



Universiteit  
Leiden  
The Netherlands

## Search for shell effects in metallic nanowires

Mares, Ancuta Ioana

### Citation

Mares, A. I. (2006, December 13). *Search for shell effects in metallic nanowires*. Retrieved from <https://hdl.handle.net/1887/5432>

Version: Corrected Publisher's Version

License: [Licence agreement concerning inclusion of doctoral thesis in the Institutional Repository of the University of Leiden](#)

Downloaded from: <https://hdl.handle.net/1887/5432>

**Note:** To cite this publication please use the final published version (if applicable).

# Search for shell effects in metallic nanowires

Proefschrift

ter verkrijging van  
de graad van Doctor aan de Universiteit Leiden,  
op gezag van de Rector Magnificus Dr. D. D. Breimer,  
hoogleraar in de faculteit der Wiskunde en  
Natuurwetenschappen en die der Geneeskunde,  
volgens besluit van het College voor Promoties  
te verdedigen op woensdag 13 december 2006  
klokke 15 uur.

door

Ancuta Ioana Mares

geboren te Hunedoara, Roemenië in 1979

### **Promotiecommissie**

Promotor: Prof. dr. J. M. van Ruitenbeek  
Referent: Dr. C. Untiedt (Universidad de Alicante, Spanje)  
Overige leden: Dr. G. H. L. A. Brocks (Universiteit Twente)  
Prof. dr. L. J. de Jongh  
Prof. dr. P. H. Kes  
Dr. ir. T. H. Oosterkamp  
Prof. dr. M. Orrit

The work described in this thesis is part of the scientific program of the "Stichting voor Fundamenteel Onderzoek der Materie (FOM)".

Casimir PhD Series, Delft-Leiden, 2006-14  
ISBN: 90-8593-021-9.

Printed by Optima Grafische Communicatie, Rotterdam: [www.ogc.nl](http://www.ogc.nl).

pentru Iulian  
mami, tati, Stefan,  
Nica si Doru



# Contents

<b>1</b>	<b>Introduction</b>	<b>1</b>
<b>2</b>	<b>Theoretical considerations concerning the stability of metallic nanowires</b>	<b>5</b>
2.1	Introduction . . . . .	5
2.2	Free electron model . . . . .	6
2.2.1	Cylindrical nanowires . . . . .	6
2.2.2	Deformed nanowires . . . . .	11
2.2.3	Stability under finite bias . . . . .	12
2.2.4	Force oscillations . . . . .	13
2.3	Atomic packing model of a nanowire . . . . .	15
2.4	Experiments on shell structure in alkali metal nanowires . . . . .	16
<b>3</b>	<b>Experimental techniques</b>	<b>19</b>
3.1	Mechanically controllable break junction in ultra high vacuum . . . . .	19
3.2	Experimental setup . . . . .	20
3.2.1	UHV insert . . . . .	20
3.2.2	UHV chamber . . . . .	20
3.2.3	UHV preparation . . . . .	21
3.3	Measurement technique . . . . .	24
<b>4</b>	<b>Observation of shell effects in nanowires for the noble metals gold, silver and copper</b>	<b>27</b>
4.1	Introduction . . . . .	27
4.2	Results . . . . .	28
4.2.1	Electronic shell effects . . . . .	28
4.2.2	Atomic shell effects . . . . .	28
4.2.3	Experiments under ambient conditions . . . . .	32
4.3	Discussion . . . . .	34
4.3.1	Comparison with low temperature histograms . . . . .	34
4.3.2	Comparison between the three different noble metals . . . . .	34
4.3.3	Electronic shell effect theory . . . . .	34
4.3.4	Comparison to magic numbers of noble metal clusters . . . . .	38
4.3.5	Atomic faceting . . . . .	38

CONTENTS

4.4	Conclusions . . . . .	39
<b>5</b>	<b>Atomic packing of gold single crystal nanowires</b>	<b>41</b>
5.1	Introduction . . . . .	41
5.2	Images of gold nanowires . . . . .	41
5.3	Experimental details . . . . .	42
5.4	Single crystal nanowires along the [110] orientation . . . . .	43
5.5	Comparison between the three orientations: [110], [100] and [111]	46
5.5.1	Beginning histograms . . . . .	46
5.5.2	Intermediate regime . . . . .	48
5.5.3	Final histograms . . . . .	50
5.6	Discussion . . . . .	53
5.7	High bias voltage . . . . .	54
5.8	Conclusions . . . . .	57
<b>6</b>	<b>Shell structure in multivalent metals: aluminum and magnesium</b>	<b>59</b>
6.1	Introduction . . . . .	59
6.2	Aluminum . . . . .	60
6.2.1	Experimental results . . . . .	60
6.2.2	Discussion . . . . .	61
6.3	Magnesium . . . . .	65
6.3.1	Results . . . . .	65
6.3.2	Discussion . . . . .	67
6.4	Conclusions . . . . .	69
<b>7</b>	<b>Mechanical properties of metallic nanowires</b>	<b>71</b>
7.1	Introduction . . . . .	71
7.2	Experimental methods . . . . .	72
7.2.1	Device design . . . . .	72
7.2.2	Oscillator model of a tuning fork . . . . .	72
7.2.3	Calibration of the stiffness of the contact . . . . .	73
7.2.4	Driving the tuning fork . . . . .	74
7.2.5	Detecting the tuning fork signal and its calibration . . . . .	75
7.2.6	Calibration of the tuning fork oscillation amplitude . . . . .	77
7.3	Experimental results . . . . .	78
7.3.1	Platinum nanocontacts . . . . .	78
7.3.2	Stiffness of a Pt atomic chain . . . . .	81
7.3.3	One atom contact of Pt . . . . .	84
7.3.4	Why does a chain break . . . . .	85
7.3.5	The stiffness of an atomic bond . . . . .	88
7.3.6	Stiffness in the tunnelling regime . . . . .	89
7.3.7	Stiffness of gold atomic contacts . . . . .	91
7.3.8	Measurements on Au at room temperature . . . . .	94
7.3.9	Conclusions . . . . .	97

*CONTENTS*

<b>8 Search for shell structure by electrochemically controlled gold nanowires</b>	<b>99</b>
8.1 Introduction . . . . .	99
8.2 Working principle . . . . .	100
8.3 Electrochemical cell . . . . .	100
8.4 Electrolysis of gold . . . . .	102
8.5 Device design . . . . .	105
8.6 Experimental results . . . . .	105
8.6.1 Conductance traces . . . . .	105
8.6.2 Stabilizing certain diameters . . . . .	108
8.7 Discussion . . . . .	110
8.7.1 Conductance traces . . . . .	110
8.7.2 Enhancement of stability by shell effect . . . . .	110
8.7.3 Low stability of small contacts . . . . .	111
8.8 Conclusions . . . . .	112
<b>Bibliography</b>	<b>113</b>
<b>Samenvatting</b>	<b>119</b>
<b>List of publications</b>	<b>123</b>
<b>Curriculum Vitae</b>	<b>125</b>
<b>Acknowledgements</b>	<b>127</b>





# I

## Introduction

The study of nano-sized specimens has received a lot of attention in the last decade. Progress is due to the development of various techniques for fabrication and characterization, like scanning tunnelling microscopy (STM), mechanically controllable break junctions (MCBJ), atomic force microscopy (AFM) and transmission electron microscopy. The contribution of chemistry to nanoscience becomes considerable in the recent years since one important direction is towards studying the properties of single molecules. This is justified by possible applications in microelectronics industry where the need in miniaturization of the components is pushed towards the ultimate limit: the size of atoms and molecules. When it will be possible to use a molecule as a transistor, still it will not be efficient to assemble every transistor by hand into a microchip and then every microchip into a nanomachine. Instead one can use self-assembly systems that as a whole will function as nanomachines. Therefore an important tool in nanotechnology is the supramolecular chemistry that deals with the synthesis of new molecules that have the property of self-assembly. The self-assembly is the structural organization of molecules in a ordered, patterned way, forming a stable and well defined stable structure. Replacing the present day computers with self-assembly nanomachines promises great advantages as improving the reliability and functionality, reducing the size and at the same time replacing the sophisticated and expensive lithographic fabrication of the chips.

Metallic nanowires, that are the subject of this thesis, can be considered as self-assembly systems in several aspects: they show a self organizing and stabilizing effect and they can be obtained by easy and accessible techniques. At the first sight, the stability of nanowires having its length longer than its diameter is unexpected. Due to the Rayleigh instability the nanowires are classically expected to collapse under their own surface tension. In contrast, we show that metallic nanowires, that can have cross-sections as large as tens of nm and as small as a few atoms, are special. They possess well-determined exceptionally stable diameters, that are so robust that they survive even under ambient conditions. Reducing the dimensions even further, chains of one single atom in cross-section can be formed, having a length that can reach seven times its diameter [1] and are extremely robust, sustaining pressures higher than in bulk materials [2].

The exceptional stability of nanowires is explained by the contribution of the quantum corrections to the total free energy of the system that will play an important role, compensating the Rayleigh instability and giving rise to a

well determined series of stable nanowires. This is due to the discrete transversal electronic states in a nanowire that will result in groups of levels bunched together and a nanowire is favored when such a shell is just filled. The phenomenon is known already from metallic clusters where the closing of shells influences the formation of "magic" clusters [3, 4, 5]. This effect is more generally appearing in fermionic systems confined in a spherical potential, like atoms where increased stability is found for elements having their electronic shells complete. An example are the noble gasses that manifest exceptional stability against ionization. Nuclei also manifest shell effects where certain isotopes are preferred.

For metallic nanowires, the shell effect was first found for alkali metals that show two series of stable diameters: electronic [6] and atomic [7], where closed-packed structures are favored. Continuing the research of stability of metallic nanowires we address further issues, extending the research to other metals, like noble metals and multi valent ones Al and Mg.

Despite the similarity of chemical self-assembly with the metallic nanowires, the latter are not as close to technological applications as the first ones. Nevertheless a few steps have been made in this direction. We found evidence of stable diameters for gold under ambient conditions. Further we have obtained atomic size contacts by electrochemical fabrication. Electrochemistry has the potential of replacing more sophisticated equipment and introduces additional parameters to control the nanowires, such as the electrochemical voltage. It is also closer to applications in molecular electronics since the solution environment facilitates attaching molecules to the metallic nanowires and study their electrical properties.

This thesis has as research purpose the investigation of stability of metallic nanowires from monoatomic chains to nanowires composed of hundreds of atoms in cross-section. In Chapter 2 we present an overview of the theoretical approaches based on a free electron model used to study the stability of the nanowires. The free electron model has been proven successful in explaining the stability spectrum in metallic clusters and it was recently found that it can explain the stable diameters found in alkali metal nanowires. Different aspects of the nanowire stability are presented, including the predicted stable diameters, the shape of the nanowire, the bias voltage influence and Jahn-Teller distortions. For the atomic shell effect a packing model used to explain the series of peaks at higher diameters is shown.

In Chapter 3 we present the main fabrication technique for the nanowires: MCBJ in ultra high vacuum. We have adapted the common MCBJ to the use of room temperature in ultra high vacuum. Room temperature gives the advantage of high atomic mobility where self stabilizing effects can be addressed. We will present the UHV set-up and the MCBJ design. We measure the conductance of the nanowires, that is related to its radius.

In Chapter 4 we present experimental results on noble metal nanowires. We perform statistical analysis constructing histograms from the conductance traces. Similar to alkali metal nanowires we obtain two series of stable diameters. At low diameters the stability is given by the electronic shell effect. A

## *Introduction*

cross-over appears at larger diameters to shells of atoms where the low surface energy nanowires are preferred. A careful comparison is presented between the three noble metals for which similar results are obtained with the exception that Cu shows no atomic shell effect but the electronic shells dominate up to high diameters. The electronic shell stable diameters are similar to the magic diameters found in noble metal clusters. Good agreement with theoretical prediction by a free electron model is obtained. For the atomic shell effect we interpret the stable diameters as due to packing along a favorable crystalline orientation, in this case [110] that is in good agreement with molecular dynamics simulations and with images of nanowires provided by high resolution transmission electron microscope (HRTEM).

Although the stable diameters are reproducible, one cannot predict in advance which will dominate the spectrum the electronic or the atomic shell effect. In other words, the cross-over between the two varies between different measurements. Also the relative intensity of the peaks varies from one measurement to the next. We have attributed it to different crystalline orientations of the nanowire. We have verified this assumption by performing measurements on single crystal nanowires, presented in Chapter 5. Additionally we have verified that [110] is the preferred direction for atomic shell effect. We recorded conductance histograms for wires initially oriented along the three main crystalline axis: [110], [100], [100]. Our results show that indeed for [110] atomic shell effect dominates and more reproducibility is obtained regarding the peak positions and value of the cross-over. The distinction between the different orientations is not as clear as we had hoped. Although on a fresh sample for the [100] and [111] different behavior is found than for the [110] orientation, we have indications that when repeatedly breaking and making the nanowire a transition towards the [110] axis occur. This observation is valuable by itself suggesting that [110] is a more stable orientation, as we had expected. As a side result we discovered an exceptional effect of stabilization of small contacts by high bias voltages.

The study of shell structure is extended to multi valent metals: Al and Mg presented in Chapter 6. Magic numbers are obtained for Al and Mg clusters and it is shown that the free electron model can explain most of them. Due to their electronic configuration, new effects are found, namely the transition from metallic to non-metallic for small cluster size where a gap between the energetic levels is formed. For Al nanowires we report two series of stable diameters that agree well with the expected periods for electronic and atomic shell effects. Al has a special feature: besides the stable diameters that agree well with what was predicted from the theory, two unexpected diameters are found. They are exceptionally stable, occurring isolated in some histograms. For the case of Mg the interpretation of the histograms is not as straight forward. The periods of the peaks found in the histograms can be attributed to atomic shell effect respectively to electronic shell effect. For the latter one needs to take into consideration also deformed wires. In most of the histograms an intermediate value is found that can be caused by the interplay of the two effects. Mg is special in the sense that, similar to clusters, we have indications that very thin nanowires are electrically insulating.

## *Chapter 1: Introduction*

A different approach on the stability investigation is reported in Chapter 7. We present here stiffness measurements performed with a combination of MCBJ and a piezoelectric tuning fork, that is a very sensitive force sensor. We have investigated the stability properties of thick nanowires at room temperature searching for signs of shell effects in the force acting in the nanowire. Secondly we have investigated the formation and stability of monoatomic chains. The latter experiments are performed at cryogenic temperature, where we have the advantage of keeping an atomic contact stable for long time. Also the cohesion force in the tunnelling regime has been investigated. We performed measurements for Au and Pt.

In Chapter 8 we present an alternative way of nanowire fabrication by electrochemical methods. We can obtain atomic sized contacts by electrochemical etching and reversible cycles of deposition and dissolution can be made. In this way we obtain a conductance histogram with peaks that agree with the ones obtained by MCBJ in UHV. However better control of the electrochemical process needs to be achieved in order to proceed in the process of stabilizing even further the "magic" diameters.

We have investigated most of the metals that are expected to show shell effects at room temperature based upon metal cluster studies and we can draw the conclusion that shell effects are generally present in nanowires of free electron metals and nearly free electron metals.

# II

## Theoretical considerations concerning the stability of metallic nanowires

### 2.1 Introduction

We have seen that nanowires made of several metals (alkali metals, noble metals, Al and Mg) show exceptional stability for particular radii. This has been identified as shell effect and its principle is well known from atomic physics, giving rise to the periodic table of the elements, and from nuclear physics, explaining the periodic appearance of stable nuclei. The effect was found also in metallic clusters, where it is related to the filling of energetic levels (for a review see [3]). For nanowires the electronic shell effect can be understood in terms of the filling of simple free-electron modes inside a cylindrical cavity. The electronic level spectrum of such systems shows groups of levels bunched together and a nanowire is favored when a shell is just filled. While the clusters are confined in all three dimensions by a spherical potential, for nanowires, along their axis the energy possesses a continuous spectrum, forming sub-bands instead of levels.

The shell effect was first observed in alkali metal nanowires [6] where similar to clusters two series of "magic" numbers are found. At low diameters the stability is given by closing of electronic shells. For larger diameters the surface contribution to the total energy dominates and closed-packed structures are favored. In section 2.2 we give an overview of the theoretical results concerning stability analysis related to electronic shell effect. The description is given in terms of a free electron model using a hard wall confining potential. This model is proven to work and the evidence comes from the good description of the shell effects in metallic clusters [3]. In section 2.3 a model of atomic packing for a fcc nanowire is presented. Section 2.4 summarizes previous experimental work on shell effects in alkali nanowires.

## 2.2 Free electron model

### 2.2.1 Cylindrical nanowires

The free electron model is especially appropriate for describing the electronic shell effects for monovalent metals with a spherical Fermi surface. The results of this model reproduce in detail the experimentally obtained stable diameters for Na [8]. A large part of the theoretical work using free electron model to study the nanowire stability is done by C. A. Stafford and coworkers. The model in its simplest form uses a cylindrical nanowire with a length much larger than its cross-section radius. The electrons are modelled to move freely and the electron-electron interactions are neglected for the first part of this investigation. In this model the electrons are confined by a hard wall potential. Classically, a nanowire having its length longer than its diameter should be unstable, breaking up under the influence of its surface tension. This phenomenon known as the Rayleigh instability, is known from fluids, but it is more general occurring in systems with large aspect ratio. In a nanowire the atoms will diffuse on the surface tending to break a cylindrical nanowire into a row of spheres. The experimental observation of Rayleigh instability in metallic nanowires was recently reported [9]. Remarkably, quantum corrections to the electronic free energy of the system play a significant role, not only in making possible the formation of long and thin nanowires but additionally certain diameters are exceptionally stable. The increased stability of given diameters is related to minima in the total energy of the nanowire. The thermodynamical potential that describes open systems where the nanowire exchanges electrons with the leads, is the grand canonical potential. The requirements used in the model are that the total volume of the nanowire is conserved, meaning that the wire is incompressible and does not exchange atoms with the leads. Bürki *et al.* [10] use an expression obtained from the liquid-drop model for the thermodynamical potential as:

$$\Omega[R(z)] = -\omega V + \sigma_s S - \gamma_s C + \int_0^L dz V_{shell} \quad (2.1)$$

with  $V$  the volume of the cylinder,  $S$  the surface area and  $C$  the mean curvature of the wire's surface.  $\sigma_s$  is the surface energy and  $\gamma_s$  is the curvature energy. The grand canonical potential has a geometrical part represented by the first three terms and an oscillating part,  $V_{shell}$ . Eq.(2.1) shows that  $\Omega[R(z)]$  becomes smaller for a given volume for small surface energy and large curvature, the latter meaning that a smooth and long wire is favored.

It was shown by Balian and Bloch already in 1972 [12] that a correspondence between the structures in the quantum mechanical DOS and classical mechanics can be made. When the Fermi wavelength of the electrons is much smaller than the dimensions of the system, classical methods can be used to describe such a system, and one can calculate for example the classical trajectory of the electrons moving in the circular cross-section of a cylindrical nanowire. A brief review about how one can attribute periodic orbits to the movement of the electrons is given by A. I. Yanson in his PhD thesis [13] and we will not reproduce

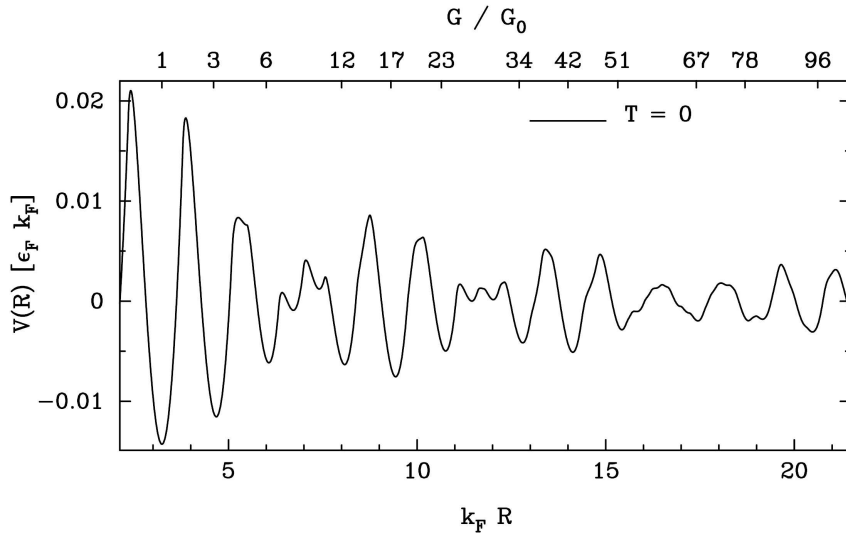


Figure 2.1: Electron shell potential at zero temperature. The minima of the potential represent stable wire diameters and their conductance is plotted on the upper axis. Reproduced from [11].

the derivation here. The main result is that the DOS can be constructed as due to the trajectory of electrons as decomposed into a sum of regular polygons. The contribution of the orbits decreases with its number of vertices, and in a good approximation one can consider that the first three orbits are significant in describing the transverse motion of electrons: diametric, triangular and square orbits. This was observed experimentally for the stable diameters for alkali metal nanowires [13]. When two or several periodic orbits having different frequencies contribute to the oscillation spectrum, a beating phenomenon occurs, resulting in an amplitude modulation of the peaks. This was observed in the experimental spectra of alkali metals and is known as super-shell effect.

The density of states can be decomposed for a cylindrical nanowire into a smooth average contribution and an oscillating part. The latter can be calculated as a sum over all periodic classical orbits of the system. One obtains the so-called Gutzwiller trace formula for the electron shell potential in Eq.(2.1), the name comes from the fact that the trace of the electron Green's function is taken [10], [14]:

$$V_{shell} = \frac{2\varepsilon_F}{\pi} \sum_{w=1}^{\infty} \sum_{v=2w}^{\infty} a_{vw}(T) \frac{f_{vw} \cos \theta_{vw}}{v^2 L_{vw}} \quad (2.2)$$

where

$$L_{vw} = 2vR \sin(\pi w/v) \quad (2.3)$$



is the length of the orbit inscribed in the cylinder of radius  $R$ . The sum includes all periodical orbits characterized by their number of vertices  $v$  and the winding number  $w$ . The factor  $f_{vw}=1$  for  $v=2w$  and 2 otherwise, accounts for the invariance under time reversal symmetry of some orbits and  $a_{vw} = \tau_{vw} / \sinh \tau_{vw}$  is the phase an electron acquires along its orbit, where  $\tau_{vw}(T) = \pi k_F L_{vw} T / 2T_F$  and  $\theta_{vw} = k_F L_{vw} - 3v\pi/2$ . The potential (2.1) has an oscillatory dependence on the radius of the wire, with minima that represent stable configurations, as seen in Fig. 2.1.

Kassubek *et al.* show that the shell effect suppress the Rayleigh instability [14]. The stability of the wire is studied within the perturbation theory. A long wavelength surface perturbation is applied to the nanowire and its effect on the grand canonical potential is studied. The wire radius under such a deformation can be expressed as [15]:

$$R(z) = R_0 + \int_{-\infty}^{\infty} dq b(q) e^{iqz} \quad (2.4)$$

where  $b(q)$  is a perturbation coefficient,  $R(z)$  is the radius of the wire at  $z$  and  $R_0$  is the radius of the unperturbed cylinder. This perturbation adds an extra term to the grand canonical potential:

$$\Delta\Omega = \int_0^{\infty} dq \alpha(q, R_0) |b(q)|^2 + O(b^3) \quad (2.5)$$

with  $\alpha(q=0) = \alpha_0$ :

$$\alpha_0 = -\frac{2\pi\sigma_s}{R} + \left( \frac{\partial^2}{\partial R^2} - \frac{1}{R} \frac{\partial}{\partial R} \right) V_{shell}(R) \quad (2.6)$$

Here  $\alpha_0$  is a significant parameter since its sign is a direct measure of the wire stability with respect to perturbations. When  $\alpha_0$  is negative  $\Delta\Omega$  will give a decrease in the grand canonical potential resulting in a instability. This occurs at the opening of new sub-bands, represented by the spikes in the *DOS*, see Fig.2.2. At these points the nanowire is unstable, while between two peaks in the *DOS* the electron shell effect contribution stabilizes the wire.

Eq. 2.6 shows the competition between the surface tension and the electron shell potential. The dependence of the surface energy with the radius goes like  $O(k_F R)$  while the electronic energy dependence is  $O(1/k_F R)$ . Since the second derivative for the electron potential enters in the expression, this avoids the suppression of the electron shell effect for high nanowire radii. A stability diagram can be constructed containing the regions of positive  $\alpha_0$  (Fig. 2.2 bottom). The dark areas represent the regions where the wire is stable with respect to perturbations. The authors have shown that the temperature (seen on the vertical axis normalized to  $T_F$ ) gives information about the life time of the wire [10]. Notice that, although the maximum temperature to which the nanowires are stable fluctuates, nevertheless for the main regions (the thick fingers of stability) the maximum temperature decreases smoothly with increasing

Free electron model

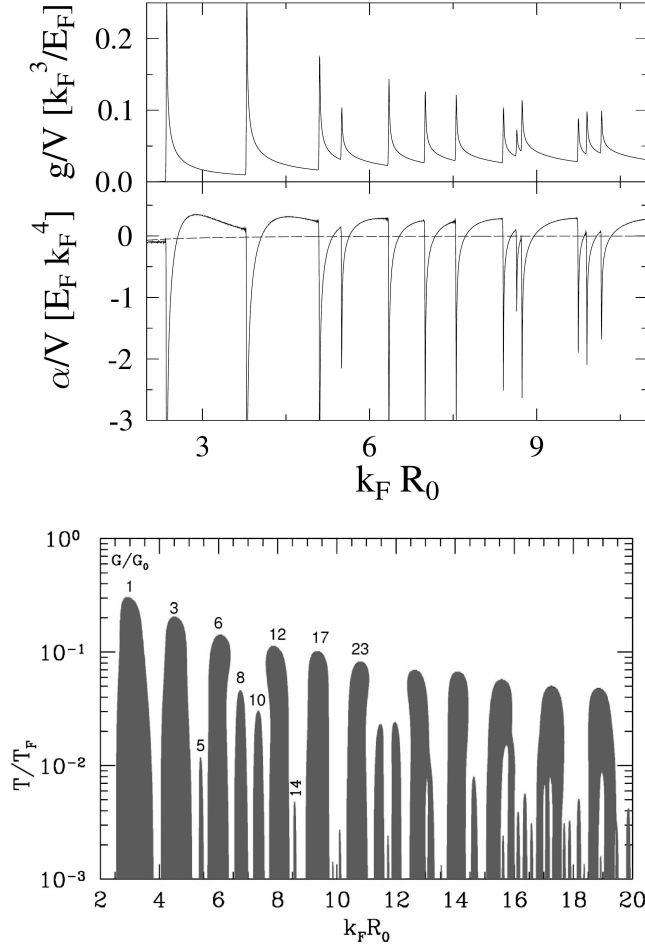


Figure 2.2: Top: DOS at the Fermi energy and the stability coefficient  $\alpha_0$ , normalized by the volume of the wire. The negative values of  $\alpha_0$  indicate instability regions. Reproduced from [10]. Bottom: Stability diagram for cylindrical nanowires. Dark areas indicate stability with respect to small perturbations. Reproduced from [10]

the diameter. Exceptionally stable values are found at 1, 3, 6, 12, 17, 23...  $G_0$  which are the magic numbers for this wire. These values are found at the points the given stability zones extend to the highest temperature.

The evolution towards the equilibrium shape of the wire was also investigated by studying the self diffusion of atoms on the nanowire surface [10], [16]. The simulation reveals the formation of a long, smooth, cylindrical wire when starting from an irregular one, see Fig. 2.3. The surface roughness is slowly

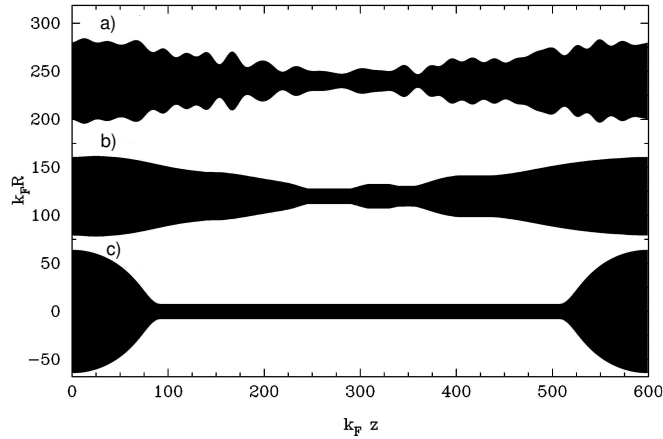


Figure 2.3: Theoretical simulation of the evolution towards the equilibrium of a nanowire. Taken from [16]. (a) represents the initial nanowire configuration, (b) is the wire shape at an intermediate moment and (c) is the equilibrium structure with  $G = 12 G_0$ .

removed as the defects propagate to the ends of the wire. The next step is to analyze the evolution of the wire with applied stress [16]. The wire is elongated by increasing its length at a constant speed while decreasing its radius for the volume conservation. Just before the moment of breaking, the wire is let to relax and equilibrate. In the elongation process kinks will occur at the center of the nanowire, that move towards the connecting electrodes leaving the wire a long smooth cylinder. This is how the wire necks down through the stable diameters. The phenomenon of kinks formation and their increase in amplitude comes from the Rayleigh instability. Remarkably the quantum corrections will stabilize the wire and the amplitude of the kinks will saturate and eventually propagate towards the leads, leaving behind a smooth wire. In the evolution of a nanowire towards breaking it is found that when unstable diameters occur, the wire will not break, but instead it will thin down to the next stable diameter [17]. This is consistent with the experimental conductance traces that are not reproducible in detail and unstable diameters can occur in the evolution. However, the averaged behavior represented in the conductance histograms reflects the reproducible, stable configurations of the wire.

Similar results on cylindrical nanowires using a free electron model are reported independently by other groups. Predictions of electronic shell structure in nanowires are done already from 1997. The principle of stability enhancement of nanowires by the electronic mechanisms is demonstrated using a simple descriptive free electron model [18]. From about the same time dates a prediction of magic wire configurations obtained with a jellium model and a local density functional based shell correction [19], commonly used to describe the

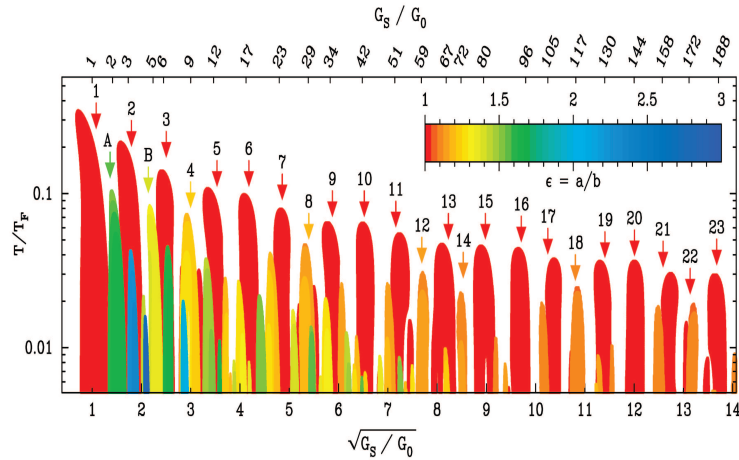


Figure 2.4: Stability diagram including elliptically deformed nanowires. The results are specific for Na nanowires.  $\epsilon$  is the aspect ratio of the ellipse, coded via the color scale shown in the inset. Reproduced from [22].

properties of clusters. In the same spirit are the calculations done by Ogando *et al.* [20], [21]. They use a soft potential and consider the valence electron density for the given metal. This allows to find different stability spectra for different metals. Ogando *et al.* calculate the minima in total energy per unit length. We will compare our experimental results with the predicted stable diameters for aluminum. The same group performs an analysis of the Na nanowires [21]. The theoretical results agree well with the experimental histograms and especially the position of the beats due to the supershell structure are well reproduced. Higher order orbits are included in the study and it is found that the star orbit will give a significant contribution in the stability spectrum of nanowires.

## 2.2.2 Deformed nanowires

The free electron model for cylindrical wires is successful in explaining the main features in the experimental series of peaks in the conductance histograms. However some peaks are still unexpected. Inspired by the existence of non-spherical clusters, Urban *et al.* investigate the stability of deformed wires. The effect found for metallic clusters is the so-called Jahn-Teller distortion, by which a spherical cluster deforms its cross-section in order to minimize its total energy. For nanowires, as it will be discussed, this deformation is expected to occur only for a small part of nanowires, typically 25%, but it is useful to explain the occurrence of certain special features in the spectrum. Urban *et al.* [22] calculate the grand canonical potential fully quantum mechanically using largely the same type of calculations as described in section 2.2.1. The deformation of the cross-section of the cylindrical wires is introduced as a perturbation, and the stability

of the nanowires is described by the stability diagram shown in Fig. 2.4. Several deformed wires appear in between the regular cylindrical ones, their deformation being described by  $\varepsilon$ , that is the aspect ratio of the ellipse. In particular two wires pointed out by arrows *A* and *B* are exceptionally stable, as one can see from the maximum temperature to which they survive. The stability diagram is applied to the particular case of Na nanowires. For noble metals and Al and Mg nanowires the stability diagram is found to be similar, the predicted stable diameters are on the same positions but the elliptical nanowires are more stable. The reason is that due to a lower surface tension for the noble metals than for alkali metals the predicted elliptical wires are less deformed [22]. In the next chapters we will compare the predicted radii positions for the stable nanowires with the experimental peaks.

### 2.2.3 Stability under finite bias

Most of the studies are done considering zero bias limit [10, 16, 17, 20, 21, 23, 24, 25, 26]. When a finite bias voltage is applied to the nanowire the electron distribution will be in non-equilibrium, namely the scattering states will be occupied differently for the left moving states compare to the right ones. In order to obtain the equilibrium one needs to lift the Fermi energy that is done by taking into account the electron-electron interactions. The authors [27] treat the Coulomb interactions using a mean field potential, in this case Hartree potential, that considers the interaction of one electron in an average density of the rest electrons:

$$U(\vec{r}) = \int d^3r' V(\vec{r} - \vec{r}') \delta\rho(\vec{r}') \quad (2.7)$$

where  $\rho(\vec{r})$  is the uncompensated charge and  $V(\vec{r}) = e^2/r$  is the Coulomb potential. A more general expression for the grand canonical potential is obtained for the non-equilibrium case when the potential is added, that is solved self consistently. The results for zero bias are very similar to the results obtained from the purely free electron model without considering the Coulomb interactions [25]. The reason is that for zero bias the contribution of the Hartree potential is a second order correction to the total energy of the system. The nanowires stability for different radii as a function of the bias voltage is shown in Fig. 2.5. For the low conductance range the thresholds of the sub-bands are indicated. As expected, here the nanowire becomes unstable. Remarkably the stability zones for most of the magic wires extend up to very high bias voltages, although the regions get narrower with increasing bias. Remarkably, new areas of stability open up when increasing the bias voltage, for example at 2, 4.5, 7, 15, 20  $G_0$ . The bias voltage at which they appear is around 0.2-0.3  $\varepsilon_F$ . For the case of noble metals this would correspond to bias voltages higher than 1 V, since they have a relatively high Fermi energy, e.g. for gold,  $\varepsilon_F=5.5$  eV. As we report in chapter 5 above 0.5 V a new behavior is found for gold, therefore we could not obtain a bias dependence of the stable diameters. The typical bias voltages used

### Free electron model

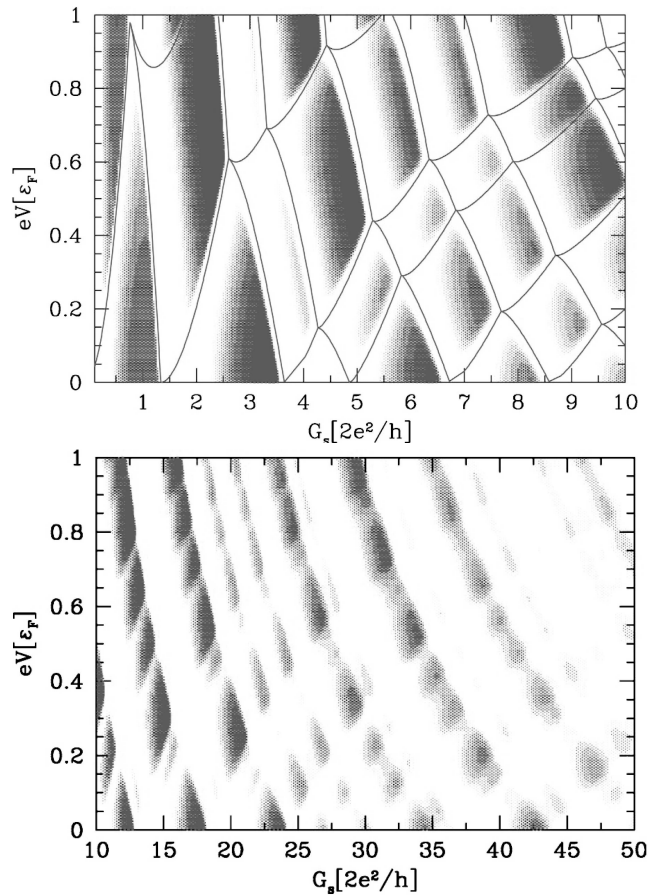


Figure 2.5: Stability diagram of cylindrical nanowires as a function of the bias voltage. Shaded area indicate stability with respect to perturbations. In the upper figure the solid lines indicate the sub-band thresholds. Taken from [27].

for recording a conductance histogram is 100-200 mV. In this case we can consider the zero bias approximation, which is similar to the results without taking into account the electron-electron interactions. In the case of alkali metals the Fermi energy is about 2 times lower and already for bias voltages around 0.3 V a new series of peaks is expected. However, no bias dependence has been reported for shell structure in alkali metals.

#### 2.2.4 Force oscillations

In this subsection we present a derivation of the expected fluctuations in the stiffness of the contact due to the electronic cohesion following Stafford *et al.*

[25], [15], [28]. The authors have shown that the transverse eigen states of the electrons contribute both to the cohesion and to the conductance. The calculated force has an oscillation amplitude that is independent of the wire cross-section and is proportional to  $\varepsilon_F/\lambda_F$ . In the particular case of gold this would mean values of 1nN, in agreement with typical experimental values [29]. The predicted force oscillations agree with results reported by other groups that use also free electron model [30], [31]. Correlations between the force oscillations and conductance steps are also found by Zabala *et al.* [32] using a free electron model with a soft potential and analyzing the case of Al, Na and Cs.

The results reported by Stafford *et al.* [25], [15], [28] are obtained starting from a grand canonical potential expression similar to Eq.(1) separated into a smooth contribution, formed by geometrical terms and an oscillating term. The oscillating part of the force is obtained from  $F = -\frac{\partial\Omega}{\partial L}$ , under the assumption of volume conservation:

$$\delta F \simeq -\frac{2\varepsilon_F}{\lambda_F} \sum_{w=1}^{\infty} \sum_{v=2w}^{\infty} \frac{f_{vw}}{v^2} \sin(k_F L_{vw} - 3v\pi/2) \quad (2.8)$$

where the dependence on the wire cross-section enters through  $L_{vw}$ , as seen in Eq.(2.3). Here we use the force approximation for the case of integrable transverse motion of the electrons, e.g. for circular, elliptical or square cross-sections [25], [33]. The theoretical results usually report an expression for the force. We measure the stiffness that will be discussed in chapter 7. Therefore we would be interested in having an estimation of the order of magnitude of the fluctuations of the stiffness related to stability of nanowires due to electronic shell effect. Considering the volume of the wire to be constant, we can use the following relation to find the expression for the stiffness of the contact,  $k$ :

$$k = -\frac{\partial F}{\partial L} = -\frac{D}{2L} \frac{\partial F}{\partial D} \quad (2.9)$$

with  $D$  the diameter of the wire cross-section and  $L$  the length of the wire. The expression for  $k$  yields:

$$k = -\frac{2\varepsilon_F}{\lambda_F^2} \frac{D}{L} \sum_{w=1}^{\infty} \sum_{v=2w}^{\infty} \pi \frac{f_{vw}}{v} \sin \frac{\pi w}{v} \cos(k_F L_{vw} - 3v\pi/2) \quad (2.10)$$

The summation will give a factor of the order of unity and therefore we can estimate the order of magnitude of the stiffness amplitude of a few N/m. We stress that this contribution is calculated considering only the force due to the electronic cohesion. This should be a good approximation since for metals it is a dominant contribution to the total force. We anticipate that in our experiment we are not able to make the difference between this electronic contribution and the atomic one, resulting in relaxations corresponding to atomic rearrangements.

### 2.3 Atomic packing model of a nanowire

At larger diameters, the surface energy becomes more important than the free energy. The formation of dense packed structures that have minimum surface for a given volume will be favored. A crossover between the electronic shell filling and atomic shells has been observed for metallic clusters [5]. The close-packed structures are non-crystalline and different ways of spherical packing are reported using polyhedra with different symmetries. Stable clusters are obtained not only when an atomic shell is complete but also when an individual facet is added. For noble metal clusters icosahedral packing is reported [34], [35]. In the case of Al octagonal packing is reported [5] and Mg has icosahedral symmetry [36].

Also in the case of nanowires the surface energy oscillations are expected to take over at large radii, since the oscillation amplitudes of the electronic free energy have a  $1/R$  dependence while the ones for surface energy increase linearly with  $R$  [10], [26]. A cross-over between the two is experimentally observed by the change in the oscillation period of the peaks. We propose a model for nanowire faceting starting from the crystalline order that we have in bulk: fcc for all three noble metals and aluminum.

Rodrigues *et al.* have imaged gold and silver nanowires using HRTEM [37], [38], [39]. A more detailed description of these experiments is presented in chapter 5. It is found that the nanowires preserve their crystalline order down to the smallest contact. [110] is found to be the preferred direction for pulling long wires with ordered facets. The configuration of the wires is modelled using the Wulff construction that takes into account the low energy facets when constructing a nanowire. Similar results are reported by the group of Takayanagi using the same experimental technique [40]. The results agree with a molecular dynamics simulation [41] that shows that the thinning down of the wire occurs by removing layer by layer and the wire is even more stable when all the layers are complete. In order to explain the stable diameters observed in the conductance histograms due to filling of atomic shells we will use similar considerations. The lowest energy surfaces for gold are perpendicular to [111] and we can construct a densely packed wire along a [110] axis with four (111) and two (100) facets, see Fig. 2.6. The filling of each individual facet will give a stable diameter.

The conductance can be related to the wire cross-section area by Sharvin's formula and a correspondence with the layers of atoms can be made as:

$$g = G/G_0 = \frac{k_F^2}{4\pi} A = C (m + 1/2)^2 \quad (2.11)$$

where  $A$  is the area of the hexagonal facet,  $m$  is the index of the layer added to the wire, and  $C$  is a constant that depends on the distances between two consecutive (111) and (100) planes and can be determined from geometrical considerations. The expected period of adding a new layer of atoms can be found as:

$$\Delta\sqrt{g} = \frac{\partial\sqrt{g}}{\partial m} = 1.43 \quad (2.12)$$



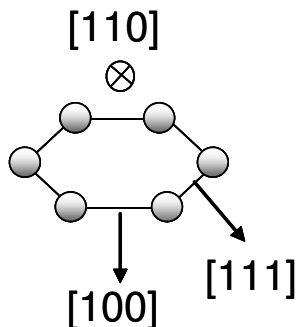


Figure 2.6: Schematic representation of suggested nanowire packing along  $[110]$  axis.

Considering the period of adding one single facet at a time, we need to divide the result in Eq.2.12 by 6 and we obtain  $\Delta\sqrt{g}=0.24$  or  $\Delta\sqrt{k_F R}=0.48$ . This value is very close to the experimentally observed periodicity. Our choice of hexagonal cross-section is also in agreement with density functional theory calculations for single crystals silver nanowires along  $[110]$  [42]. The authors calculate the minima in the surface energy and find for larger diameters stable wires with hexagonal cross-sections. There has been another proposed cross section of the nanowire with octagonal symmetry for Au and Al [43]. Also non-crystalline nanowires have been proposed by theoretical studies being referred to as "weird" wires [44]. HRTEM imaging confirmed these predictions, showing that gold nanowires adopt a helical arrangement, both at room temperature [45] and at 150 K [46]. By the same fabrication procedure straight wires are observed by Rodrigues *et al.* [37] as well as by the same group that reports the helical wires [40]. We expect that the helical wires appear when the connecting electrodes have different crystalline orientations and the wire formed in between has to wriggle to match both of them. We cannot exclude that in our experiment this geometry can occur, but it seems not very favorable, since it does not reproduce in a peak in the conductance histogram. This would suggest that under stress the helical configuration is not stable.

## 2.4 Experiments on shell structure in alkali metal nanowires

The shell effects contribution to the stability of nanowires was first experimentally observed in alkali metals [6]. The alkali metals are the simplest metals to study fundamental properties, since they can be considered free electron metals, having a valence electron very weakly bound to the nuclei. The stability of the alkali nanowires are studied by recording conductance histograms. The technique used is the cryogenic MCBJ adapted to the use of alkali metals that

are very reactive. A possibility of raising the temperature was also implemented and the experiments are carried out at temperatures around 90 K. Two series of peaks are observed in the conductance histograms. At low diameters the electronic shell effect appears, that is more pronounced in Na and Li than in K where a cross-over to atomic shell structure occurs. However for Li no atomic shell structure was seen and it was considered as due to increased atomic diffusion caused by the relatively low mass of the Li atom. Also for Na the electronic shell effect dominates in many cases [7, 13, 47]. The spectrum of orbits contributing to the stabilities in the conductance histograms have been identified by performing a Fourier transform of the oscillating part of the conductance histogram in  $k_F R$  units. The diametric orbit is dominant in this case, and the other two show together a broader peak. A nice super-shell oscillation is seen, due to the superposition of the diametric orbit with the other two ones (triangular and square) [48]. For potassium a long series of peaks is seen with a period related to atomic shell structure up to high conductance values (above  $250 G_0$ ). The period can be understood as modelling a bcc nanowire along the [111] orientation resulting in a hexagonal cross-section formed from six [110] facets. The period  $\Delta k_F R = 0.48$  [7] is relatively close to what obtained in chapter 5 for an fcc nanowire. Similar series of stable diameters are seen for heavy alkali metal nanowires [49]. The spectrum depends on the direction of forming the contact, as more peaks are observed in the pushing process. This suggests that the atomic rearrangement influences the wire evolution.



# III

## Experimental techniques

### 3.1 Mechanically controllable break junction in ultra high vacuum

We will investigate the stability of metallic nanowires by measuring their conductance that is proportional to the contact area. In our measurements we make use of the mechanically controllable break junction (MCBJ) technique [50], [51]. The sample consists of a metallic wire to which a circular notch has been made where the break will eventually occur. The wire is mounted on a bending beam that is made of phosphore-bronze alloy that permits elastic deformations. The substrate will be mounted in a three-point bending configuration, with two supports at both ends of it and a piezoelectric element in the center. The piezo will bend the substrate until the wire will break. When the stress is released, e.g., the piezo is retracted, the wire will eventually recover to the initial position and the electrical contact is remade. The initial bending is done by mechanical displacement of the piezo element that will afterwards be used for fine adjustments of the wire size.

Several adjustments had to be done to the conventional MCBJ in order to be compatible to the use at UHV and at variable temperatures. The bending beam consists of two separate phosphore-bronze substrates bridged just by the wire, that is in electrical contact with each of them, see Fig. 3.1. The two substrates are fixed to a sample holder, as seen in Fig. 3.2. The wire is fixed with two stainless steel clamps, in order to avoid the use of epoxy as in conventional MCBJ, such as to make the device compatible with UHV and high-temperatures.

The sample holder seen in Fig. 3.2 has just a single sample wire. We are interested in performing a statistical analysis on a large number of samples. Since the procedure for obtaining UHV is time consuming, we would like to avoid breaking the vacuum for each new sample that we want to measure. Therefore we have improved this design such that our new sample holder has a tray of six parallel bending beams like the ones seen in Fig. 3.2 with a sample mounted on each, as one can see in Fig. 3.3. The samples are electrically insulated and can be independently broken and measured. We have a single set of electrical connections, represented by two phosphore bronze springs that will make contact to the sample to be measured only at the moment when the substrate is in the measurement position. A similar mechanism is used for the thermocouple. The substrate position is controlled by an external linear manipulator that will bring the desired substrate in the position below the piezo. The substrate can be

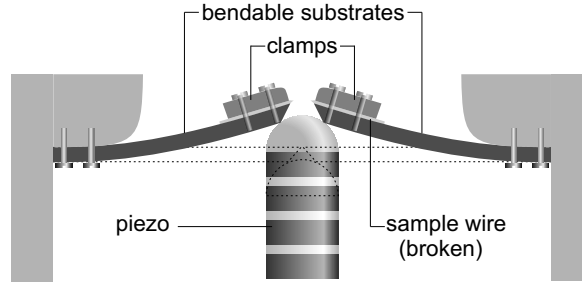


Figure 3.1: Schematic view of the MCBJ technique under UHV. The relaxed configuration of the sample is represented by the dotted lines.

locked in the measurement position, avoiding mechanical instability. We have the possibility of measuring at variable temperatures, between 77 K and 500 K. The cooling down is done by thermal contact of the sample substrate with a nitrogen bath. The sample can also be locally heated by radiation from a tungsten filament placed beneath the sample. The temperature is monitored by a thermocouple.

## 3.2 Experimental setup

### 3.2.1 UHV insert

The sample holder is mounted at the bottom of the UHV-insert, as one can see in Fig. 3.4. The insert is made of stainless-steel as most of the parts of the set-up. The insert main part consist of the nitrogen bath that is in thermal contact with the sample holder. The insert will be mounted in the vacuum chamber from the top and closed at the top flange. The mechanical axis goes through the nitrogen bath and has a separate connection to UHV at the bottom of the bath. The mechanical axis ends with a rotary-to linear gear that acts through bellows, that are commonly used for moving parts in UHV. Two electrical feed-throughs can be seen on the top of the insert in Fig. 3.4: one for the high voltage applied to the piezo element and a second one that is used for the wiring of the conductance measurements, heater and thermocouple. Clamping is used for all the electrical connections and the wires are UHV compatible materials insulated with glass fiber, that is suitable for UHV and use of high temperatures.

### 3.2.2 UHV chamber

The insert is inserted from the top into the UHV chamber, a scheme of which can be seen in Fig. 3.5. The set-up is pumped with a turbo molecular pump and in the pressure range of  $10^{-10}$  mbar an ion pump is used, that is placed at the bottom of the UHV chamber. The pressure is monitored with two pressure

### *Experimental setup*

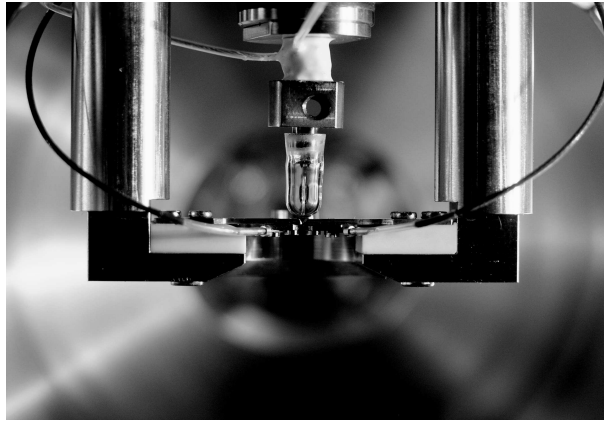


*Figure 3.2: Sample holder used for the UHV-MCBJ. The piezo is covered in white epoxy, UHV compatible torr seal [52]. Below the piezo element a quartz piece is placed that presses on the substrate and insulates thermally the piezo from the substrate. The conductance measurement coaxial wires are connected to the substrate.*

gauges, one in the pressure range of  $10^{-9}$  mbar and one ionization gauge for the lowest pressure range. A mass spectrometer is also available that can be used for gas analysis in the chamber and for leak detection. Two manual valves are available for both the ion pump and the turbo pump.

In the middle part of the UHV chamber, opposite to the turbo pump is placed the linear manipulator that is used to select one of the six samples in the tray and adjust the position of the sample below the piezo-electric element.

### **3.2.3 UHV preparation**

Our measurements are carried out at a pressure of  $4 \times 10^{-10}$  mbar. After the insert is mounted at the top of the chamber and closed, the chamber is pumped with the turbo pump, down to a pressure in the range of  $10^{-7}$  mbar. A rotary pump is used as pre-pump that has a trap in order to avoid any oil vapors going into the UHV chamber. The chamber is baked then at a temperature of 150 degrees. At this temperature most of the adsorbates from the walls, mostly water, are expected to be released. The baking temperature is increased step-wise ensuring a uniform temperature over the setup. Large temperature gradients can cause different deformations of the parts, that can cause leaks.

The UHV is maintained during the measurements by pumping only with the ion pump. Since the turbo pump is connected to the chamber without any vibration attenuators, the turbo pump should be switched off during the measurements. In the process of cooling down the set-up to room temperature the filaments of the pressure gauge and the mass spectrometer are degassed. The

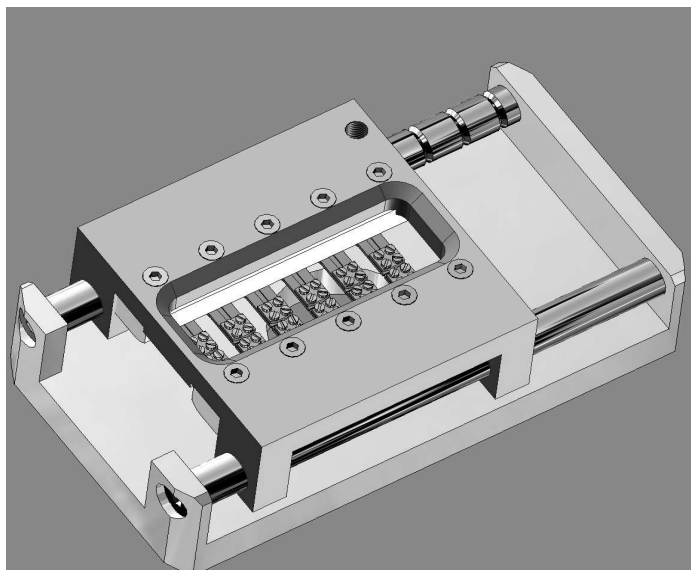
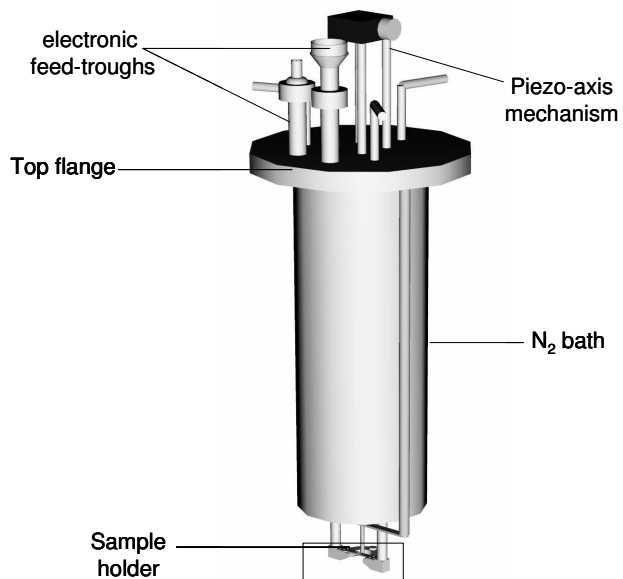


Figure 3.3: Drawing of the sample holder containing six parallel substrates. The tray can be locked in a fixed position in the grooves of the rails.

procedure is repeated at several temperatures. One of the important steps in the cooling down procedure is to clean the surface of the electrodes in the ion pump. The ion pump is degassed by switching it on briefly. A layer of adsorbates is removed from the electrodes after the impact with the high kinetic energy ions. The procedure will be repeated until the increase in the pressure when the ion pump is on decreases, e.g. when it is less than three times the pressure. The temperature at which the degassing process is optimal is around 150 degrees, when the sputtering ions have enough kinetic energy. The ionic pump will be operated for the low pressure range, since the pumping efficiency is limited by the electrode surfaces. The time it takes for the electrode surfaces to saturate with adsorbates is proportional with the pressure. For example at pressures of  $1 \times 10^{-6}$  mbar it takes an average time of a second until any atom on the surface will be hit by a gas atom. A titanium sublimation pump is also used for the  $10^{-10}$  mbar range that is efficient for removing light elements, like  $H_2$ . The pump consists of a few titanium filaments, placed inside the ion pump. The Ti filaments are heated by a high electrical current. The evaporated Ti will condense in a thin film on the chamber walls, binding some of the gases present in the chamber.

A mass spectrum showing the gasses present in the UHV chamber is shown in Fig. 3.6. The UHV chamber has been baked and cooled down to room temperature. The final pressure achieved was  $4 \times 10^{-10}$  mbar. One of the dominant contributions is hydrogen seen at the masses of 1 and 2 atomic units (a.u.). At

*Experimental setup*



*Figure 3.4: The UHV MCBJ insert made of stainless-steel. The insert enters into the UHV chamber all the way to the top flange where it is sealed. At the bottom is fitted the sample holder, that is shown enlarged in Fig. 3.2 .*

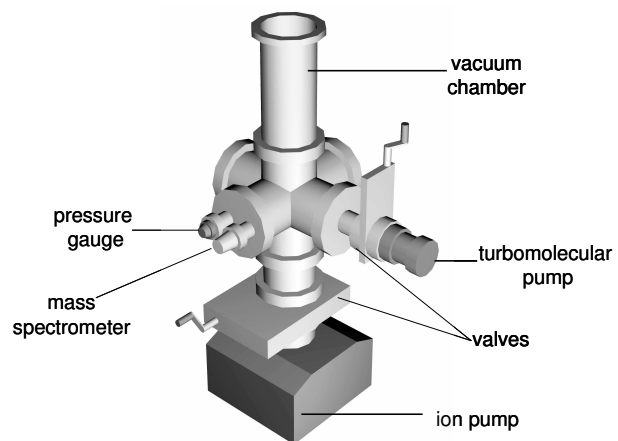


*Figure 3.5: Schematic drawing of the UHV chamber used for the MCBJ experiments.*



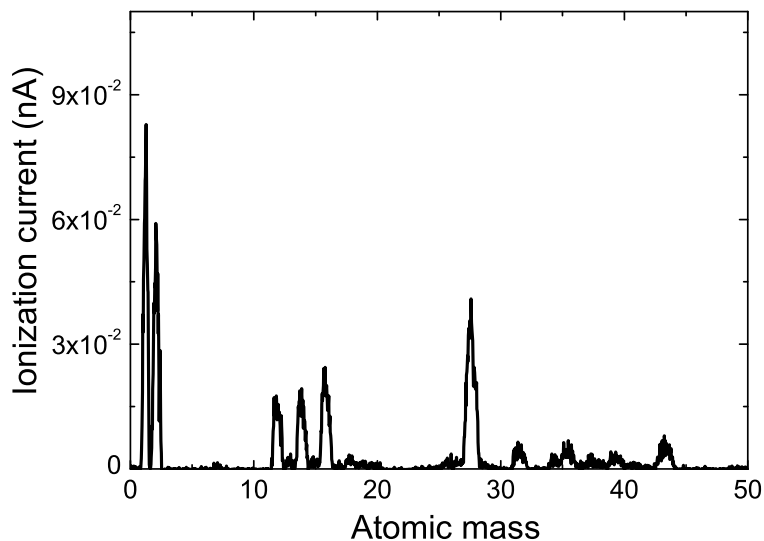


Figure 3.6: Mass spectrum indicating the gasses composition in the UHV chamber. The system is at room temperature after baking and the pressure is around  $4 \times 10^{-10}$  mbar.

mass 28 a.u. there is the sum of  $N_2$  and CO. In between 10 and 20 a.u. we find contributions from the dissociated molecules, for example  $N^+$ . From these contributions one can extract the ratio between  $N_2$  and CO at mass 28 a.u.

### 3.3 Measurement technique

The conductance is measured with a dc bias voltage in a two terminal configuration. A bias voltage is sourced from the DAC (digital to analog converter) card of the computer and the resulting current is measured using a commercial low noise current to voltage converter Stanford SR570. The data acquisition and the controlling of the measurement are done using a 16-bit ADC (analog to digital converter) card using a LabView program [53]. The contact is thinned down by increasing the voltage on the piezo element, that is also controlled by the LabView program through the data acquisition card coupled to a high-voltage amplifier. A typical conductance trace follows a step-like pattern, with plateaus for metastable configurations of the contact and jumps resulting from atomic rearrangements in the vicinity of the contact, as one can see in Fig. 3.7.

In order to find only the preferred diameters from all metastable configurations, we use a statistical analysis, by adding many conductance traces in a histogram. The conductance scale is divided into bins, and a histogram is build from a few thousands conductance traces, recorded during repeated scans of making and breaking the contact. A peak in the histogram corresponds to a

Measurement technique

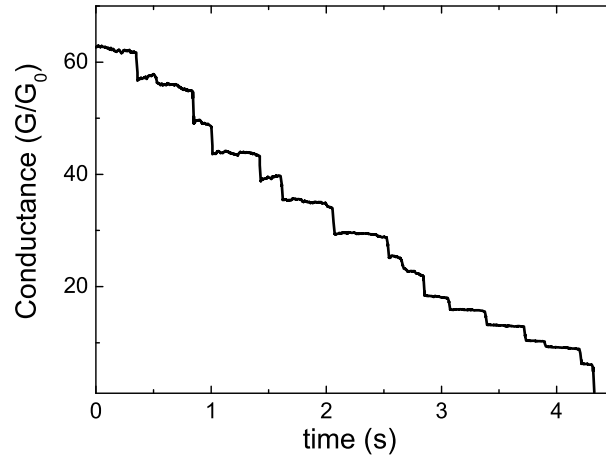


Figure 3.7: Conductance trace for Au recorded at RT-UHV. The contact breaks from a conductance of  $60 G_0$  in about 5 seconds, the last plateau being at about  $7 G_0$ .

preferred, reproducible configuration of the contact.

When searching for stable diameters, the atoms need to have sufficient mobility to select the most favorable among all possible metastable configurations. One way to enhance their mobility is by increasing the thermal energy. The optimal temperature is a given fraction of the melting temperature but one has to take into account that for nanowires the melting temperature is strongly suppressed. For example Hwang *et al.* [54] find in a calculation for copper nanowires of 34 atoms in cross section a melting temperature of 590 K (compared to bulk value 1357 K). On the high end the optimal temperature is limited by the reduced lifetime of the metastable states at elevated temperatures. Bürki *et al.* [10] give an estimate of the relevant activation energies, which are more than a factor of two higher for the noble metals as compared to the alkali metals.



# IV

## Observation of shell effects in nanowires for the noble metals gold, silver and copper

### 4.1 Introduction

When the conductance of metallic nanowires can be described in terms of a finite number of quantum modes it is expected that the degree of filling of the quantum modes has a measurable effect on the total free energy of the nanowires [18, 19, 23]. Indeed, Yanson *et al.* [6] observed that alkali nanowires, obtained by the mechanically controllable break junction (MCBJ) technique, exhibit exceptional stability for certain diameters. The series of stable diameters was shown to correspond directly to the well-known magic number series of alkali metal clusters produced in vapor jets (for a review see Ref. [3]). The alkali nanowires are very attractive from a fundamental point of view, since the electronic structure is well-described in terms of free and independent electrons, but they are not very suitable for possible applications. As suggested by research on metal clusters shell effects should be observable for many other metals. As a first step beyond the alkali metals we have chosen the noble metals. To some extent the free electron model can be applied also to noble metals nanowires, as it was proven successfully for noble metal clusters [3]. We present evidence that noble metal nanowires show certain exceptionally stable diameters of the same origin: shell filling. Firstly, we see electronic shell effects in all three metals. Secondly, the atomic shell effect appears only in gold and silver nanowires. Silver however, is exceptional, regarding the more pronounced shell structure as well as the small variation in the peak positions. [55], [56]. Remarkably, we find that for gold and silver some of the stable diameters survive even under ambient conditions, which is a big step in the direction of possible applications.

Previous experimental results on the formation and stability of gold nanowires have been reported. By the use of an electron beam thinning technique in a transmission electron microscope under ultra-high vacuum (UHV) at RT, Kondo

---

This work is published as A. I. Mares, A. F. Otte, L. G. Soukiassian, R. H. M. Smit, and J. M. van Ruitenbeek, Phys. Rev. B, **70**, 073401, (2004) and A. I. Mares and J. M. van Ruitenbeek, Phys. Rev. B, **72**, 205402, (2005)

and Takayanagi [45] observed gold nanowires that adopt a series of unusual helical configurations, which is an exceptional form of atomic shell structure. Using STM indentation experiments Medina *et al.* [43, 57] reported the observation of atomic shell effects in gold nanowires.

## 4.2 Results

The stability analysis of the noble metal nanowires is done by investigating electrical conductance using the mechanically controllable break junction (MCBJ), method described in chapter 3. The contact is thinned down in a few seconds starting from about  $100 G_0$ , that roughly corresponds to  $\sim 100$  atoms in cross section. Different breaking times in the range of 10 ms to a few minutes and different dimensions of the starting contact were tested.

### 4.2.1 Electronic shell effects

In Fig. 4.1 we show a conductance histogram for gold recorded at room temperature under UHV (UHV-RT) using a bias voltage of 100 mV. One can see a sequence of distinct peaks at certain conductance values. In the low conductance range peaks are situated close to 1, 2 and 3  $G_0$ , the conductance for 1, 2 and 3 atoms in cross section, as reported previously for gold atomic contacts [13, 58]. We see that these peaks have a relatively low amplitude, the maximum being found only at much higher conductance, at the peak of  $10 G_0$ .

For the regime of relatively thick nanowires the conductance is related to the nanowire radius by a semi-classical formula for a ballistic nanowire with circular cross section:

$$G = gG_0 \cong G_0 \left[ \left( \frac{k_F R}{2} \right)^2 - \frac{k_F R}{2} + \frac{1}{6} + \dots \right], \quad (4.1)$$

with  $k_F$  the Fermi wave vector,  $g$  the reduced conductance and  $R$  the radius of the nanowire [30], [61]. When we plot the peak positions in units  $k_F R$  as function of peak index we get a linear dependence, illustrated in the inset of Fig. 4.1 with a slope  $\Delta k_F R = 1.06 \pm 0.01$ , similar to the one obtained for alkali metals. This is an indication that the peaks in the conductance histogram are due to electronic shell filling: the nanowire chooses such diameters that give minima in the electronic free energy. We find similar periodic patterns for silver and copper nanowires as one can see in the histograms of Fig. 4.2. The periodicity of the peaks,  $\Delta k_F R = 0.98 \pm 0.01$ , is similar to gold.

### 4.2.2 Atomic shell effects

Sometimes a new series of peaks appears in the histogram as we can see in Fig. 4.3 (top) recorded for gold in UHV-RT [55]. This is related to a geometrical effect also present in clusters, namely, atomic shell filling. Certain nanowires

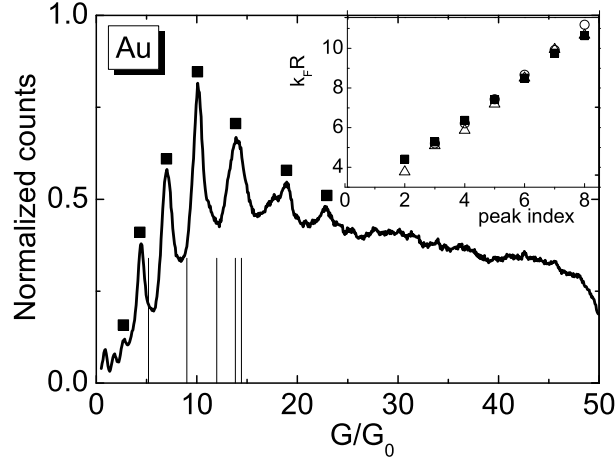


Figure 4.1: Conductance histogram for gold at room temperature under UHV constructed from 5000 individual consecutive traces, using a bin size of  $0.1 G_0$  and a bias voltage of 100 mV, giving evidence of electronic shell filling. Peak positions are indicated by squares. By bars we plot the calculated conductance for helical nanowires [59]. The inset shows the peak positions, converted to  $k_F R$  with the help of Eq. (4.1), as a function of peak index (filled squares), magic radii for gold clusters (circles) [60], and predictions of the minima of the electronic energy calculation (triangles) taken from [20]. The experimentally observed periodicity of the peaks is  $\Delta k_F R = 1.06 \pm 0.01$ .

are more stable when they adopt a crystalline order with smooth facets such as to obey minima of surface energy. This effect is expected to appear at larger diameters than electronic shell filling. Silver nanowires present this new series of stable diameters even more pronounced than gold does, with peaks up to conductance values of  $80 G_0$  (see Fig. 4.3). However, for copper we have not observed distinct atomic shell effect peaks.

The crossover between electronic and atomic shell effects is around  $10 G_0$  for gold, and at about  $15 G_0$  for silver but it can vary around this value between different measurements. This variation can be due to local crystalline orientation, a parameter that we cannot control during measurements. However for gold single crystals a more reproducible value of the cross-over was seen as it is reported in chapter 5.

We observe that during a particular measurement, after repeated cycles of making and breaking the contact, an evolution from atomic shell effect to electronic shell effect appears, as one can see in Fig. 4.4. Curves 1, 2 and 3 are histograms recorded during the same measurement containing 5000, 8000, and 20000 consecutive scans. A smooth positive background was subtracted from the histograms for better clarity. Firstly we can see that some peaks having

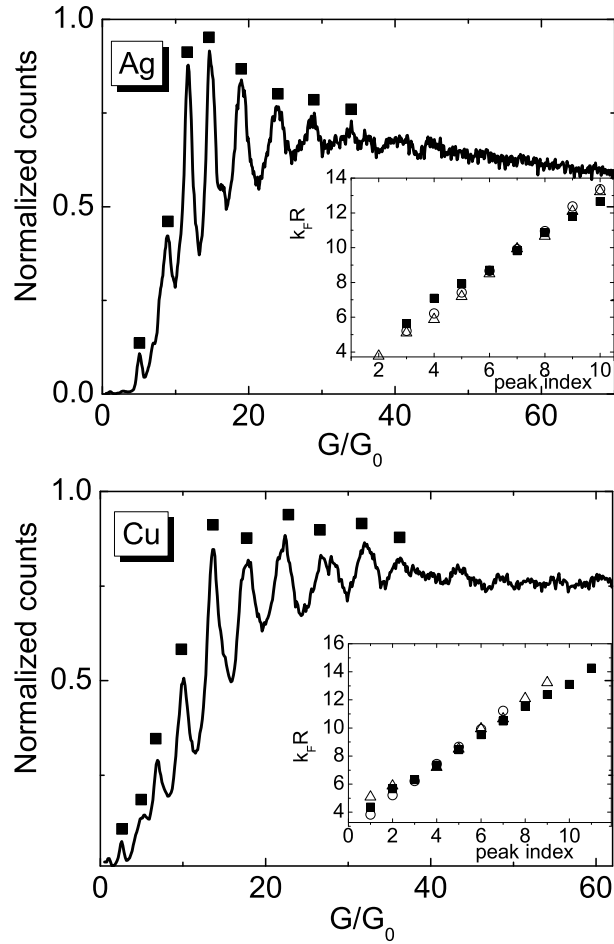


Figure 4.2: Conductance histogram for silver (top) and copper (bottom) at room temperature. The silver histogram is constructed from 10000 individual consecutive traces, using a bin-size of  $0.1G_0$ , while for copper 20000 individual consecutive traces were included and a bin-size of  $0.14G_0$  was used. In each case the bias voltage was 100 mV. The insets show the peak positions, converted to  $k_F R$ , as a function of peak index (filled squares). The slope is  $\Delta k_F R = 0.98 \pm 0.01$ , both for silver and copper. Magic radii for silver and copper clusters [60] and theoretical predictions for stable diameters in nanowires [20] are shown for comparison (circles and triangles, respectively).

atomic shell effect periodicity in histogram 1 gradually decrease their weight in histogram 2 until they disappear in histogram 3 (peaks at  $G \sim 7, 16, 20, 22, 26G_0$ , and all the peaks above this value). Secondly we see that in histogram

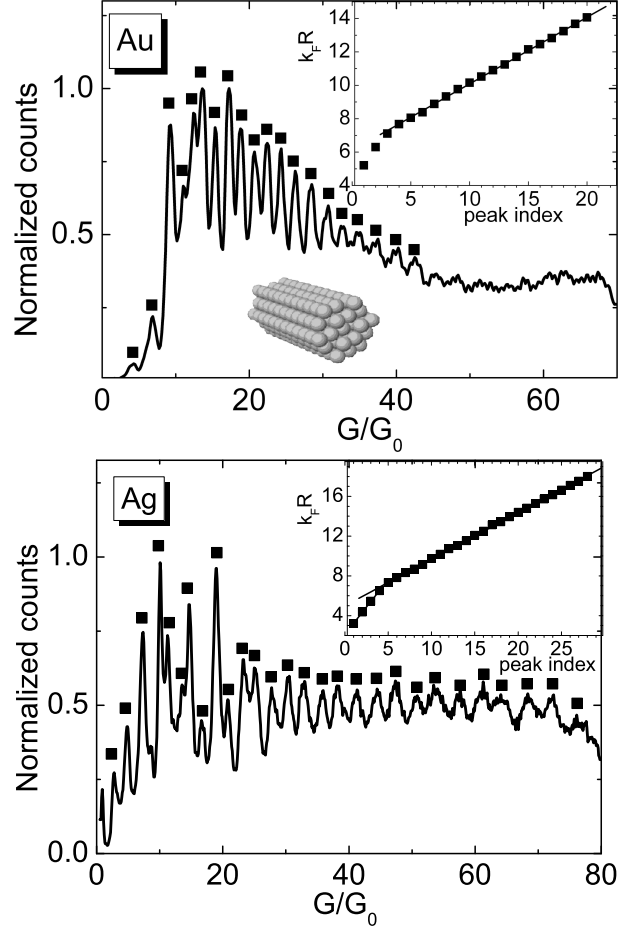


Figure 4.3: Conductance histogram for Au (top) and Ag (bottom) obtained from 3000 and 4500 individual conductance traces, respectively, recorded under UHV-RT. Peak positions as function of peak index (top insets) exhibit a linear dependence with slopes of  $\Delta k_F R = 0.400 \pm 0.002$  and  $\Delta k_F R = 0.460 \pm 0.001$  for gold and silver, respectively. The lower inset in the top panel shows a sketch of a fcc packed nanowire along the  $[110]$  axis with hexagonal cross section with four  $(111)$  facets and two larger  $(100)$  ones.

3 the peaks vanish above  $30 G_0$ , while in histograms 1, 2 they are visible up to about  $40 G_0$ . Finally in the histogram 3 we get peaks that have electronic shell effect periodicity. This transition from atomic to electronic shell effect was reported previously for alkali metals [47], and can be due to an increase in mobility of the atoms during repeated cycles of elongation/compression of the



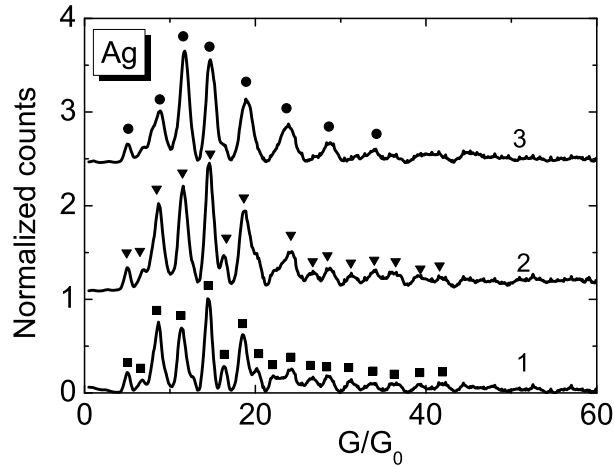


Figure 4.4: Evolution of Ag conductance histograms obtained in UHV-RT recorded at a bias voltage of 100 mV during the same measurement, containing 5000 traces (1), 8000 traces (2), and 20000 traces (3). Histogram (3) includes the traces of histograms (2) and (1). From all three curves a smooth background was subtracted.

nanowire, that can damage the faceting. Another possible reason may be that during repeated indentation the crystalline orientation of the nanowire or of the connecting electrodes changes, not being favorable anymore for faceting.

### 4.2.3 Experiments under ambient conditions

Fig. 4.5 (top) shows a conductance histogram for gold recorded at room temperature under ambient conditions. One can clearly distinguish peaks up to about  $22G_0$ , with a periodicity  $\Delta k_F R = 1.00 \pm 0.01$ , very close to the value obtained in UHV. The peak positions are close to the ones obtained in UHV, although some of them may be shifted somewhat to lower values. Similarly, a silver conductance histogram in air shows electronic shell effect periodicity  $\Delta k_F R = 1.06 \pm 0.02$  (Fig. 4.5, bottom). This brings evidence that, remarkably, shell structure survives even under ambient conditions in silver and gold. The relative intensity of the peaks is different from those under UHV. The peak close to  $1G_0$ , commonly attributed to a single-atom contact [62] has a much higher amplitude than under UHV. It has been shown by Hansen *et al.* [63] that a one-atom contact is hardly stable under UHV-RT, due to the high mobility of the atoms. However, under ambient conditions adsorbates decrease the atom mobility resulting in an enhanced stability of small contacts. This may explain also the previous results for gold atomic contacts obtained at RT in air [58]. In our conductance histograms we see that only the electronic shell effect survives in air. This is not unexpected since the atomic shell effect is a surface effect,

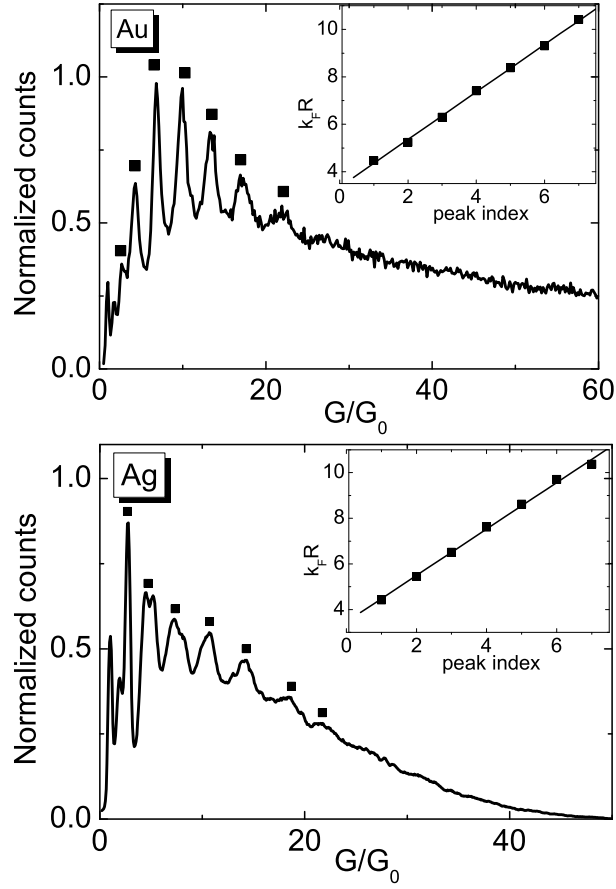


Figure 4.5: Conductance histograms for gold (top) and silver (bottom) at room temperature under ambient conditions, constructed from 2000 and 10000 individual consecutive traces, respectively, giving evidence of electronic shell filling. The insets show the peak positions, converted to  $k_F R$ , as a function of peak index with a slope  $\Delta k_F R = 1.00 \pm 0.01$  (gold) and  $\Delta k_F R = 1.06 \pm 0.02$  (silver).

therefore adsorbed species modify the surface energy and are expected to damage the faceting. Copper does not show shell effect peaks in air. The dominant feature is a broad peak close to  $1 G_0$ , as previously reported [64]. Since copper is known to be the most reactive of the three noble metals, the absence of shell structure can be caused by fast oxidation of the contact.

## 4.3 Discussion

### 4.3.1 Comparison with low temperature histograms

Conductance histograms for gold at low temperatures reported in the literature typically show only the range of low conductances that is dominated by a peak near  $1 G_0$ , attributed to a one atom contact, see e.g., results on gold at liquid helium temperatures [13]. The dominant peaks are close to 1, 2, and  $3 G_0$ . For copper and silver conductance histograms recorded at helium temperature are similar to gold having a dominant peak at or just below  $1 G_0$ , followed by two additional peaks of lower intensity [65]. There is a major difference in the origin of the low temperature peaks compared to our UHV-RT histograms. At low temperature the atoms are frozen in configurations that have a certain conductance value. In UHV-RT measurements atomic mobility plays an important role and the nanowire can self-organize such as to find the most stable configuration. Therefore, the peaks in our data reflect preferred stable diameters, and not preferred conductance like in the case of low temperature histograms.

### 4.3.2 Comparison between the three different noble metals

In Fig. 4.6 we plot the averaged values of the peak positions in histograms showing electronic shell structure recorded from different independent measurements for gold, silver and copper. We observe that the peak positions are very close to each other for the three metals. There are variations for the gold peaks indexed 6, 9 and 10. It is possible that one peak is missing in the histograms because of the supershell modulation of the peak amplitudes, [48], as it will be explained later. Although the peaks are reproducible, they show variations between different measurements. We believe that one reason can be the influence of the crystalline orientation. More reproducibility is found for gold single crystal nanowires, presented in chapter 5.

### 4.3.3 Electronic shell effect theory

The periodic pattern present in our histograms in Figs.4.1 and 4.2 is due to minima in the electronic free energy of the nanowire as function of elongation, as discussed in chapter 2. In Fig. 4.7 we compare our peak positions with the theoretically predicted stable diameters using a free electron model. We averaged 8 histograms for gold having the electronic shell effect period since we have variations in the peak positions between different measurements, as seen in Fig. 4.6. The filled squares in Fig. 4.7 are stable diameters calculated by a free electron model that takes into account the valence electron density of the metal [20]. We have used the results for Na that has the closest value to gold. We see that largely the peak position agree with the calculation. We include also the results for the purely free electron model that consider a cylindrical nanowire using a hard wall potential, discussed in chapter 2, [10, 16, 17, 23, 24]. With

Discussion

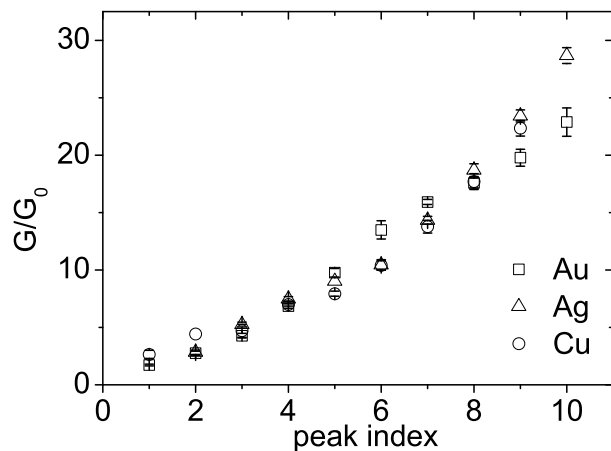


Figure 4.6: Averaged peak positions and their standard deviations obtained from conductance histograms of independent measurements for Ag (11 measurements; squares), Cu (12 measurements; circles), and Au (5 measurements; triangles).

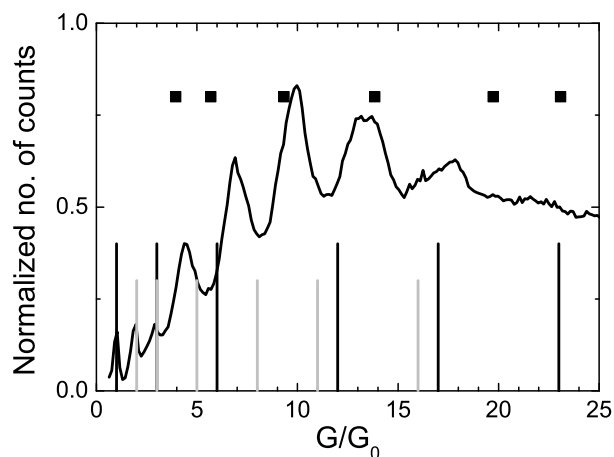


Figure 4.7: Averaged conductance histogram for Au containing 8 histograms with electronic shell effect period. The dots represent theoretical results obtained in the stabilized jellium model [20]. With black bars we plot the results for a cylindrical nanowire using free electron model with a hard wall boundary. In this case a cylindrical nanowire is considered [14], [16], [66]. The gray bars represent deformed nanowires [66].

this model one can reproduce the peak positions at 1, 3, 17  $G_0$  and the global peak separation agrees, but many peak positions are off. We mention that this

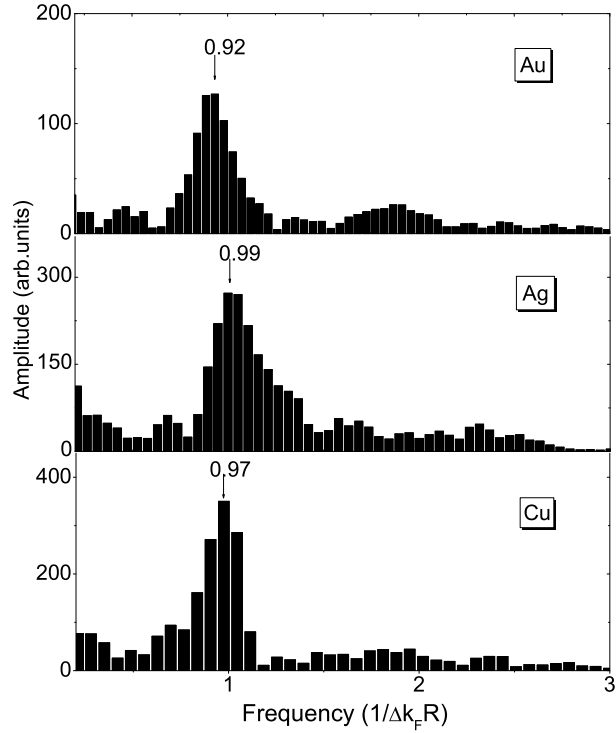


Figure 4.8: Fourier transform of the conductance histograms showing electronic shell effect for gold, silver and copper.

model was very successful explaining the electronic shell structure in alkali metals. Considering more general shapes of the nanowire, several additional stable diameters can be produced as resulting from elliptical and quadrupolar cross-sections [66] as illustrated in Fig. 4.7. Still several peaks are not reproduced correctly, as for example the peak at  $10 G_0$  that is very reproducible and has mostly the highest amplitude in the histograms. As a further possibility for this peak one could consider even higher order deformations, as it was attributed to a pentapolar cross-section [66]. We argue that the relatively high stability of this diameter will then not be completely understood since the stability decreases for higher deformations, the surface energy increasing as  $R m^2$ , where  $m$  is a parameter describing the order of the deformation. The calculations by Stafford and coworkers [10, 16, 17, 23, 24] are based on non-interacting free electron gas models. Here lies possibly the most significant difference with the calculations from Ogando *et al.*, who employ a local density approximation (LDA) to density functional theory of electron-electron interactions. This calculation includes some of the dominant effects of electron-electron interactions and this more realistic approach may explain the better agreement with our experimental data.

## *Discussion*

However Stafford and coworkers have also extended their model recently including the electron-electron interactions as described in chapter 2. They report similar results to the case this interaction was neglected.

As discussed in chapter 2 the stable diameters are determined by closed orbits inside the cylindrical walls of the wire. The orbits that proved to have the most significant contribution for alkali nanowires are the diametric, triangular and square orbits [13], [48]. The oscillating frequencies that result from these orbits are  $1/\Delta k_F R = 0.64$  for the diametric orbit and  $1/\Delta k_F R = 0.83$ ,  $1/\Delta k_F R = 0.90$  for the triangular and square orbits. A beating effect known as the supershell effect appears due to the superposition of the diametric orbit with the higher frequency orbits (triangular and square). In order to separate the oscillating frequencies in the experimental histograms we perform a Fourier transform. Since we are interested in only the oscillatory part of the spectra in Figs. 4.1 and 4.2 we subtract a smooth background. The Fourier transform for Au (Fig. 4.8, top) shows a broad peak centered at a frequency of  $1/\Delta k_F R = 0.92$ . This value is somewhat higher than what is expected from the superposition of the triangular and square orbits. This deviation can be seen as due to conductance lowering due to backscattering on defects in or near the nanowire. This correction seems to be contact size dependent, as seen by the fact that the conductance is lowered, but the calculated radii of the contact are still linear with peak index, as seen in the insets of Figs. 4.1 and 4.2. Indeed the slope is somewhat lower than what is obtained from stabilized free electron model calculation [20]  $\Delta k_F R = 1.19 \pm 0.02$ , and also by comparison to the results on potassium and sodium nanowires [13]. However deviations of the same order have been observed for lithium nanowires attributed to the same defect scattering effect [13]. In the case of silver and copper the dominant peak in the Fourier transform is centered on even higher frequencies  $1/\Delta k_F R = 0.97$  and  $1/\Delta k_F R = 0.99$ . The contribution of the diametric orbit, expected to have a frequency of  $1/\Delta k_F R = 0.64$  seems to be less important in the spectra for the noble metal nanowires as compared to the alkali metals. The selective suppression of the diametric orbit may be explained in terms of backscattering on surface roughness. For the circular orbit the incoming electron wave is perpendicular to the surface being therefore more probable to be diffusely scattered than in the case of grazing incidence orbits. Another reason can be the low resolution we have in the Fourier transform because of the limited number of peaks.

By applying a free electron model to noble metals one ignores the non-spherical shape of their Fermi surfaces. The main sheets of the bulk Fermi surface are connected by necks at Brillouin zone boundaries along the [111] orientation. However, the contribution of the necks to the oscillations in the density of states is expected to be small since their wavelength is about six times larger than the main Fermi wavelength, for gold and copper. Filling of the states in the neck will have a period six times larger than the one resulting from the states in the belly. The silver Fermi surface has even smaller deviations, resulting in a wavelength and a period of resulting oscillations of density of states eight times higher than those in the belly. Moreover the contribution of the states of the necks to the total density of states is relatively small. Therefore, in a good

approximation Au, Ag, and Cu may be considered free electron metals. Our assumption is supported by electronic structure calculations for the quantum modes in nanowires of Na and Cu [67].

#### 4.3.4 Comparison to magic numbers of noble metal clusters

We compare the values for the preferred nanowire diameters with the magic radii in clusters (circle symbols in Figs.4.1, 4.2). The radius of a cluster,  $R$ , can be obtained from its number of atoms,  $N$ , using the relation  $k_F R = N^{1/3} k_F r_s$  where  $r_s$  is the Wigner-Seitz radius of an atom and  $k_F r_s = 1.919$  [3]. The magic numbers are taken from the experiments on noble metal clusters in vapor jets [60]. We see that the agreement is very good for the magic radii in clusters and nanowires. This is at first sight unexpected due to the difference of symmetry, that is spherical in the case of clusters and cylindrical for nanowires. However, we first note that the gross features of distribution of zeros for spherical and cylindrical Bessel functions are nearly identical for not too large diameters. The difference between cylindrical and spherical geometries is expressed mostly in the relative weight of the various semiclassical orbits. For nanowires the diametric orbit is expected to have a strong contribution in the oscillation spectrum while for clusters it is negligible. Since we have very little influence of the diametric orbit, possibly as a result of surface roughness as explained above, we obtain about the same oscillation period as for noble metal clusters.

#### 4.3.5 Atomic faceting

Considering the packing model presented in chapter 2, the filling of the individual facets of the hexagon will result in a periodicity of  $\Delta k_F R = 0.476$ . This value is very close to the experimentally observed periodicity for gold  $\Delta k_F R = 0.40$  and even closer for silver  $\Delta k_F R = 0.46$ . Silver also has the largest number of atomic shell effect peaks, as one can see in Fig. 4.3. We consider atomic faceting along [110], as obtained in chapter 2 because this provides the lowest energy facets. The agreement with observations is fair. Our model agrees with the high resolution transmission electron microscope (HRTEM) imaging of gold nanowires reported by Ugarte and coworkers [37], [68].

Kondo *et al.* reported the formation and imaging of suspended multi-shell helical gold nanowires with diameters ranging from 0.6 nm and length of 6 nm [45]. Such anomalous atomic arrangements in nanowires, referred to as ‘weird wires’, had been predicted from model calculations by Gülseren *et al.* [44]. Recently the conductance of these structures was calculated by first principle methods [59]. We compare in Fig. 4.1 the calculated values of the conductance for the multi-shell helical wires with our peak positions. One can observe that the period for the first few peaks is close to the period of the calculated helical nanowire conductances, although their values do not fully coincide. However, at higher conductances the bars start to get closer together in contrast to the peaks in the histogram. We do not exclude the formation of helical nanowires,

## *Conclusions*

but we believe the peaks in the histogram are due to shell effect considering the agreement with the theoretically predicted period for the electronic shell effect [20].

### **4.4 Conclusions**

We have evidence that electronic shell filling influences the formation and stability of all three noble metal nanowires: gold, silver and copper. At larger diameters the atomic shell effect is dominant and appears in gold and silver but was not observed in copper. We observe that the shell structure is the most pronounced in silver nanowires. Regarding the electronic shell structure the Fourier spectrum reveals that the main contribution comes from the superposition of triangular and square orbits. Free electron LDA model predictions of stable radii due to the shell effect agree well with our results. Our stable diameters are in good agreement with the magic diameters of noble metal clusters. Together with the results for alkali metals [6, 7, 13, 47], we thus conclude that shell effects are generally observed for monovalent metals. The effect is sufficiently robust that it can be observed under ambient conditions for gold and silver.





# V

## Atomic packing of gold single crystal nanowires

### 5.1 Introduction

In our modelling of the atomic shell packing we made the assumption that the preferred orientation for the long wires with faceted structure to occur is [110]. Our assumption agrees with Monte Carlo simulations that find preferential stability for [110] [41]. Also HRTEM (High resolution transmission electron microscopy) experiments [68], [37], [69] reveal the formation of longer nanowires along [110] compared to the other main orientations [111] and [100].

By performing experiments on single crystals we mainly want to verify this hypothesis. Secondly we want to investigate the reproducibility of the peak positions and the cross-over between electronic and atomic shell structure compared to poly-crystalline wires. Another question is whether the initial orientation of the bulk wire is preserved at the nanoscale and for how long this will survive during repeated deformations of the nanowires. Last but not at least we want to compare the three main crystalline orientations [110], [100] and [111] and to find out what the origin of the peaks will be for the latter two and which of them will be more favorable for electronic shell effect long series of peaks that we often see. We indicate an orientation as [110]. We mean with this that the axis of the contact is originally aligned with the [110] axis.

### 5.2 Images of gold nanowires

We compare our results with the conclusions from the HRTEM imaging of gold nanowires performed by Rego *et al.* [68]. An electron beam is focused on a gold thin film on very small spots where it will produce holes. The procedure is repeated until a thin nanowire will bridge two holes. The nanowires are imaged with atomic resolution using a HRTEM. With the means of the geometrical Wulff constructions [70] Rego *et al.* can determine the structure of the nanowires. The authors find that before rupture the nanowire can have only three possible configurations oriented along [110], [111] or [100] crystalline axis, as seen in Fig. 5.1. As a function of the crystalline orientation of the nanowire the last contact before breaking will be different for the three cases. Along [110] a long wire is expected to form. This can be about 5 times longer than in the

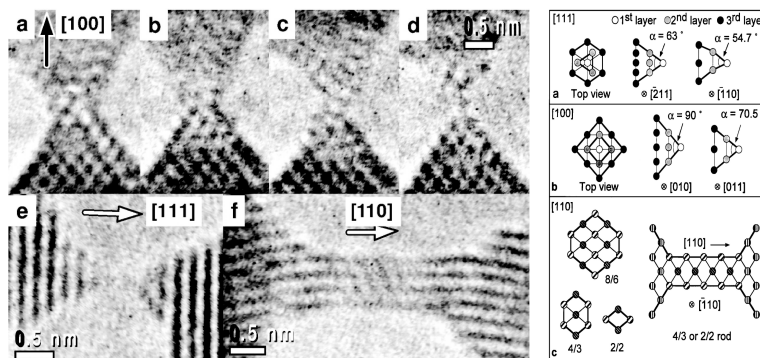


Figure 5.1: HRTEM images (left) and proposed atomic geometry (right) for gold nanowires oriented along  $[110]$ ,  $[100]$  and  $[111]$  crystalline orientation. Reproduced from [68], [37].

case of the other two orientations,  $[100]$  and  $[111]$ , as one can see in Fig. 5.1. This wire will be faceted and one of the proposed cross-sections labelled  $4/3$  in Fig. 5.1 corresponds to our proposed hexagonal cross-section considered in the packing model used in chapter 2. The thinning down of this structure is deduced based on the fcc crystalline structure and the Wulff construction. The conductance of these structures is calculated using the extended Hückel theory, that takes into account the atomic arrangement. The results show that nanowires along  $[110]$  axis will thin down such that it is impossible to end with an one atom contact, that has a conductance close to  $1 G_0$ . They are expected to break when they are two or three atoms thick. The calculated conductance for the structure  $4/3$  from Fig. 5.1 is  $4.5 G_0$  while for  $2/2$  is  $2.8 G_0$ . Thinner nanowires would have the conductance of around  $2 G_0$ . Similar considerations are used for describing the evolution of the nanowires oriented along the other two crystalline axis  $[100]$  and  $[111]$ . In the case of  $[100]$  orientations the contact will be much shorter having a pyramidal shape and the opening angle is unfavorable to form a contact of 2 atoms (seen in the proposed atomic geometry shown in Fig. 5.1), but the last plateau is predicted to be at  $1 G_0$ . Also it should appear a conductance of  $3 G_0$ . Also in the case of the  $[111]$  orientation shorter wires are formed that in the breaking process will go through configurations having conductances of about 1, 2 and  $2.6 G_0$ .

### 5.3 Experimental details

In the next sections we present measurements performed in UHV-RT on gold single crystal wires. The measurements are performed using the UHV-MCIBJ technique. In this case the sample preparation procedure needs more care than the poly-crystalline wires. The wires of 1 mm diameter were cut by spark erosion

from a slab. The central notch of 0.5 mm diameter was also cut in this way, this procedure avoiding mechanical stress on the wires that can distort them and damage the crystalline structure. After this the single crystals were wet etched in a concentrated aqua regia solution for an hour. The etching rate was determined to be about 100  $\mu\text{m}$  per hour. The etching of the samples is done in order to remove any defects on the surface that can propagate in the bulk and to ensure a cleaner surface. The mounting of the samples has to be done also with caution in order to not scratch the surface and produce defects that will propagate in the bulk of the wire. The MCBJ design was adapted to the use of thicker samples by using special substrates that have a 0.5 mm groove in the middle where the single crystal will be fitted in. The initial breaking is done slowly such that the sample is not bent too far and the recovery is done with care in order to not push together the two broken parts of the sample and to mismatch the orientations of the two sides.

## 5.4 Single crystal nanowires along the [110] orientation

Fig. 5.2 shows two histograms recorded in UHV at RT for a single crystal gold wire along the [110] axis, at a bias voltage of 40 mV. One can see a series of distinct peaks up to a conductance of about  $20 G_0$ . Starting from  $10 G_0$  the peaks have a period related to atomic shell effect,  $\Delta k_F R = 0.4$ , as found from the plot of the peaks position as a function of their index, shown in the inset. Below  $10 G_0$  there are only three peaks that are related to electronic shell filling. In Fig. 5.2a) there are no clear peaks in the low conductance regime, below  $5 G_0$ . This observation agrees with the interpretation of Rego *et al.* [68] concerning the thinning down of gold nanowires depending on the initial crystalline orientation. As one can see in Fig. 5.2b), we sometimes obtain histograms with a last peak at  $2 G_0$  that would also agree with the predictions of [68]. In general a better reproducibility of the peak position has been seen for the single crystal nanowires along [110], as compared to the poly-crystalline ones. Moreover the cross-over between electronic and atomic shell effect peaks is very reproducible, being at about  $10 G_0$  in 11 of 13 histograms showing the atomic shell effect period. As we expected, the atomic shell effect oscillation dominates for these wires, since 75% of the histograms show the atomic shell effect period, being similar to the histograms shown in Fig. 5.2. 10% show an electronic shell structure and 15% have a different slope. The histograms that are an exception were recorded after some time from the beginning of the measurement, therefore it is possible that during repeated indentation the orientation of the nanowire changes or that contamination starts to accumulate. Nevertheless, the transition is reversible, since the atomic shell effect period can be recovered, after deep indentation. When continuing taking histograms for a given contact there is no transition from atomic to electronic shell structure, in contrast to what was seen in the case of poly-crystalline gold and silver nanowires, reported in chapter 4. This

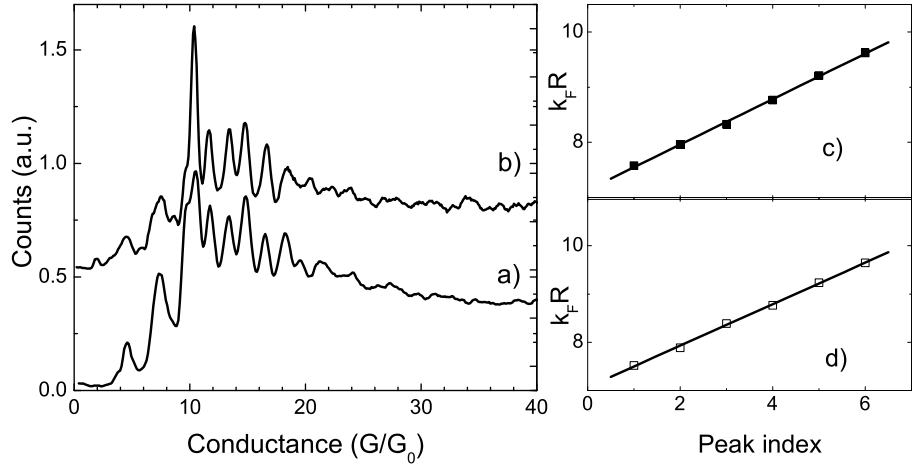


Figure 5.2: Conductance histograms for single crystal gold nanowires oriented along  $[110]$  axis recorded at RT-UHV. The peaks positions are remarkably reproducible. The periods are the same,  $\Delta k_F R = 0.42 \pm 0.02$ , found in c), d), where the peaks positions in  $k_F R$  units is plotted vs the peak index (c) for histogram a) and d) for histogram b).

indicates that in the case of single crystal nanowires the orientation can be easier preserved.

The appearance of the atomic shell effect peaks depends on the direction of forming the contact, being observed only for the breaking process, when the wire is pulled. We could see that for a histogram recorded in the pushing process no clear peaks could be distinguished. This is not unexpected, since other reports show that shorter nanowires are formed in the reversing process [71].

We have analyzed the dependence of the histograms with the applied bias voltage. Below 200 mV no clear dependence with the bias voltage was observed. Above 200 mV the histogram start to change, as one can see in Fig. 5.3. Firstly, the number of peaks decreases and the atomic shell effect period disappears. Secondly the peak at  $1 G_0$  increases in amplitude for larger bias voltages, especially seen for the histogram recorded at 400 mV. This increase is more general, being observed for the other two crystalline orientations investigated,  $[111]$  and  $[100]$  as well as for poly-crystalline wires. Finally the peaks that still survive, the ones around 4, 7, 10 and  $12 G_0$  are shifted to lower conductance values by increasing the bias voltage. A possible mechanism to explain the different conductance histograms would be the structural changes in the nanowire, hypothesis supported by recent TEM imaging of gold nanowires at room temperature [72]. The nanowires are formed with a STM and their shape is imaged for different bias voltages. With increasing the bias voltage the nanowire shortens, due to the elongation of the supporting electrodes, possibly due to thermal

*Single crystal nanowires along the [110] orientation*

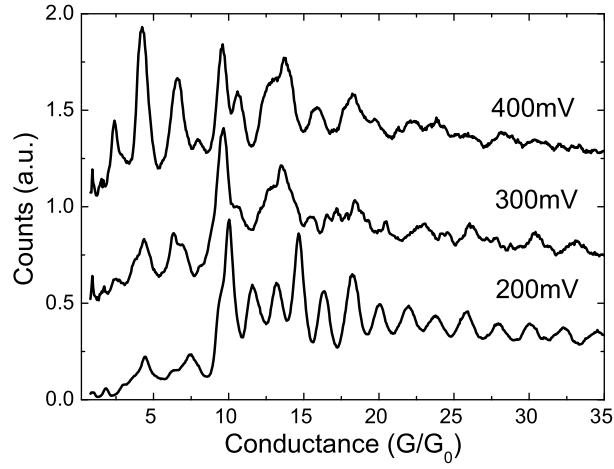


*Figure 5.3: Bias dependence of the conductance histograms for gold nanowires oriented along [110] axis recorded at room temperature in UHV.*

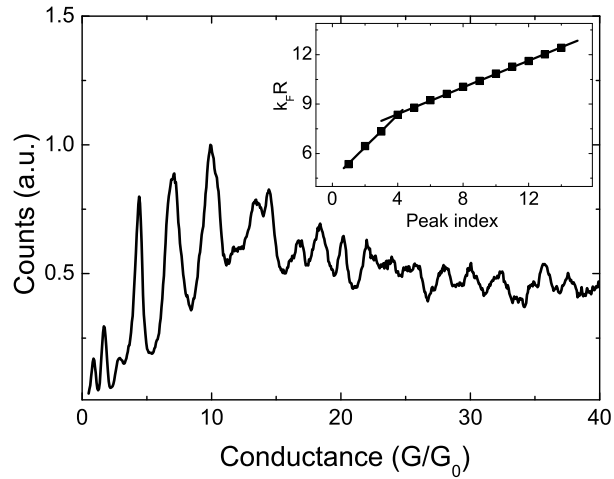


*Figure 5.4: Conductance histogram recorded in nitrogen atmosphere at room temperature using a bias voltage of 200 mV. The period of the peaks gives the atomic shell effect oscillation, as found from the linear fit in the inset,  $\Delta k_F R = 0.41 \pm 0.02$ .*

heating. Since atomic shell effects imply a long nanowire, this can be a possible explanation of the transition to a different series of peaks with increasing the bias voltage, seen in Fig. 5.3. The shift of the peaks to lower conductance values can be due to scattering on defects that would eventually form in the structural

change of the nanowire.

In order to find out what is the influence of surface adsorbates to the stability spectrum of nanowires we have introduced nitrogen gas in the UHV chamber. A histogram recorded for a [110] oriented single crystal in nitrogen atmosphere at a pressure of the order of the atmospheric pressure is shown in Fig. 5.4. Remarkably the peaks having atomic shell effect period survive. The period of the peaks is found in the inset as  $\Delta k_F R = 0.41$ . The overall shape of the histogram is somewhat different than in UHV, namely the peaks below  $10 G_0$  have a significant amplitude, as well as the peak at  $1 G_0$ . This observation is similar to what we have seen for poly-crystalline gold in air and reported before by Hansen *et al* [63]. The increased stability of small diameters in air or nitrogen atmosphere can be due to the decrease in the atomic diffusion due to surface adsorbates.

## 5.5 Comparison between the three orientations: [110], [100] and [111]

As it is shown in the analysis below, similar results to the previously explained are obtained for the other two orientations [100] and [111]. The period of the peaks is largely the same. For the [100] orientation 53% of the total recorded histograms show an atomic shell effect period, 24% show electronic shell effect and 23% a different slope or unclear peaks. In the case of the [111] orientation 44% of the histograms have an atomic shell effect period, 33% have electronic shell effect period and 22% have a period different from the first two. Thus, still the most dominant feature is the atomic shell effect periodicity, that has about the same slope as in the case of [110]. Therefore in order to find the differences to the [110] orientation one has to look in more detail. In the next subsections we look at the peak positions and the occurrence of the peaks in the low conductance regime 1, 2, 3  $G_0$  following the analysis of [68]. We have indications that for [100] and [111] during the measurement an evolution to a different orientation occurs, very likely [110] orientation, since the peak period is similar. We will focus on the histograms that show atomic shell structure for the comparison to [110]. We will perform a time evolution analysis identifying about 3 regimes. The beginning histograms are the first 1000 scans from the beginning of the measurements. The intermediate histograms are those where the atomic shell effect peaks are already clear and distinguishable but their position is very scattered and they vary with respect to the [110] orientation. The end histograms represent the histograms where a more stable series of peaks was achieved.

### 5.5.1 Beginning histograms

In the case of [110] orientation the atomic shell effect is present from the beginning of the measurement in most of the cases. One can see in Fig. 5.5 an example of a beginning histogram (the lower curve) and its evolution with time.

Comparison between the three orientations:  $[110]$ ,  $[100]$  and  $[111]$

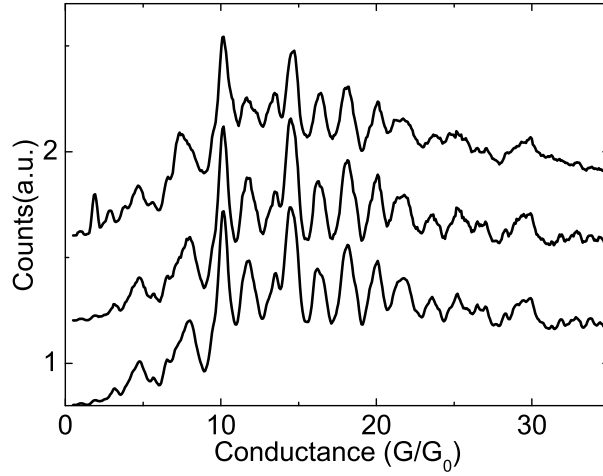


Figure 5.5: Evolution of the histograms for the  $[110]$  orientation recorded at the beginning of the measurement for the same sample. For every histogram going from the bottom to the top additional 1000 scans are included.

The peak positions are very reproducible for the three histograms. The period of the peaks is the atomic shell effect period, in this case around  $\Delta k_F R = 0.41$ . We have seen for  $[110]$  orientation that the tendency is to get very quick to this period. Concerning the low conductance peaks, we find from the beginning either the situation with no clear peaks below  $5 G_0$  or a peak at  $2 G_0$ , as it can be seen in the histograms from Fig. 5.5. We find that the two situations are in almost all of the histograms met, even if sometimes a small contribution is seen at  $1 G_0$ .

For the  $[100]$  orientation the first 1000 scans show either electronic shell effect period, (3 out of 5 histograms) as one can see in Fig. 5.6 a), or not a defined period. The histogram in Fig. 5.6 b). is an average over several beginning histograms for different samples. An electronic shell effect period is found,  $\Delta k_F R = 1.05$ . Agreeing with the interpretation of Rego *et al.* [68], we see that for the  $[100]$  orientation in the first histograms the peak at  $1 G_0$  is prominent. In time the histograms change towards the atomic shell structure and the peak at  $2 G_0$  increases its weight, as one can see in Fig. 5.6 a). In the histograms that have a faster transition to atomic shell structure there is no clear peaks in the low conductance regime.

The beginning histograms for the  $[111]$  orientation are similar to the  $[100]$  case. Thus 3 out of 5 have electronic shell effect period and the other 2 have directly atomic shell effect. One can see in Fig. 5.7a) examples of starting histograms. In Fig. 5.7b) is shown an average histogram for the  $[111]$  orientation. One gets two periods:  $\Delta k_F R = 1.05$  and  $0.46$ . The somewhat larger period for the atomic shell effect might be due to the superposition of the peaks from



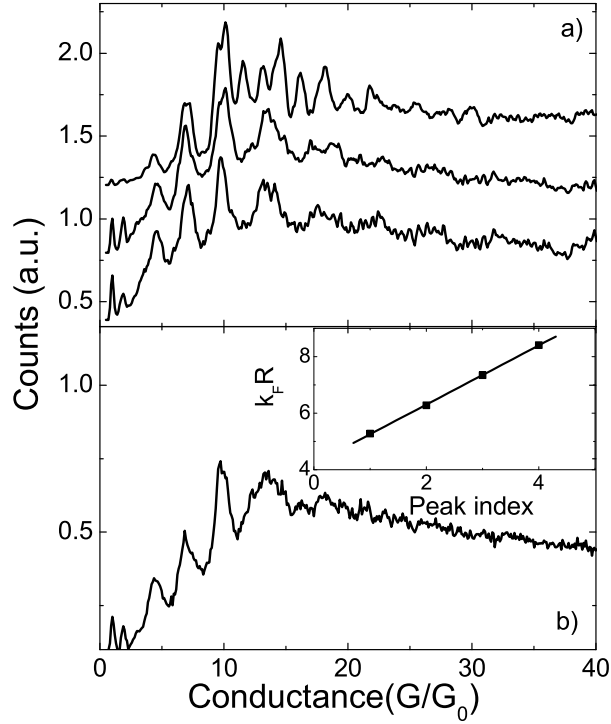


Figure 5.6: a) Evolution of the histograms for the  $[100]$  orientation recorded at the beginning of the measurement for the same sample. For every histogram going from the bottom to the top additional 1000 scans are included. b) Average of five histograms for the  $[100]$  orientation for the beginning of the measurement. The period of the peaks found in the inset is  $\Delta k_F R = 1.05 \pm 0.03$

histograms with the two periods. For this orientation (Fig. 5.7 a)) we see a series of 1, 2, 3  $G_0$  and sometimes also  $2.5 G_0$ . This series of peaks appears together with the electronic shell effect peaks which is more pronounced in the  $[111]$  case. As one can see in the upper curve from Fig. 5.7a), when these peaks are missing the histogram has a different series of peaks, as similar to atomic shell structure.

### 5.5.2 Intermediate regime

The intermediate histograms are those where in case the atomic shell effect appears, the peaks are already clear and distinguishable but their position is still scattered. In Fig. 5.8 b) we compare a histogram recorded for the  $[100]$  orientation from this regime with the histogram for  $[110]$  from Fig. 5.2. One can see that the peaks for  $[100]$  start to deviate starting from about  $10 G_0$ . The

Comparison between the three orientations:  $[110]$ ,  $[100]$  and  $[111]$

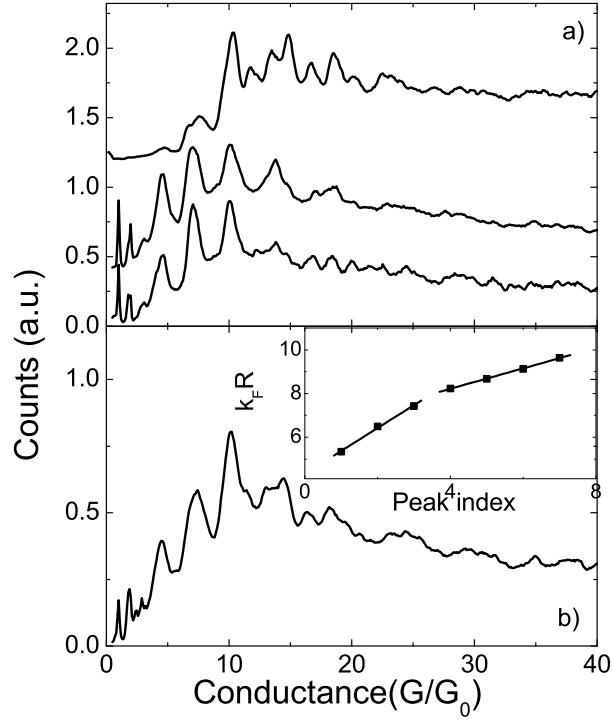


Figure 5.7: a) Beginning histograms for  $[111]$  orientation. The lower histogram was recorded based on the first 1000 traces and the one above will include it plus the next 1000 traces. The two lower histograms show peaks at 1, 2 and 3  $G_0$  and have an electronic shell effect period. The upper curve is for a different sample and it has the atomic shell effect period. b) Average of five histograms for the  $[111]$  orientation for the beginning of the measurement. Inset: Peaks period  $\Delta k_F R = 1.01 \pm 0.06$  and  $0.46 \pm 0.07$ .

shift to lower conductance values is increasing with increasing the conductance, until the peaks are completely out of phase at conductances around 16  $G_0$ . One can see in the three histograms from Fig. 5.8 a) that the peak positions vary more for this orientation than in the case of  $[110]$  (Fig. 5.2).

For single crystals along the  $[111]$  orientation we observe a similar behavior: after a few thousands scans, the histograms change to showing atomic shell effect period (Fig. 5.9 a). The case of  $[111]$  is the most probable for the electronic shell effect to appear, at the beginning of the measurements and also after the atomic shell effect. We show such an example in Fig. 5.9 b). When compared to  $[110]$  the peaks are shifted to lower values for  $[111]$ , similar to the histograms for  $[100]$ , see Fig. 5.10. Also their positions in different histograms vary. If one averages several histograms for different samples, the standard deviation in the

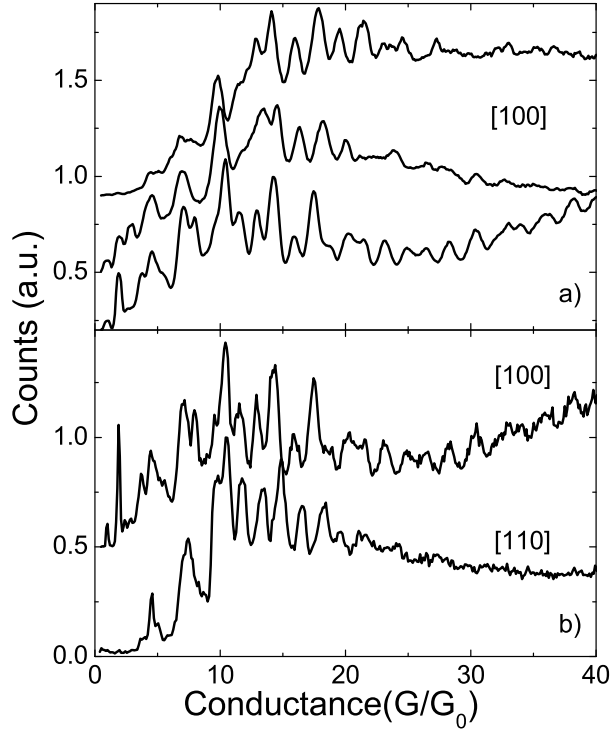


Figure 5.8: a) Comparison between different histograms for the [100] orientation in the intermediate regime, when the atomic shell structure starts to develop. b) Comparison between a histogram for the [100] and the [110] orientation.

peak positions will be in average  $\pm 0.4 G_0$  for the [100] orientation,  $\pm 0.3 G_0$  for [111] and lower for the [110] orientation,  $\pm 0.15 G_0$ .

### 5.5.3 Final histograms

Final histograms are defined as the histograms where the peak positions become much more stable having little variation. In Fig. 5.11 a) we compare the evolution of the histograms for several samples for each orientation.

In the case of [110] the dominant behavior is the atomic shell effect and there are only three exceptions. For [100] there are more transitions to electronic shell structure and back. We can identify also different values for the slopes that can be a result of the superposition of the electronic and atomic shell effect peaks. [111] shows the highest preference for electronic shell structure among the three orientations. In b) we can see a histogram made out of the periods found for the histograms. [110] has less variations and the distribution around  $\Delta k_F R = 0.4$  is sharper indicating more reproducibility for atomic shell structure.

Comparison between the three orientations:  $[110]$ ,  $[100]$  and  $[111]$

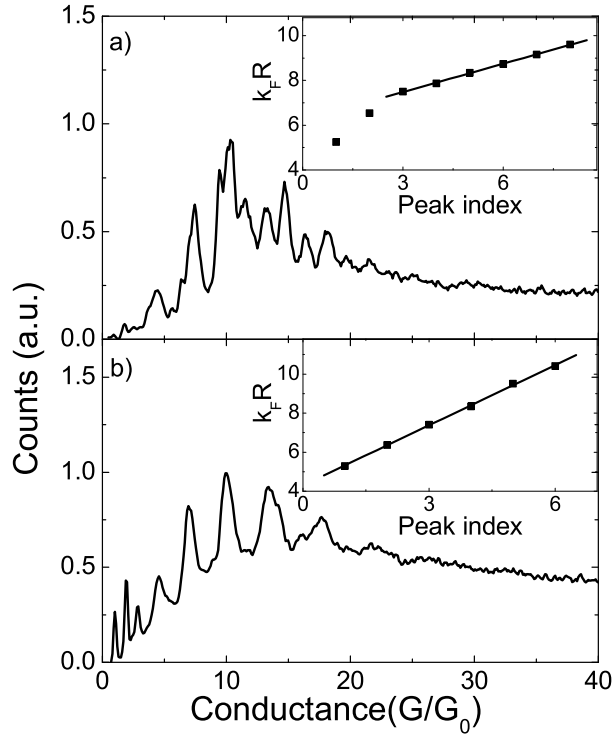


Figure 5.9: Conductance histograms for the  $[111]$  orientation in the intermediate regime for two different samples. The peak periodicity for the top histogram is the one expected for atomic shell structure, from the period found in the inset  $\Delta k_F R = 0.42 \pm 0.04$ . The bottom histogram shows electronic shell effect with a period  $\Delta k_F R = 1.05 \pm 0.02$ .

Sometimes a histogram with a large number of peaks occurs, normally after many cycles of making and breaking. This can indicate that the nanowire is mechanically annealed finding a more stable structure [71]. In the earlier histograms the peaks at high conductance values might be suppressed because of large variations in the conductance due to defect backscattering. Long series of peaks with atomic shell period occurs for all the three orientations, as one can see in Fig. 5.12. In the case of  $[110]$  the peak positions is more reproducible than in the other two cases, where they start to deviate at larger conductance values.

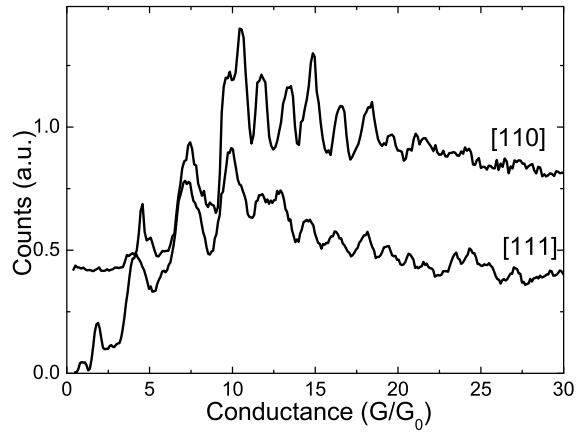


Figure 5.10: Comparison between a histogram for the [111] orientation with one for the [110] orientation in the intermediate regime. The peaks in the first are shifted to the left as compared to the latter.

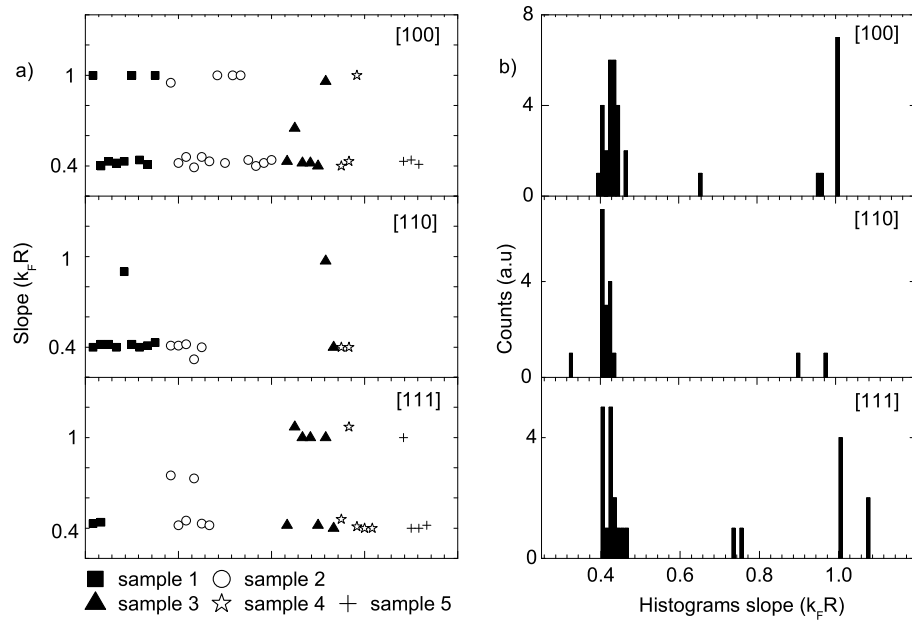


Figure 5.11: a) Evolution of the histograms with time. On the x axis is plotted the histogram number for different samples. On the y axis is plotted the periodicity of the given histogram.  $\Delta k_F R$  around 0.4 correspond to atomic shell effect and around 1 to electronic shell effect. b) Histograms of the slopes value for the three orientations.

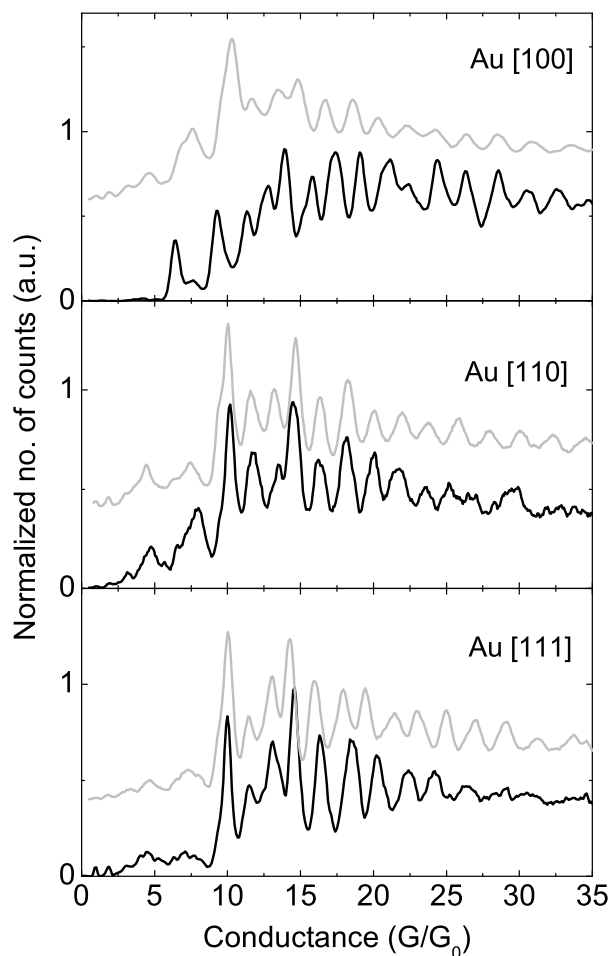


Figure 5.12: Histograms with peaks up to high conductance values for all the three orientations in the final regime.

## 5.6 Discussion

There can be several possible causes for the relatively large variation in the peak positions and their shift to lower conductance values in the case of [100] and [111] compared to the [110] orientation. We propose that a possible mechanism is back-scattering on defects or nanowires edges. It is suggested by density functional theory calculations [42] the occurrence of a so-called mixed structure. While pulling the wire, the neck does not evolve on the whole length from one long wire with a uniform cross-section to the next stable one, but the new structure appears before the previous one has completely disappeared.

The conductance is lower because of backscattering on the nanowire boundaries. Another possible cause of enhanced backscattering can be that along [100] and [111] more disordered nanowires are formed compared to [110], as it was observed by HRTEM [68]. If we assume that a transition to a different orientation occurs, defects are created in the structural change of the nanowires. Finally another possibility is that along [100] and [111] completely different structures form. These will have different packing, hence different peak positions, but by coincidence the same final periodicity. Also in this case we need to assume that defect scattering occurs in order to understand the large variation of the peak positions.

A DFT calculation predicts that for the nanowires along the [100] axis is energetically more favorable to relax to a [110] orientation [73] under its own surface stress. The results will predict this type of behavior for Ag, Cu while for Au a transition to a bct (body centered tetragonal) lattice is predicted. There are some differences between the calculation and our experiments that encourage our suggestion that the nanowires will keep their fcc structure although eventually their orientation changes during repetitive elongations. Firstly, in the calculation an infinite long nanowire is considered, while in the experiment the nanowire is connected to the leads and their orientation should match. Secondly the HRTEM imaging reveal that the nanowire keeps its fcc orientation [37], [68], [69]. Finally in our experiment the nanowires are under elongation stress, while the DFT calculation investigated the stability of the nanowires under shear distortions. Although the results of [73] do not match perfectly our conclusions, they support qualitatively our suggestion that transitions from [111] and [100] to [110] orientation occur.

## 5.7 High bias voltage

One expects to have a critical value for the bias voltage, over which a stable atomic sized contact is not possible due to power dissipation. Indeed immediately after increasing the bias to 400 mV or higher the contact breaks very sudden for few hundred scans. After this, in the low conductance regime the contact will survive for very long time while pulling it. Such breaking traces are shown in Fig. 5.13. The breaking time is more than 10 times larger than in the case of a bias voltage of 100 mV. The traces will break relatively fast in the high conductance regime and much slower below  $1 G_0$ . Sometimes some plateaus can appear at fractional values of conductance, as one can see in the enlarged region from Fig. 5.13 a). It is even more remarkable the stability of these contacts when they are left to evolve by themselves. Fig. 5.13 b) shows a stable contact around  $1 G_0$  that stays around this value for almost 30 minutes. Here the contact is not pulled below  $1.2 G_0$ . Finally the contact was broken by manually increasing the voltage on the piezo element.

---

This work was done in collaboration with M. R. Calvo, Universidad de Alicante, Spain

### High bias voltage

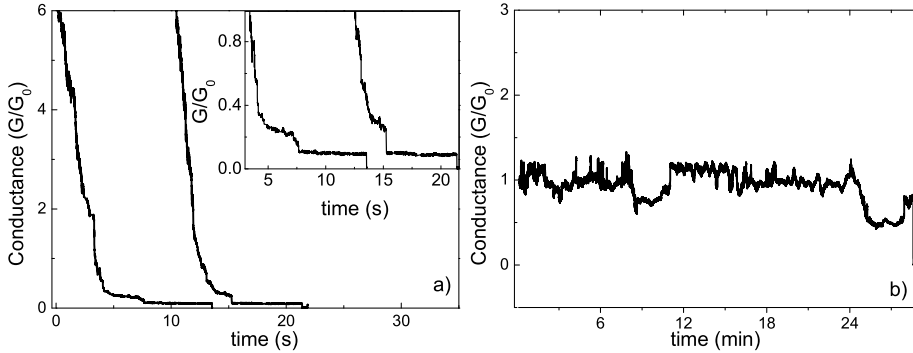


Figure 5.13: a) Breaking traces for a single crystal along [111] when applying 500 mV bias voltage. The contact is externally elongated. Inset: enlargement of the low conductance regime. b) Stable contact having a conductance around 1  $G_0$  when biased with 600mV. The contact is left to evolve by itself, without pulling it below 1.2  $G_0$ .

We emphasize that we do not see any sign of contamination or any similar behavior for bias voltages lower than 400 mV. In this case a trace will break very sudden in the low conductance regime, staying only of the order of ms at conductance plateaus below 10  $G_0$ . After the stable contacts are obtained with high bias if going back to low bias voltage the transition is reversible. The transition is not spontaneous, only after few indentations the "clean" behavior is recovered and the fractional conductance values will completely disappear. From these measurements we have an indication that these stable contacts with conductance below 1 quantum unit are due to contaminant species adsorbed. Although we have a UHV system, still some species are present as one can see in a mass spectrum in chapter 3 in Fig. 3.6 like  $H_2$ , C, CO,  $N_2$ ,  $O_2$ . It is still not understood how the high bias voltage enhances the binding of contaminants species to the contact. We have observed that the voltage where this stable contacts start to appear is well defined, being around 400 mV and their occurrence is enhanced by the process of making and breaking the contact. No such behavior was observed when one keeps the electrodes separated at tunnelling distance and applies a high bias voltage.

The conductance of these exceptionally stable contacts depends on the bias voltage. Fig. 5.14 shows the I-V characteristic of such a contact for a gold poly-crystalline sample, that was obtained after the contact was stabilized by repeatedly making and breaking it with a bias voltage of 400 mV. One can see in Fig. 5.14a) that the I-V is not linear. In b) we show the differential conductance as a function of the bias voltage. We add an ac modulation signal of 10 mV amplitude and 1 kHz frequency to a DC voltage. The differential conductance is recorded by a lock-in amplifier simultaneously with the DC current plotted in a). One can see that the differential conductance increases almost linear with



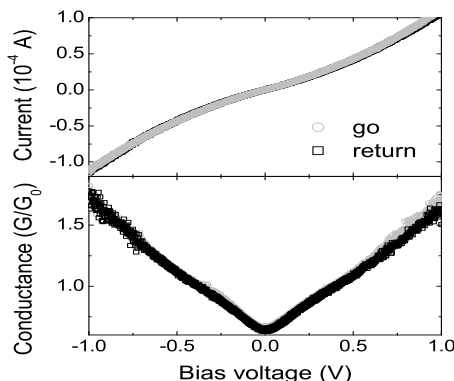


Figure 5.14: *I-V* characteristic and the differential conductance as a function of the bias voltage recorded simultaneously for an exceptionally stable contact. The voltage is swept back and forth and both curves are shown (go and return). The stable contacts obtained at 400 mV have a conductance at 400 mV of  $1 G_0$ .

the voltage with a slope  $dG/dV \sim 1 G_0/V$ . The linear fit is not perfect but when considering a quadratic term this would have much less weight. The bias voltage is swept back and forth and one can see that the curves are almost identical. This gives the indication that the contact remains nearly unchanged during sweeping the voltage. Similar linear increase for the conductance was observed for different values of the starting contact, in between  $0.2$  and  $4 G_0$ .

The linear dependence of the conductance with the bias voltage is somewhat unexpected. One possible mechanism would be tunnelling through a contamination layer. In this case a parabolic dependence of the conductance with the bias voltage is expected, since the tunnelling barrier will be overcome for a certain voltage. Nonlinearity in the current-voltage curves was seen in the experiment by Yoshida *et al.* described in the previous section. The *I-V* curves have a cubic dependence starting at about  $0.1$  V. This is attributed to thermal expansion of the connecting electrodes that will increase the cross-section of the nanowires.

Since both assumptions are not consistent with our observations we propose a different mechanism. If an adsorbate layer is trapped in between the metallic tips, this acts as a capacitor. Due to the high bias voltage applied, an electrostatic force will act between the two tips. An estimated order of magnitude for this force will be of about few nN. The measured force for the atomic contacts that will break an atomic bond is about  $1$  nN [2]. The electrostatic force is large enough to produce atomic rearrangements resulting in an increase of the area of the tips, and at the same time compress the adsorbate layer between them. Since the area of the adsorbate increases and its thickness decreases, an increase in the conductance is expected.

## 5.8 Conclusions

We have investigated by conductance measurements the formation and stability of gold nanowires for single crystals along three crystalline orientations: [110], [100] and [111]. As expected for the [110] orientation the predominant feature is the atomic shell effect. We obtain remarkable reproducibility of the peak positions and the cross-over between electronic and atomic shell effect. For the other two orientations we have indications that a transition occurs, more likely towards the [110] orientation. This assumption is in agreement with the expectations that [110] is the preferred orientation [41], [68]. Our observations agree to some extent to other predictions that relate the peaks in the low conductance regime ( $1, 2, 3 G_0$ ) to the crystalline orientation [68]. In this regime we see different series of peaks for electronic and atomic shell structure. The distinction between the three orientations is not as clear as we have hoped. The results support the idea that the local atomic arrangement changes under the influence of the contact making and breaking cycles. Together with the differences observed in the beginning histograms this provides evidence that the variations in histograms for poly-crystalline wires can be attributed to various atomic packing. Our interpretation of the transition in time for the [111] and [100] to [110] orientation agrees to some extent with some recent theoretical predictions [73].

As a side result we have discovered an unexpected stabilizing effect at high bias voltage. The conductance of the stable contacts can have any value, not limited to integer multiples of the quantum unit. The process is reversible: when lowering the bias voltage the contact will be cleaned and the normal gold behavior is recovered. These contacts are very likely to be contaminant species adsorbed on the contact, although their conductance dependence on the bias voltage is still yet not completely understood.



# VI

## Shell structure in multivalent metals: aluminum and magnesium

### 6.1 Introduction

For noble metal nanowires we have obtained evidence of two series of stable diameters related to electronic and atomic shell filling, similar to alkali metals. Inspired by the research done in metal clusters we extend our investigation to multivalent metals: magnesium and aluminum. The bulk Fermi surface for magnesium and aluminum has higher deviations from the free electron like sphere, since the electron-lattice interaction has a significant contribution. In nanowires the transversal confining potential competes with the periodic potential of the lattice and one would expect that the latter will give a correction that becomes negligible as the specimen size decreases. This is observed in aluminum and magnesium clusters, where magic numbers expected from the simple jellium model are identified. Photoelectron spectroscopy studies give evidence that electronic shell closure is present in Al clusters up to clusters formed of 75 atoms [74]. The jellium model using a spherical confining potential can explain to some extent the results on Al clusters [4]. For clusters larger than 75 atoms the geometrical packing influences their stability.

Magnesium has the particularity that its  $s$  shell is completely filled. In low dimensional systems, like clusters, a gap occurs between the  $s$  and  $p$  band, and the clusters are non-metallic. The transition to the metallic state occurs when the number of atoms in the cluster increases inducing broadening of the  $s$  and  $p$  band leading to an overlap. This transition is found also for Al clusters where the  $s - p$  hybridization is found to appear at cluster sizes of 9 atoms. For Mg it occurs at larger sizes, more than 18 atoms, as it was reported experimentally and theoretically calculated [75, 76, 77, 78]. The stability spectrum of Mg clusters cannot be explained only by a simple jellium model considering spherical

---

This work was done in collaboration with G. van Dorp, Universiteit Leiden, D. F. Urban, Albert-Ludwigs-Universität, Germany, J. Bürki and C. A. Stafford, University of Arizona, Tucson.

clusters, but it was proposed that additional stable clusters with a spheroidal shape occur [78]. It is found that, although the stability of clusters is given by their electronic properties, they do not determine the structure completely. Additionally a contribution comes from the geometrical packing that is influenced by the hexagonally closed packed structure of bulk magnesium [78].

Conductance histograms for aluminum atomic size contacts recorded using the MCBJ technique at 4.2K were reported by Yanson *et al.* [79]. Four peaks can be identified situated close to 1, 2, 3 and 4 conductance quanta. Scheer *et al.* [80] analyzed the transmission modes for Al point contacts by recording current-voltage characteristics in the superconducting state. For a single atom three modes are found to contribute to the conductance, having transmissions lower than one, summing together to a total conductance of one quantum unit. Previous results on aluminum shell structure were already reported by Medina *et al.* [43]. The authors report both experimental results and molecular dynamics simulations of the evolution of Au and Al nanowires when breaking. The experiments are performed using a STM at room temperature in UHV. The authors attribute the oscillation period of the peaks to filling of octagonal facets, claiming that the electronic shell effect is absent. Our results reported below are significantly different since we present evidence of electronic shell effects. The large series of peaks in Ref.[43] may not have enough weight to be reproducible.

In the next sections we will report conductance histograms recorded for Al and Mg nanowires in UHV at room temperature. For every metal we have investigated six samples using the MCBJ set-up described in chapter 3. A long series of peaks was obtained from the beginning of the measurement for every sample and the peak structure is characteristic for the given metal.

## 6.2 Aluminum

### 6.2.1 Experimental results

A conductance histogram for aluminum is shown in Fig. 6.1. We can see a remarkably long series of peaks, in this case up to  $100 G_0$ . The first step in finding out the origin of the peaks in a conductance histogram is to verify whether the peaks are periodic in conductance or in contact radius. We can see in Fig. 6.1 c) that a linear dependence is found with the radius, while for the conductance the dependence is far from linear, b). Therefore we can conclude that similar to the noble metals the peaks in the histograms are related to stable radii of the nanowire. In the case of the histogram of Fig. 6.1 the period found is  $\Delta k_F R = 0.58 \pm 0.01$ . As for the noble metals the appearance of the histograms varies from one experiment to the next and a characteristically different histogram can be seen in Fig. 6.2. Here a cross-over to a different period occurs. Two periods of oscillation can be identified around  $\Delta k_F R = 1$  and  $0.5$  having a crossover at a conductance value of about  $40 G_0$ . The first period is similar to the period obtained for noble metals for electronic shell effect. The second one, similar to the period of the histogram from Fig. 6.1, is somewhat

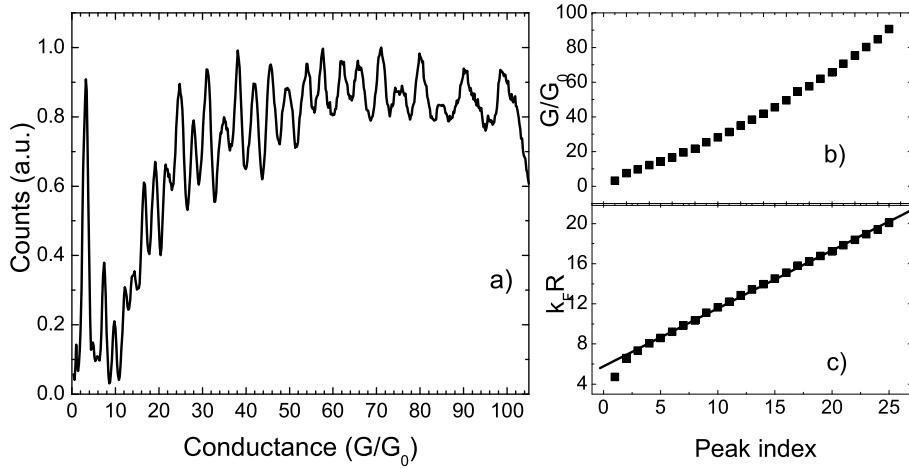


Figure 6.1: Conductance histogram for aluminum at RT-UHV showing a remarkably long series of peaks. The peak position vs. their index is plotted in b) (the conductance values at the peak positions) and c) (the peak positions converted to  $k_F R$ ). For c) a good linear dependence is obtained with a period  $\Delta k_F R = 0.58 \pm 0.01$ .

larger than what was obtained for the atomic shell effect in noble metals, for which typically  $\Delta k_F R$  is found around 0.42. Different than for noble metals, the cross-over between the two periods appears at higher conductance values, in this case around  $40 G_0$ .

Sometimes a new type of histogram appears having only two peaks as one can see in Fig. 6.2 b). This type of histograms appears at the beginning of the measurements on a fresh sample just after the initial breaking, and we see it in 7 out of 30 histograms. The position of the peaks is always close to 14 and 22  $G_0$ . In two of the histograms also a peak at 5  $G_0$  appears. One can see in the breaking traces very long plateaus at these values.

In Fig. 6.3 we show a conductance histogram recorded for aluminum in air at room temperature. We see distinct peaks that have a period close to the electronic shell effect found in noble metals and for Al in UHV. It is known that Al is a very reactive metal that forms an oxide layer on the surface, therefore the presence of peaks is unexpected. A possible explanation can be that the surface oxide layer does not immediately penetrate in the bulk of the wire and since we deform only a small fraction inside the wire, this remains uncontaminated for some time.

## 6.2.2 Discussion

Remarkably for Al the peaks extend up to high conductance values. Aluminum has a lower melting temperature than the noble metals, having then a higher

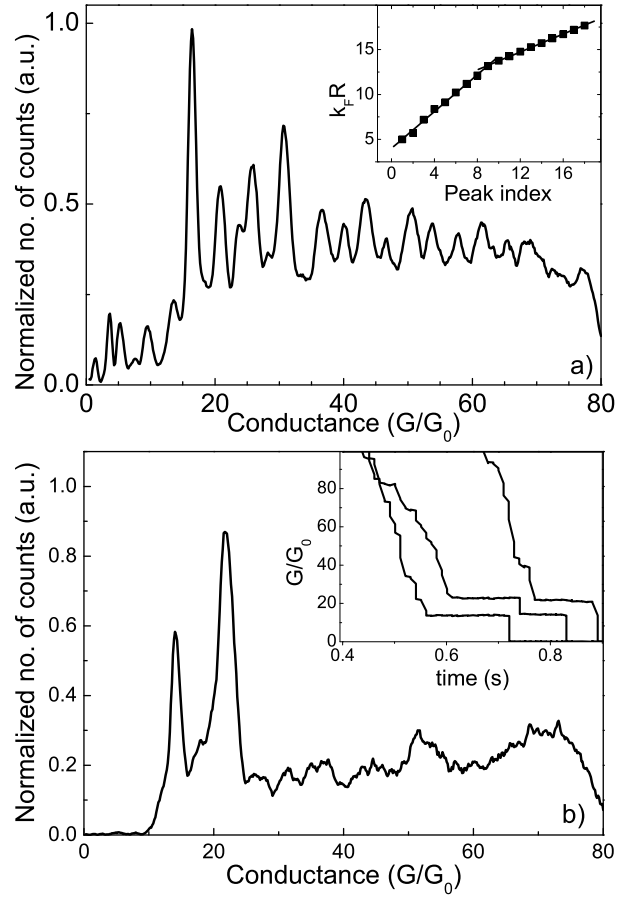


Figure 6.2: a) Conductance histogram for Al taken under UHV-RT conditions. Inset: the peak oscillation has two periods: in the low conductance regime up to about  $40 G_0$  the period is  $\Delta k_F R = 1 \pm 0.08$  and for the higher diameters  $\Delta k_F R = 0.5 \pm 0.06$ . b) Special type of histogram recorded for Al at RT-UHV showing two dominant peaks situated at  $14$  and  $22 G_0$ . Sometimes in the individual conductance traces a long plateau can be seen at these values, shown in the inset.

atomic mobility at room temperature. The melting temperature decreases when the size of the system goes down [54]. Possibly larger diameters are more difficult to stabilize for noble metal nanowires than for Al nanowires at room temperature.

The stability of Al nanowires was studied using a jellium model considering a soft confining potential [20]. The free energy is calculated using a jellium model within local density approximation (LDA) and it is found to have oscillations

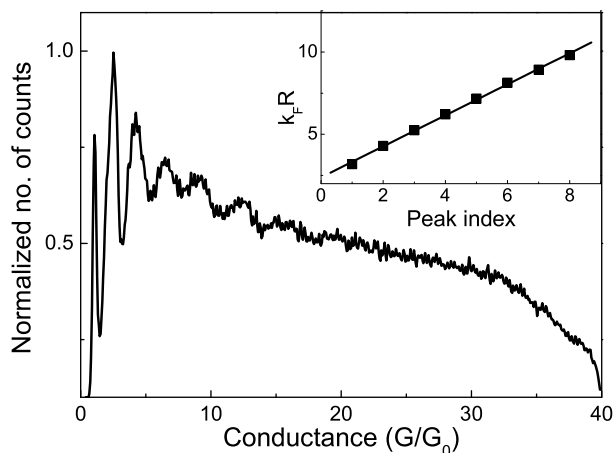


Figure 6.3: Conductance histogram for Al at room temperature in air. Inset: the peak oscillation has a period  $\Delta k_F R = 0.94$ .

as a function of the wire radius, with minima corresponding to stable configurations. We convert the predicted magic radii of the wires to conductance using the improved Sharvin formula (Eq. (4.1)) [61], [30].

We can see in Fig. 6.4 that most of the peaks are close to the theoretically calculated stable diameters. However, two of the peaks at 14 and 22  $G_0$  are completely out of the predicted values, as indicated by arrows. This is an indication that these particular diameters are not regular cylindrical wires. Moreover an evidence that these peaks represent different structures comes from the fact that they occur isolated in the histograms, being exceptionally stable, as shown in the histogram of Fig. 6.2 b).

The amplitude variation of the peaks that we see in the histograms can be a result of the beating pattern due to a superposition of several orbits having different frequencies. The strongest contributions are expected to come from the diametric, triangular and square orbits, similar to Na and to the noble metals. The beats positions from the LDA jellium calculation of [20] are plotted in Fig. 6.4. We can identify in the experimental histogram a lower amplitude for the two peaks next to 25  $G_0$ , where a beat minimum is expected. The beat minimum near 8  $G_0$  appears to be shifted to about 10  $G_0$  in the experiment. Above 40  $G_0$  the structure in the histogram is not reliable enough for identifying the third beat.

In Fig. 6.4 we also compare the experimental histogram with the results predicted by a purely free electron model [81] that includes also quadrupolar deformed cross-sections for Al nanowires. The peak positions can be well reproduced by including both cylindrical and deformed nanowires. In particular the peaks at 14 and 22  $G_0$  would be attributed to deformed nanowires. However their exceptional stability, causing them to appear isolated in a histogram



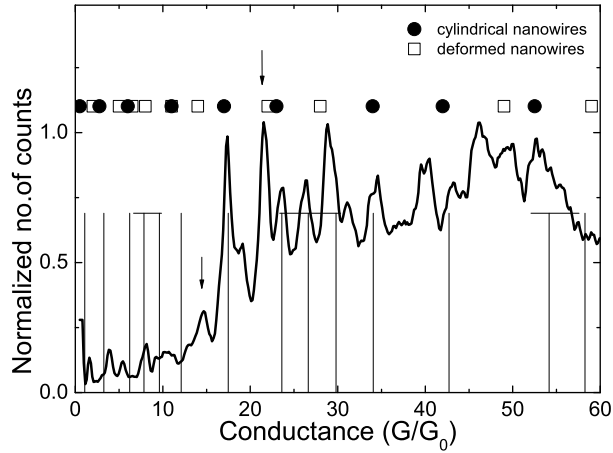


Figure 6.4: Comparison with the theoretical predictions for the electronic shell effect stable diameters. The vertical lines are the calculated energy minima using a jellium LDA calculation of Ref.[20]. The horizontal lines indicate the position of the supershell beat minima. Results of purely free electron model [81] are included. The predicted stable diameters for cylindrical and deformed wires are represented by circles and squares.

would not be completely expected for these deformed wires, since in a stability diagram they do not appear exceptionally stable compared to other deformed wires and less stable than the cylindrical ones. Exactly which structure they represent remains to be investigated further.

Given the good agreement with the stable diameters predicted by the theory [20], [81] and with the electronic shell effect period seen in noble and alkali metals we suggest that the periodic pattern having the period of  $\Delta k_F R$  around 1 is due to the electronic shell effect.

Similar to aluminum clusters we observe a cross-over to a different period of about  $\Delta k_F R = 0.55$ . This cross-over varies between different histograms, similar to noble metal nanowires. In the case of clusters the cross-over was determined to be at 75 atoms, which would mean a radius of around  $k_F R = 12$ . Although the surface reconstruction is expected to be different for spherical clusters compared to nanowires, we often get a similar value for the cross-over to the new type of period, as presented in Fig. 6.2 ( $k_F R = 12$  would correspond to a conductance of about  $36 G_0$ ).

Similar to noble metals, Al bulk has a fcc packing. We will use the same packing model as for noble metals, described in chapter 2. For Al the period will be different when expressed in  $k_F R$ , due to a change in the Fermi wave vector, that depends on the number of valence electrons as [82]:

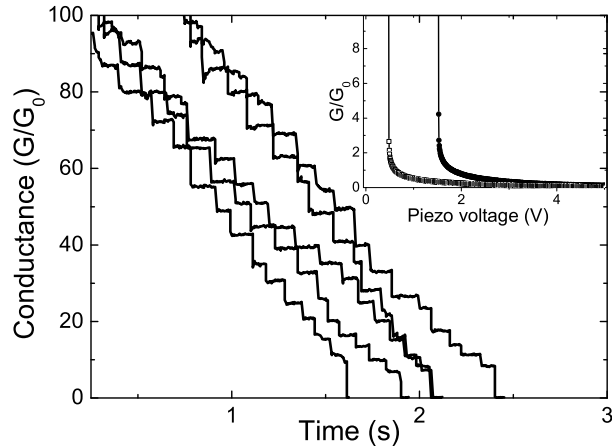


Figure 6.5: Individual conductance traces for Mg at room temperature in UHV. In the inset two curves for the low conductance regime are shown, plotted as a function of the piezo voltage which is proportional with the contact elongation.

$$k_F = \frac{2\pi}{a} \left( \frac{3x}{2\pi} \right)^{1/3} \quad (6.1)$$

where  $x$  is the valence of the metal and  $a$  is the lattice constant. We will expect to obtain for aluminum  $\Delta k_F R = 0.66$ . Averaging over 7 histograms we obtain a value  $\Delta k_F R = 0.54$ , that is 15 % lower. Deviations of this order were also observed for noble metals. The decrease in the period can be attributed to conductance lowering due to backscattering on surface roughness.

## 6.3 Magnesium

### 6.3.1 Results

In Fig. 6.5 we show some individual conductance traces for Mg at room temperature in UHV. One can see a nice sequence of steps with plateaus mostly at the same conductance values. This effect is specific for magnesium, while in the other metals the structure of the steps was less regular. Also specific to magnesium is the fact that the contact breaks suddenly in the low conductance regime, the last step occurring at conductance values higher than  $5 G_0$ .

When adding the traces in a histogram a nice series of peaks results (Fig. 6.6). The peaks are much sharper and better defined than for the other metals presented. The histogram shows no counts below 4 or  $5 G_0$  as expected from the sudden breaking seen in the traces in Fig. 6.5. This is valid for all the histograms we have recorded, and is very different from Al and the noble metals

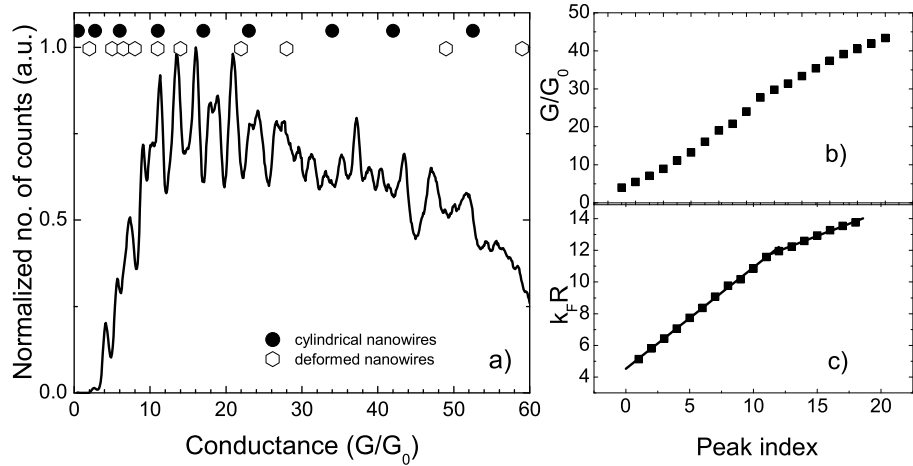


Figure 6.6: A conductance histogram for Mg recorded at RT-UHV. In the right panels we plot the peak positions vs. their index in conductance units (b) and in  $k_F R$  (c). One obtains a linear dependence for the latter with two periods of oscillations as  $\Delta k_F R = 0.64 \pm 0.07$  and  $\Delta k_F R = 0.31 \pm 0.04$ . The predicted stable diameters due to electronic shell structure of a free electron model are shown in (a) by dots for cylindrical and deformed nanowires [81].

where peaks close to 1, 2 and 3  $G_0$  are present. In the low conductance regime we see a sudden jump from about 10  $G_0$  to an exponential decrease of the current below 1  $G_0$  (Fig. 6.5 bottom).

The next question is to identify the peak origin in the histograms. Similar to the other metals we verify whether the peaks are periodic with the radius of the wire. In Fig. 6.6 c) a linear dependence is obtained with the radius of the nanowire, giving two periods around  $\Delta k_F R = 0.64$  and  $\Delta k_F R = 0.31$ . When plotting the peaks position in conductance values the dependence is clearly not linear (Fig. 6.6 b)).

In some of the histograms the peaks have a different period, as for example in the histogram from Fig. 6.7, where a cross-over between two periods  $\Delta k_F R = 0.87$  and  $\Delta k_F R = 0.38$  occurs. One can see that in this case both series have less peaks, especially for the second one the peaks are not so clear, as in the previous histograms. Sometimes we have observed a special type of histogram shown in Fig. 6.8. In the intermediate region the peaks have almost a double oscillation frequency, like a superposition of the oscillations from regions 1 and 2. Starting from the seventh peak we have divided the peaks between the two oscillations. We have attributed the odd indexed peaks to the first region and the even ones to the second. In this way we obtain a dependence that is not exactly linear (see Fig. 6.8 c). When plotting the peaks positions in conductance values (see Fig. 6.8 c) we obtain a very nice linear dependence where the two period are

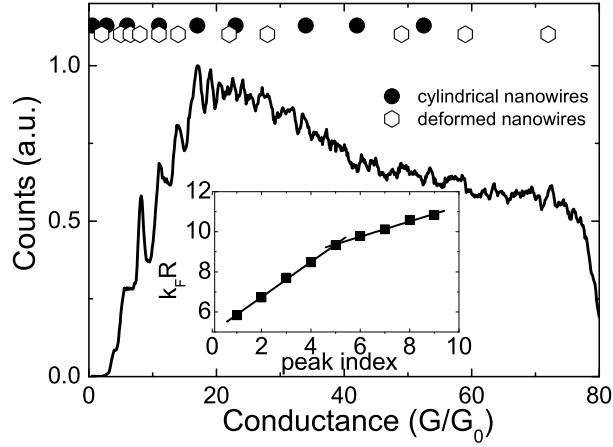


Figure 6.7: Conductance histogram for Mg recorded at RT-UHV. Inset: peak positions vs. their index in  $k_F R$ . One obtains a linear dependence with two slopes:  $\Delta k_F R = 0.87 \pm 0.06$  and  $\Delta k_F R = 0.38 \pm 0.06$ . The predicted stable diameters due to electronic shell structure of a free electron model are shown by dots for cylindrical and deformed nanowires [81].

close to each other being around  $\Delta g = 2$ , where  $g = G/G_0$ . This type of stability that is proportional with the conductance is definitely different from what we see in Fig. 6.6 and in most of our histograms.

### 6.3.2 Discussion

Mg histograms present three types of periods of oscillation. The most dominant one appearing in 12 out of 16 histograms is in average found at  $\Delta k_F R = 0.55$ . This is about two times lower than what is expected for electronic shell effect when considering free electrons confined in a cylindrical cavity. The expected period for atomic shell filling would be  $\Delta k_F R = 0.43$ , using a similar packing model as described in chapter 2 but starting from the hexagonally closed packed bulk lattice of Mg. Also if considering atomic shell packing starting from a different bulk lattice structure like fcc or bcc, the expected period will be very close to  $\Delta k_F R = 0.43$ . One can expect a lowering of the slope due to conductance lowering due to backscattering, but a higher period is unexpected.

As we already mentioned, Mg clusters present regular magic numbers related to spherical clusters, that are predicted with the jellium model [78]. Besides, intermediate stable clusters occur that are spheroidal. Inspired by these findings in clusters, as well as by the theoretical predictions of Jahn-Teller distortions in nanowires [22], one possibility is that some of the stable diameters are related to deformed nanowires. The increased number of stable diameters will decrease the periodicity. In Fig. 6.6 we compare the predicted values of the purely free

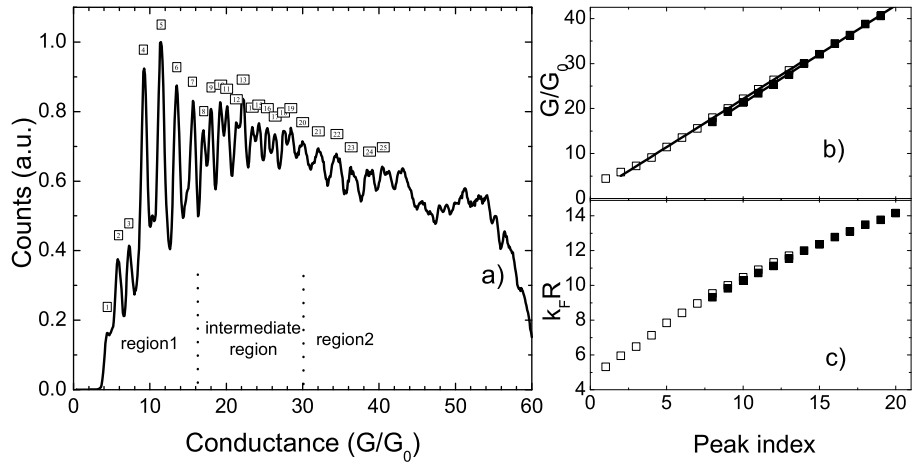


Figure 6.8: Conductance histogram for Mg. In the intermediate region the histogram has a superposition of the peaks with the periods from the region 1 and 2. In the inset we plot the peak positions vs. their index. For the intermediate region we attribute alternately the odd peaks to the first period and the even ones to the second one. In b) we plot the peak positions in conductance values. We can see two precise linear dependencies having very similar slopes:  $\Delta g = 2.15 \pm 0.1$  and  $\Delta g = 2.10 \pm 0.15$ .

electron model for cylindrical and quadrupolar nanowires with the our experimental histogram. We use the values calculated for Al since they should be largely the same, only their relative stability can differ, as suggested in [22], [66]. Some of the peak positions can be reproduced, but the agreement is not perfect. Therefore it is likely that an additional effect plays a role here, and a possibility will be a superposition between electronic and atomic shell effect. Possibly a mixed structure is formed, that at the same time accommodates both atomic closed-packing and electronic free energy minima. A similar interplay was found for Mg clusters where the atomic structure is found to have a significant contribution even for small clusters [78]. A molecular dynamics simulation predicts the occurrence of helical multishell nanowires for Mg [83]. Since the conductance of these structures is not calculated we cannot directly compare them with our experimental data. Although this would be another possibility to interpret the period around  $\Delta k_F R = 0.55$ , by analogy with gold nanowires we think it is less probable.

A better agreement with the theoretical results is found for the histogram from Fig. 6.7. In this case up to a conductance of about  $17 G_0$  for every peak there is a direct correspondence with a predicted stable diameter, either cylindrical or deformed. This is not unexpected since the period of the first peaks is close to the electronic shell effect period.

## Conclusions

In both histograms (Fig. 6.6 and Fig. 6.7) a cross-over to a lower period is found, that has the value in average around  $\Delta k_F R=0.35$ . This is similar to the atomic shell effect period found in noble metals. For Mg atomic shell packing we expect a value of  $\Delta k_F R=0.43$ . The experimental value is, as in the case of aluminum and noble metals, 15% lower. In analogy we suggest that the peaks having this period are related to the atomic shell effect.

An exception from the periodicity in radius is found in Fig. 6.8 where the peaks are periodic in conductance. An interference between two type of oscillations belonging to the two regions is seen in the intermediate region. This looks like an even-odd oscillation of the peaks since the period is around  $\Delta g=2$ . The origin of this exceptional periodicity remains to be further investigated.

The conductance traces for magnesium always break at fairly large values, as it can be seen in the traces of Fig. 6.5. This effect is specific for Mg and very reproducible. Similar to clusters, we suggest that it represents the transition from the metallic to nonmetallic state when the nanowire radius decreases. Different than for clusters, in the case of the nanowires the electronic states are continuous along the nanowire axis, being confined only in the transverse directions. Instead of electronic levels present in the clusters, the nanowire will have the electronic states grouped in sub-bands. For low diameters most of the atoms are on the surface having a low coordination number. The sub-band width is proportional with the number of nearest neighbors, decreasing with the number of atoms in the cross-section. It is possible that similar to clusters a gap will occur between  $s$  and  $p$  bands, and due to the filling of the  $s$  band the nanowire will become insulator. At this transition in clusters not only the electronic properties change but also their binding energy. It is predicted that the metallic bond changes into a van der Waals bond, that is much weaker [78]. This can be the reason that the wire breaks suddenly when it becomes an insulator. If the wire would be still mechanically contacted, instead of the exponential dependence one would expect to see jumps in the low conductance regime when the contact is pulled apart.

## 6.4 Conclusions

In this chapter we have reported measurements performed on multivalent metals at room temperature in UHV. In the case of aluminum the similarity with noble metals is quite obvious. Therefore we suggest that we obtain stable diameters that are related to electronic and atomic shell effects. The electronic shell effect stable diameters calculated using a free electron model agree well with the positions of the peaks in our histograms. Additional stable diameters are found, that sometimes appear isolated in the conductance histogram. It has been suggested that stable wires that are highly deformed would correspond to these conductance values. However it seems unlikely that they would appear even more stable than the circular wires. A satisfactory explanation for these exceptional peaks has not yet been found. Remarkably some of the peaks survive under ambient conditions.

In the case of magnesium we obtain three types of histograms having three periods of oscillation. The lowest period that is found at high conductances can be attributed to atomic shell packing. The highest one is close to what is expected for electronic shell structure in cylindrical nanowires, although somewhat lower. For this type of histograms we get a good agreement with theoretically predicted stable diameters, and the somewhat lower period can be attributed to electronic shell effect when considering also deformed nanowires. An intermediate period can be found in most of the histograms. In analogy to Mg clusters this period can be explained by an interplay between electronic and atomic shell effect. Also similar to clusters we have indications that at low diameters, typically below  $4 G_0$ , the nanowire becomes an insulator, together with a weakening of the metallic bond.

# VII

## Mechanical properties of metallic nanowires

### 7.1 Introduction

In the characterization of atomic contacts the information comes mostly from electrical measurements, like conductance histograms,  $I - V$  spectroscopy, shot noise (for a review see [84]). However we have little information about their mechanical properties. We are particularly interested in metallic contacts and their electrical and mechanical properties are interconnected [85], [25]. Therefore simultaneous measurements of the conductance and force would bring extra information about the physics of these systems. An example of such an experiment was reported by Rubio *et al.* [29]. In this experiment the set-up is a combination of an scanning tunnelling microscopy (STM) with atomic force microscopy (AFM). An atomic contact is formed between a STM gold tip and a gold surface, and its conductance can be monitored. Simultaneously, with the AFM one can measure the forces acting in the contact. The authors have investigated in this way the evolution of the force for thick contacts consisting of hundreds of atoms [86] and also atomic sized junctions down to one atom in cross-section including the formation of monoatomic chains [2, 87].

In order to be able to measure the force in the atomic contacts by not influencing their formation and evolution, the cantilever stiffness should be much larger than the stiffness of the contact itself. This reduces the detection sensitivity. In order to overcome this problem we have developed a new force sensor that will be described in the next sections. This is a combination of the MCBJ set-up with a tuning fork used as force sensor. Besides the large stiffness of the tuning fork, of the order of 10 kN/m, another advantage is its sensitivity due to a high quality factor (of the order of few thousands) that allows detection of very small frequency shifts (smaller than 100 mHz) and at small vibration amplitudes (smaller than 10 pm). Moreover the tuning fork is made of quartz, that is a piezoelectric material. The oscillation signal will produce a voltage that will be detected. The electrical detection replaces the complication of optical detection of the cantilever motion commonly used in the AFM techniques.

---

This work was done in collaboration with T. Shiota, Tokyo Institute of Technology, Japan and A. Valkering, T. Oosterkamp from Universiteit Leiden



Another advantage of this technique comes from the possibility of adapting the tuning fork use to the MCBJ set-up. This allows us to make use of the high mechanical stability of the MCBJ in comparison with the STM fabrication of atomic contacts. Lastly, with the tuning fork we will measure directly the stiffness of the contact, that gives direct information of the strength of the atomic bonds. Instead, in the AFM-STM measurement the force is measured, that is stiffness multiplied with the elongation.

A similar design making use of the MCBJ and a tuning fork was independently developed by Rubio *et al* [88]. In this way the authors have investigated the stiffness simultaneously with the conductance in the tunnelling regime, in order to study the metallic cohesion.

The purpose of our work is to understand the mechanical properties of metallic nanowires, with diameters ranging from hundreds of atoms to just one atom in cross-section. As explained in chapter 4 we obtained evidence that for thicker gold nanowires shell structure enhances the formation of certain "magical" diameters. We expect that the exceptional stability of these diameters should be reflected in their stiffness. Also related to the stability we investigate the stiffness of very thin nanowires, in particular the formation and stability of monoatomic chains.

## 7.2 Experimental methods

### 7.2.1 Device design

In Fig.7.1 is shown a schematic drawing of the sample configuration. It represents a combination of the standard MCBJ technique with the use of a tuning fork as a force sensor. We use commercially available tuning forks that originally have a metallic casing sealing the two prongs. We remove partially the capsule keeping only a little ring around the prongs at their base. This base is soldered on the bending beam with both prongs freely standing, as seen in Fig.7.1. A notched 100  $\mu\text{m}$  wire is attached to the tuning fork, gluing one electrode on one prong and the other one on a metallic support placed at the same height as the tuning fork prongs. The sample is mounted in an insert in a three point bending configuration. The insert is pumped down to pressures of  $10^{-5}$  mbar and then cooled down to liquid helium temperature. The wire is broken for the first time in cryogenic vacuum, ensuring in this way freshly exposed surfaces.

### 7.2.2 Oscillator model of a tuning fork

The tuning fork is a coupled mechanical resonator formed by two prongs that oscillate with a frequency dependent amplitude. For one of the oscillating modes that we are interested in, the prongs oscillate in opposition on a direction parallel to the substrate ( $x$  axis), with a maximum amplitude at the resonance frequency that is for the bare tuning fork at exactly 32768 Hz. We will derive the oscillation motion for one prong, considering it as a spring with elastic constant  $k$ . The

## Experimental methods

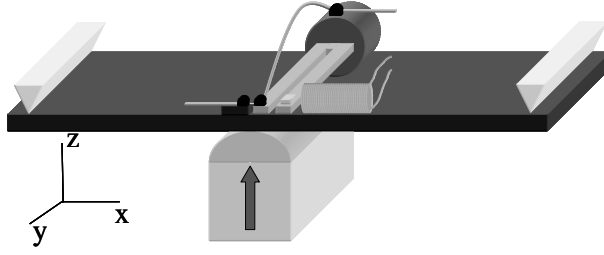


Figure 7.1: Schematic drawing of the MCBJ combined with the tuning fork (TF). One end of the wire is placed on the TF prong and the other one on a metallic support, having the notch suspended in between. The substrate is bend from below by the piezo element causing the wire to break at the notch. A coil is placed on the bendable substrate close to the second prong of the TF where the magnet is glued. The coil and the magnet are used for the mechanical excitation of the TF, that will oscillate along  $x$  direction.

equation of motion along  $x$  is:

$$m\ddot{x} + m\gamma\dot{x} + kx = F\exp(i\omega t) \quad (7.1)$$

This is the equation of motion for a forced harmonic oscillator with damping. Here  $m$ ,  $k$ ,  $\omega = 2\pi/f$  are the mass, force constant and driving frequency of the tuning fork. The second term in the Eq. 7.1 is responsible for the losses occurring in the prongs, being proportional with the velocity.  $\gamma$  is inverse proportional to the tuning fork quality factor ( $Q$ ) and  $F$  is the external driving force. Assuming a solution of the type  $x = x_0\exp(i\omega t)$  and writing  $\omega_0 = \sqrt{k/m}$ , one obtains the expression for the absolute value of  $x_0$  as:

$$x_0 = \frac{F}{m} \frac{1}{\sqrt{(\omega_0^2 - \omega^2)^2 + \gamma^2\omega^2}} \quad (7.2)$$

This is a Lorentzian dependence of the tuning fork oscillation amplitude on the driving frequency, having a maximum at the resonance frequency,  $\omega_0$ . The quality factor,  $Q$ , of the tuning fork is defined as:

$$Q = \frac{f_0}{\Delta f_{FWHM}} \quad (7.3)$$

where  $\Delta f_{FWHM}$  is the full width at half maximum on the Lorentzian curve.

### 7.2.3 Calibration of the stiffness of the contact

In order to measure the elastic constant of the atomic contact, we are measuring the shift in the resonant frequency due to the stretching force acting in the contact. In order to translate the frequency shift into elastic constant we use an

approximation of the harmonic oscillator model. In the presence of the external force, the equation of motion 7.1 changes as:

$$m\ddot{x} + m\gamma\dot{x} + kx + F_c = F \exp(i\omega t) \quad (7.4)$$

where  $F_c$  is the force acting on the atomic contact during stretching. Considering very small oscillation amplitudes, one can linearize the force  $F_c$  around the equilibrium position of the tuning fork  $x_0$  as:

$$F_c(x_0 + \Delta x) = F_c(x_0) + \Delta k(x_0)\Delta x + O_2(x) \quad (7.5)$$

In this equation  $\Delta k = \partial F_c / \partial x$  is the stiffness of the atomic contact to be determined and  $O_2$  contains the higher order terms in the expansion, that we will neglect. The linearization is valid for oscillation amplitudes  $x$  much smaller compare to the displacements induced by stretching in the contact. Replacing this in the eq. (7.4) and with  $x = x_0 + \Delta x$  one will obtain:

$$m\ddot{x} + m\gamma\dot{x} + (k - \Delta k)x \simeq F \exp(i\omega t) - F_c(x_0) - k_c(x_0) \quad (7.6)$$

At the resonance:

$$\omega = \sqrt{\frac{k + \Delta k}{m}} \quad (7.7)$$

Considering  $\Delta k \ll k$  and performing a Taylor expansion, one obtains the relation between the frequency shift and the stiffness of the contact:

$$\frac{\Delta\omega}{\omega_0} = \frac{1}{2} \frac{\Delta k}{k} \quad (7.8)$$

#### 7.2.4 Driving the tuning fork

The tuning fork (TF) can be either mechanically driven or directly electrically excited. We have used both methods. In the first case the mechanical driving is done by the magnetic interaction between a piece of magnetic material placed on one of the tuning fork prongs and one coil placed at very close distance to the tuning fork free prong, as illustrated in Fig.7.1. The coil has an iron core, in order to increase the strength of the magnetic field. Typical dimensions for the coil are length 8 mm and diameter 2.5 mm and it has an electrical resistance  $R_{coil} = 2\Omega$ . By applying an ac voltage on the coil, typically with an amplitude of 10 mV, a magnetic field will be induced that will put the magnet in oscillatory motion and subsequently the TF prong. The piezoelectric effect of the quartz arms of the TF will induce an ac voltage.

The other method to drive the TF is by directly applying an ac voltage on it's contact pads. By reverse piezoelectric effect this will produce a time dependent oscillation motion that further will induce a time varying charge and therefore an ac current. In both cases mentioned above we monitor the induced current on the TF.

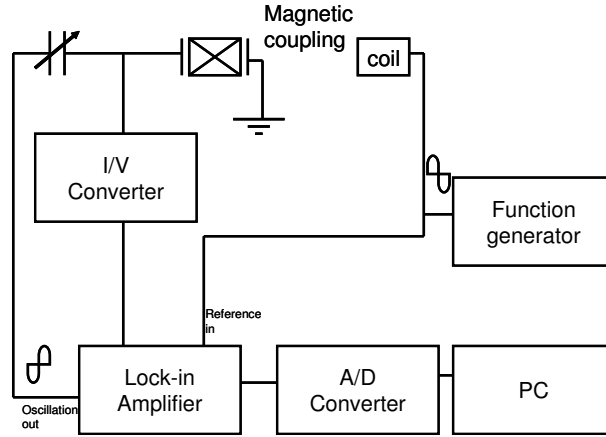


Figure 7.2: Electronic circuit used for TF mechanical excitation, capacitive current compensation and TF signal detection.

Besides the piezoelectric current ( $I$ ), the measured current has an additional component ( $I_c$ ) given by a stray capacitance determined by the intrinsic properties of the tuning fork, such as geometry of the contact pads, but also by the measurement cable capacitances. The shape of the resonance curve can be modelled by considering an equivalent electrical RLC circuit in parallel with a capacitance. The resonance curve will be asymmetric due to the frequency dependence of  $I_c$ . In order to have a unique relation between the phase and the frequency we need to have a symmetric resonance. Therefore one needs to compensate for the capacitive current  $I_c$ . We show in Fig. 7.2 the scheme for measurement and compensation in the case of mechanical driving of the TF. An ac voltage is applied to the coil from the function generator. The same signal is used as a reference for the lock-in amplifier. The output voltage from the lock-in amplifier will be inverted and applied to a variable capacitor. One can compensate  $I_c$  by adjusting the amplitude of the voltage of the output of the lock-in amplifier or the variable capacitance. A similar type of compensation is done in the case of electrical driving of the tuning fork. An ac voltage from the function generator is in this case directly applied to the tuning fork. The ac voltage is inverted and applied to a variable capacitor, in order to compensate  $I_c$ . In this case the capacitive current is larger than for mechanical driving, the compensation being much more important.

### 7.2.5 Detecting the tuning fork signal and its calibration

Once the signal is compensated it is amplified by the current to voltage ( $I/V$ ) converter and then read by the lock-in amplifier. The signal is recorded using a digital to analog converter card of 16 bits resolution. The final purpose is to measure the resonance frequency of the TF as a function of the applied force in

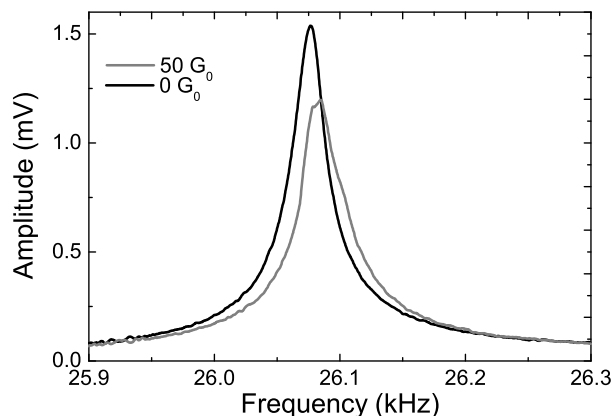


Figure 7.3: Two tuning fork resonances at RT-HV for a gold sample, in the case of a contact of about  $50G_0$  and in broken contact. The frequency shift is about 7 Hz and the quality factor of the tuning fork in broken contact is about 700.

the contact. A resonance can be measured by relating it either to the amplitude or to the phase of the signal. We have chosen the second option and used two measurement methods: with a phase-locked loop (PLL) system or directly measure the phase and use its linear region to relate it to the frequency shift. Both methods give similar results. Typical resonance curves of the tuning fork at room temperature under high vacuum (pressures of the order of  $10^{-5}$  Pa) are shown in Fig.7.3. Two curves are shown: for the case when the contact is broken (free tuning fork) and when we have a contact with a conductance of  $50 G_0$  that give roughly 50 atoms in the cross-section. A frequency shift of about 7 Hz is observed when the wire is connected.

The PLL detection was realized with the help of a homemade software done in LabView. From measurement of the phase shift the resonance frequency is calculated and send through a GPIB interface to the function generator as being the new driving frequency. The new phase shift is read again and the loop continues until the phase shift is close to 0 with a preset accuracy (usually 0.5 deg). The corresponding frequency at phase 0 is the resonance frequency, that will be recorded. This method is relatively slow. Therefore in many of the cases we have used directly the measurement of the phase shift while driving the TF at a constant frequency. One has to make the following considerations.

- i) The frequency range where the linear relation of phase with frequency applies goes down when the quality factor (Q) increases. For a very high Q the frequency shifts due to the force acting in the contact might go out of this linear region. In this case we cannot relate the values for the phase and the frequency.
- ii) The shape of the resonance should not change. This can be verified since simultaneously with the phase, we monitor the signal amplitude.

### 7.2.6 Calibration of the tuning fork oscillation amplitude

The tuning fork oscillation amplitude is a very important parameter, since it might influence the stability of the atomic contact. Besides, the relation between the contact stiffness and the shift in resonance frequency (Eq. 7.8) is obtained under the assumption of small oscillation amplitudes. In order to calibrate the amplitude we measure the tunnelling current between the two tips of the wire fixed on the TF. The tunnelling current will have an exponential dependence on the distance between the two tips:

$$I_t = CV \exp\left(-2d\sqrt{\frac{2m\phi}{\hbar^2}}\right) \quad (7.9)$$

Where  $V$  is the dc bias voltage applied across the contact,  $m$  is the electron mass,  $C$  is a constant that depends on the geometry of the two tips and the density of states at the Fermi level, and  $\phi$  is the work function of the material. Since one tip oscillates together with the tuning fork with the frequency  $\omega$ , the distance between the two tips oscillates also and the tunnelling current becomes:

$$I_t = CV \exp\left[-2(d_0 + A \sin\omega t)\sqrt{\frac{2m\phi}{\hbar^2}}\right] = I_{dc} \exp\left[-2A \sin\omega t \sqrt{\frac{2m\phi}{\hbar^2}}\right] \quad (7.10)$$

Where  $I_{dc}$  is the dc current when the two tips are at a fixed distance  $d_0$ , the equilibrium position of the TF. Since the oscillation amplitudes are very small,  $A \ll \hbar/2\sqrt{2m\phi}$ , we can approximate the current as:

$$I_t = I_{dc} \left[1 - 2A \sqrt{\frac{2m\phi}{\hbar^2}} \sin\omega t\right] \quad (7.11)$$

The current is amplified by the I-V converter and one has to take into account that its transfer function has a frequency dependence which becomes significant for high gains, as for example of  $10^7 V/A$  that we typically use for the tunnelling regime. The gain impedance  $Z_g$  for a gain resistance  $R_g$  and a parallel capacitance  $C_g$  is:

$$Z_g = \frac{R_g}{\sqrt{1 + (\omega R_g C_g)^2}} \quad (7.12)$$

With this correction we obtain the relation between the ac voltage due to the oscillation of the tuning fork and the dc tunnelling voltage:

$$\frac{V_t}{V_{dc}} = \frac{2A}{\hbar} \sqrt{\frac{2m\phi}{1 + (\omega R_g C_g)^2}} \quad (7.13)$$

The amplitude will be calibrated as follows: the tuning fork is driven at its resonance frequency. An dc voltage is sourced to the gold wire by the DAC card of the computer. The resulting tunnelling current is amplified by the  $I/V$  converter and the ac component is measured with the lock-in amplifier. At the

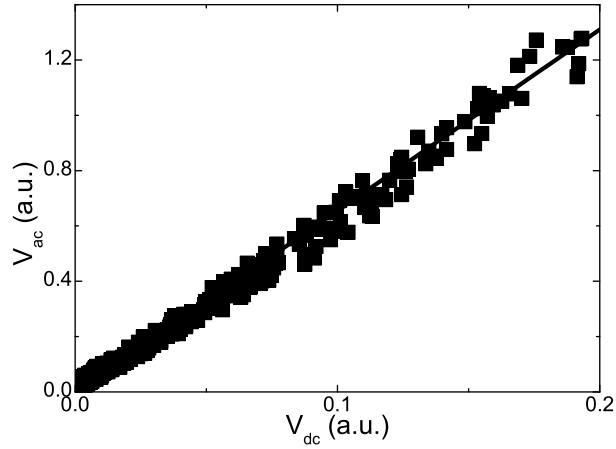


Figure 7.4: An example of calibration of the TF oscillation amplitude. The ac component for the tunnelling current due to the TF oscillation is plotted as a function of the dc component.

same time the dc and ac components are recorded on two different channels of the ADC card. Equation 7.9 can be used to calibrate the displacement of the electrodes with respect to the voltage applied to the piezo element used to bend the substrate. This method is very efficient, since by recording both ac and dc component we can calibrate at once the displacement ratio of the piezo and the oscillation amplitude of the TF.

An example of the TF amplitude calibration for a gold sample is shown in Fig.7.4. The tuning fork was driven electrically with an ac voltage of amplitude 0.1 mV at a frequency  $f=28112$  Hz. From the slope one can calculate the amplitude  $A$ , in this case being equal to 6.5 pm rms. We used the following values:  $R_g = 10M\Omega$ ,  $C_g = 14pF$ ,  $\phi = 5.5eV$ .

## 7.3 Experimental results

### 7.3.1 Platinum nanocontacts

In Fig. 7.5 one can see a typical trace for a platinum sample showing simultaneous recording of the conductance and the elastic constant in the process of breaking the wire. On the horizontal axis is plotted the piezo voltage as an linear measure of the electrodes displacement. The force constant ( $\Delta k$ ) is measured relative to the stiffness of the broken contact, that we take as  $k = 0$ . The conductance ( $G$ ) trace is formed by plateaus separated by sudden jumps, correlated to reconfigurations in the electrodes. The evolution of the contact during pulling was previously described as being composed of two stages [29]: an elastic stage where the conductance is constant (on a certain plateau) and a yield stage

### Experimental results

corresponding to the jump at a new configuration, with a smaller cross-section. One can observe a similar effect here, where the stiffness has abrupt jumps at the transition to a new plateau. We see that the stiffness shows a smooth decrease over the length of the plateau. This shows that the contact response over the elastic stage is not linear with the applied stress. The conductance plateaus similar to the stiffness, show a decrease as a function of elongation. It has been shown in a theoretical calculation that the slight increase or decrease in conductance over a plateau is related to the stretching of the orbitals for the given metal [89]. In this calculation is investigated conductance behavior over the last plateau, corresponding to an one atom contact, for the case of gold, aluminum and lead. The stretching causes a narrowing of the  $sp_z$ ,  $p_{xy}$  bands and depending on their position relative to the Fermi energy, this will affect the conductance. In the case of gold the conduction is given mostly by the  $sp_z$  orbital that is centered on the Fermi energy. By stretching, the narrowing of the  $sp_z$  resonance will not affect the conductance. By similarity with lead, we expect that in the case of platinum, the narrowing of the  $sp_z$  and  $p_{xy}$  will cause a decrease in the conductance. This is seen in the experiment not only for the last plateau but also for larger conductance values, as seen in Fig. 7.5. This way the smooth decrease of the stiffness over the conductance plateau upon pulling is not unexpected. The stiffness reflects the strength of the atomic bonds in the contact, and its decrease might mean that the bonds become weaker with increasing stress. Apart from the correlation in the change of  $G - \Delta k$ , as described above, one can also see that for very small changes in  $G$ ,  $\Delta k$  shows a significant variation, as for example at piezo voltage  $V_p = 13V$  in Fig. 7.5 where there is a sudden decrease in  $\Delta k$ , while a very small step in  $G$  is visible at that point. This might indicate a sudden change in the configuration of the contact, with a transition to a softer contact without a significant change in its cross-section size. When decreasing the contact radius, the maximum value of  $\Delta k$  on a certain plateau gradually goes down as one would expect when the stiffness is proportional to the contact size. However, the stiffness does not depend linear on the cross-section of the contact,  $S$ , as one would expect from the law for a macroscopic object:

$$k = \frac{ES}{l} \quad (7.14)$$

where  $E$  is Young's modulus and  $l$  is the object length. In Fig. 7.6 a) we plot the stiffness normalized to the conductance (that is proportional to the contact area) and we see an exponential increase of the  $\Delta k/G$  with decreasing the contact size. This was previously observed by Rubio *et al.* in the so called apparent pressure that is force divided by the contact area. For nanoscale contacts the volume to surface ratio is very small, and as a consequence the surface energy starts to play a role. One can make an estimation of the critical sizes where the surface effects has to be taken into account [84]. If we consider a cylinder of radius  $R$  that deforms plastically with a yield strength  $\sigma_y$ , the energy required to deform its volume will be:

$$E_v = \pi R^2 \sigma_y \Delta l \quad (7.15)$$



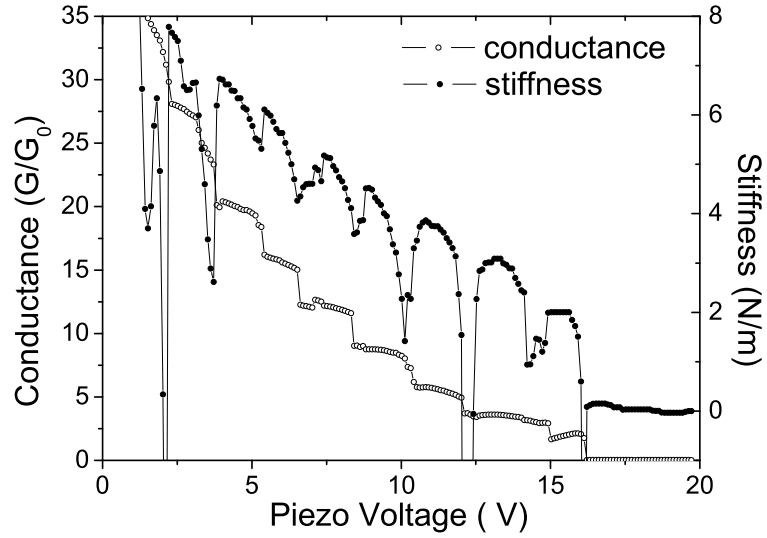


Figure 7.5: An example of simultaneous measurement of the stiffness and the conductance for platinum atomic contacts as a function of the piezo voltage. The conductance is measured by applying 10 mV bias voltage to the wire and monitoring the resulting current. The tuning fork is excited mechanically at constant frequency and the phase of the signal is monitored.

and the energy to deform its surface:

$$E_s = \gamma\pi R\Delta l \quad (7.16)$$

Using typical values for metals for  $\gamma$ , the surface energy and  $\sigma_y$  one finds that  $E_s$  becomes larger than  $E_v$  for radii  $R$  in the range 1-10 nm. The surface energy comes from unsaturated surface bonds. At equilibrium a system will minimize its surface energy by adopting the minimum surface. In the case of an atomic contact, this will be done by reducing its length and in consequence opposing to the external elongation, reflected in a high stiffness. Since we see that obviously the stiffness of the atomic contacts does not obey eq.7.14 we will check what dependence fits it best. Considering contact mechanics laws, the stiffness should have the dependence on the radius of the contact  $R$  as:

$$k = \frac{BER}{1 - \nu^2} \quad (7.17)$$

where  $B$  is a constant and  $\nu$  is Poisson's ratio [84]. In Fig. 7.6 b) we plot the stiffness divided by the square root of the conductance that is proportional to the radius of the contact. At a constant conductance  $\Delta k/\sqrt{g}$  shows oscillations that are just the jumps in stiffness at the steps in conductance. On average one can see a more or less constant dependence as a function of conductance that indicates that Eq. 7.17 is satisfied.

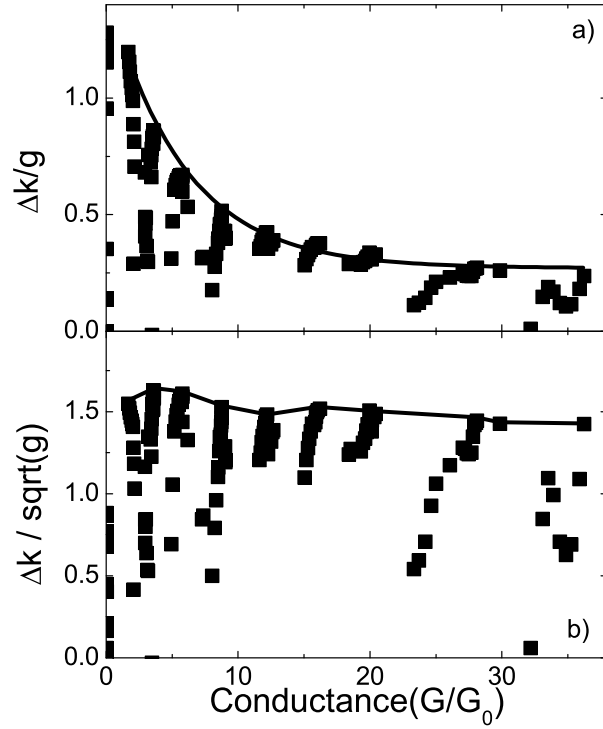


Figure 7.6: Stiffness for a individual trace for platinum normalized the conductance a) and to the square root of the conductance b).

In Fig. 7.7 we plot the stiffness as a function of the conductance for an individual trace for both processes, during the elongation and compression process. The stiffness values for the elongation process are higher than in the compression case for the elastic stages. This is a general behavior observed in many other traces. In the process of elongation it is more likely that long necks form while in the reverse process one expects to form shorter structures. If we would consider a macroscopic object that is elastically stressed, its elastic constant will depend on its length  $l$ , as given by Eq. 7.14. From this we would expect to have larger force constants for longer necks, contradictory to our results. It would make sense to get higher stiffness for longer contacts if we apply again the surface energy argument. When the neck is long, an extra contribution in the stiffness will come from the contact resistance to the elongation.

### 7.3.2 Stiffness of a Pt atomic chain

We will now concentrate on the last conductance plateau before breaking, see Fig. 7.8. This represents the formation of an one atom contact that in the

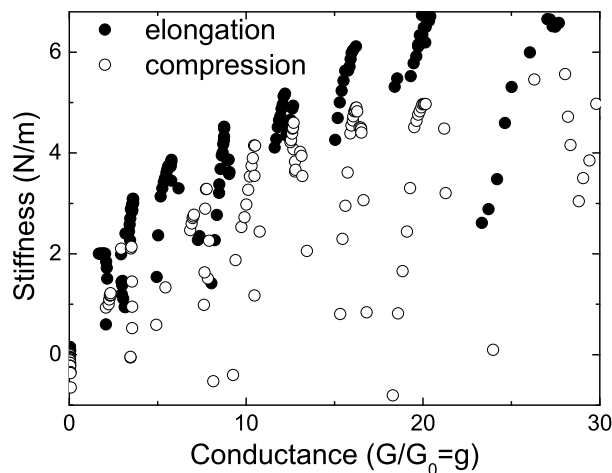


Figure 7.7: Plot of stiffness as a function of the conductance for an individual trace recorded during both the elongation and the contraction of the contact.

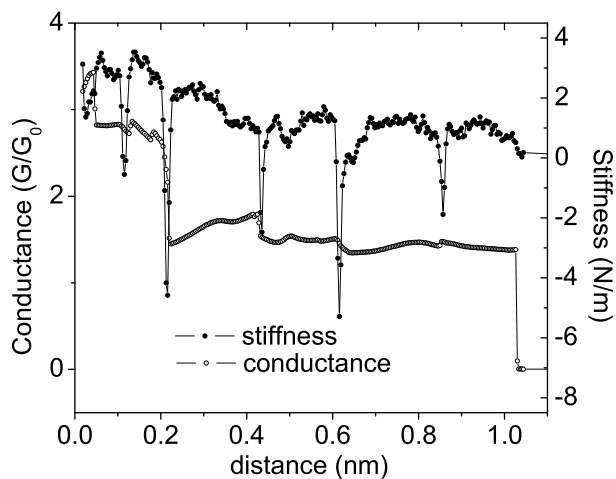


Figure 7.8: Measurement of the stiffness for the last conductance plateau for platinum.

case of platinum has a conductance between  $1.5-2 G_0$ . One can see in Fig. 7.8 that this last plateau can be stretched over a distance of about 0.8 nm. The conductance has some variations and a final decrease just before breaking to a value  $G=1.4 G_0$ , while at the starting point the conductance was  $G=1.5 G_0$ . Conductance is a measure of the number of atoms in the cross-section and since its value is more or less constant we have an indication that while pulling we

### Experimental results

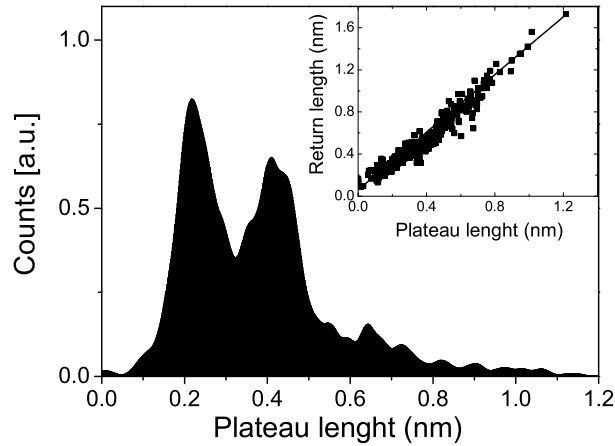


Figure 7.9: Histogram of the distribution of lengths for the last conductance plateau for platinum chains. Inset: Return distance vs. the length of the last plateau for platinum chains.

have just one atom in cross-section. From the length of the this plateau one can see that it represents approximately 4 atomic diameters. This constitutes an indication that a chain has formed in between the two electrodes, having just one atom in cross-section. The chain formation has been first reported by Yanson *et al.* [1]. The first argument used by Yanson *et al* comes from the length histogram. A length histogram counts the length of the last plateau, from the moment the conductance jumps to a preset value as being associated with the conductance of one atom, for Pt we take usually from  $G = 2.5G_0$  to the moment it breaks. Following this approach, we constructed a length histogram for Pt as seen in Fig. 7.9. Two distinct peaks are seen and their central position is equally spaced along the length axis. One can see that the occurrence rate decreases with the length, that means that longer chains are less favorable to occur. The periodicity of the length at the peaks position is an indication of the formation of an atomic chain. Additional evidence of the chain formation comes from the measurement of the return length, an experiment also firstly performed by Yanson *et al.* The return length is the length it takes once the chain is broken, to get back into contact. Since one needs to push back by distances comparable to the breaking distance, a linear dependence between the chain breaking length and the return length is expected. We have obtained this linear dependence on a Pt sample, as one can see in the inset of Fig. 7.9.

Most of the information on the chain formation comes from conductance measurement. With our new developed force sensor we can investigate the formation of the chains, having the advantage of being able to measure at the same time the conductance and the stiffness. In Fig. 7.8 we show an example of such measurement. Let us focus on the plateau that starts at about 0.2 nm. In

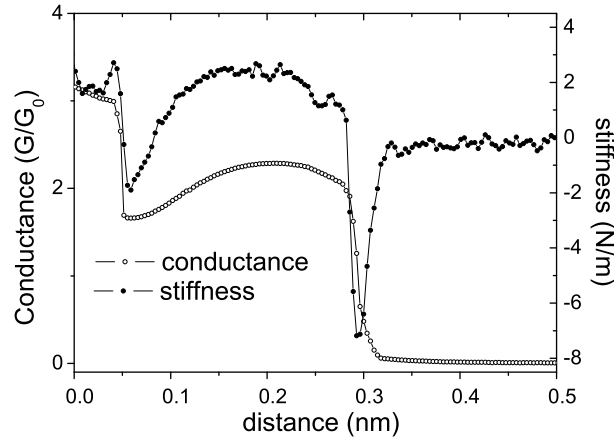


Figure 7.10: Measurement of the stiffness at the last conductance plateau for platinum.

the stiffness curve one can see sudden jumps that have a periodic occurrence. Their period is given in atomic diameters, and therefore we have an indication that they appear at the moment when a new atom is released from the electrodes into the chain. The jumps in the stiffness represents relaxations of the contact, when the build up strain during pulling is released at the reconfiguration when a new atom accommodates in the chain. One can see in the conductance curve some variations correlated to the jumps in the stiffness. The variation of the stiffness in between two jumps is not reproducible in detail, since it can come both from reconfigurations in the contact and in the electrodes.

One might find intriguing that the stiffness become negative at the jumps when a new atoms comes in the chain. The stiffness is the second derivative of the energy with respect to the length. The potential energy of the two states can be seen as formed of two wells that are brought close by pulling, and the barrier between them is decreased. At the inflection point of the two curves the stiffness (the curvature sign) becomes negative, leading naturally to a negative contribution to the stiffness.

### 7.3.3 One atom contact of Pt

We see in the trace from Fig. 7.5 that upon pulling the stiffness smoothly decreases. Over the last plateau the conductance shows in general a global decrease with the stretching, as discussed in the previous section. Under these considerations, the increase in  $G$  on the last plateau in the curve from Fig. 7.10 is unexpected. Note that this is observed for a short chain, expected to be two one-atom tips touching. We might relate it to a new configuration of the tips, recently predicted by first principle simulations [90]. The conclusion from the calculation is that platinum chains can form a zig-zag arrangement that is

### *Experimental results*

even more stable than a linear one. The conductance of such a zig-zag chain is predicted to be lower than for a linear one. Upon pulling the configuration might evolve into a linear one, together with an increase in the conductance. The authors describe two types of arrangements: first (for long chains) when the electrodes are collinear and only the atoms in the chain are zig-zag arranged and second when the banks are misaligned, in the case of two-atom chains. In the calculation the transition zig-zag to linear while pulling can occur only in the first case. In a real contact we can imagine a situation when the transition happens for the second case as well. While pulling, the banks deform elastically and can move sideways and this may lead to an alignment into a linear configuration.

We identify such a sign in the stiffness and conductance curve from Fig. 7.10. We see a smooth increase in the stiffness while pulling the two atom contact, that can be attributed to the transition between the two configurations, as one would expect that a zig-zag chain has a lower stiffness than a linear one. The conductance shows similar behavior as the stiffness, showing a smooth increase as suggested by the calculations [90]. After the chain becomes linear, if pulling further  $G$  decreases as one would expect from the effect of orbitals stretching mentioned in the previous section. Therefore, the correlated increase of the stiffness and conductance seen over the last plateau gives an indication that a smooth transition zig-zag to linear arrangement occurs.

#### **7.3.4 Why does a chain break**

In Fig. 7.11 we make a statistical analysis over about 2000 traces, constructing a length histogram and averaging the stiffness and the conductance. When looking at the behavior of the stiffness with the chain length, we see that at the peak position in the length histogram the stiffness shows a minimum. This is the position where most of the chain break, indicating the most probable behavior of the stiffness. This minimum value of the stiffness at the breaking point indicate that the chains break stretched. We find a clear correlation between the peaks in the conductance histogram and the oscillation in the stiffness. Since they have the same period this shows that the peaks in a length histogram are a measure of the number of atoms in the chain.

In Fig. 7.12 we divide the length histogram in four regions. We intend to separate the chains as a function of their number of atoms. In order to have more precision in the selection we take only the regions in the length histogram that are centered on the peaks, as shown by the shaded rectangles in Fig. 7.11. Similar to Fig. 7.11, the stiffness and the conductance are averaged over many traces, in this case separately for the given length regime. We see again in all four lengths regimes that the stiffness shows an oscillation with minima centered on the peaks position. If we now look for each length regime in detail we can see that for every case the maximum stiffness for that regime depends on the length of the chain. The chain that will break in a certain regime has always a stiffness higher than the one that survives and increases its length with one more atom. For example in the first regime, the one atom chain has a higher

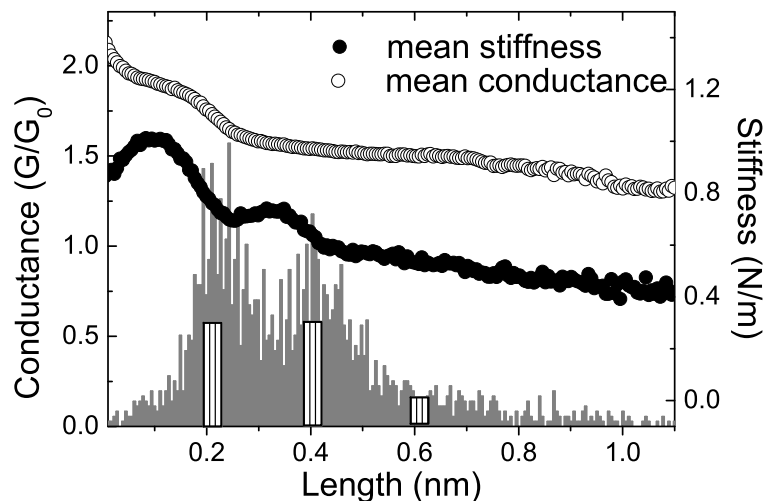


Figure 7.11: Length histogram and the average of the conductance and stiffness for platinum chains. Over 200 traces are included.

stiffness than two atom chain and the same is valid for two to three and three to four atoms long chains. This might be an explanation why a chain breaks with a certain length. For the same displacement (as it's the case in one length regime) a larger stiffness means a larger force applied to the chain. Since there is a maximum force than the chain can hold, longer chains have a smaller stiffness. As a support of our conclusion that there is a certain force needed to break an atomic chain we refer to the force measurements of Rubio *et al.* [2] where they prove that for gold atomic chain this force is well determined being about 1.5 nN, independent of the chain length.

Previous experiments on platinum chains [91], reveal a conductance oscillation that is related to the number of atoms in the chain, the so called even-odd effect. As a function of the matching of the Fermi levels in the chain to the banks, the conductance shows an oscillation with a period of two atomic diameters. Since the electronic and mechanical properties of metallic contacts are interconnected we were looking for an even-odd oscillation in the averaged stiffness, as well. We can see a oscillation, but with half period, as seen in Fig. 7.11. This is related to the relaxation after a new atom is released in the chain, or after the breaking of the chain. This atomic contribution in the stiffness dominates and no electronic oscillation due to the even-odd effect can be distinguished. In the averaged conductance an even-odd oscillation can be identified in Fig. 7.11 and also for chains with more than four atoms, Fig. 7.12d. For shorter chains we see a different period of oscillation. Here the conductance and the stiffness have a correlated behavior, increasing with the elongation, similar to the individual trace shown in Fig. 7.10. This behavior is seen both for two and three atom

Experimental results

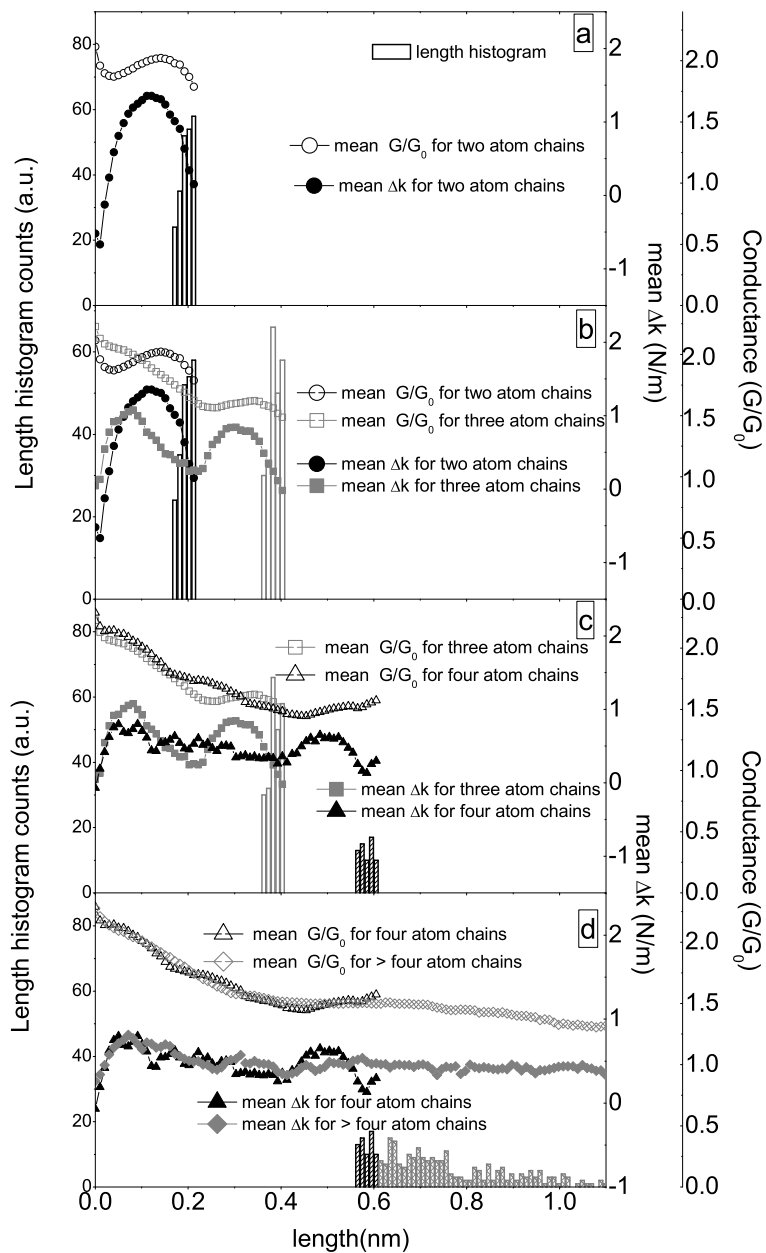


Figure 7.12: Length histogram, average conductance and stiffness for the data in Fig. 7.11 considering the shaded regions.



chains, Fig. 7.12b. This might be related to the transition zig-zag to linear geometry. The fact that we do not observe similar behavior of increasing stiffness and conductance for longer chains, suggests that the chains are formed under sufficient stress that they are linear.

### 7.3.5 The stiffness of an atomic bond

We measure an equivalent stiffness that is the series of the supporting electrodes, or the banks with the chain itself. If we consider the stiffness of the banks constant as a function of the chain length,  $k_b$ , then the effective stiffness will be:

$$k_{eff} = \left( \frac{n}{k_a} + \frac{1}{k_b} \right)^{-1} \quad (7.18)$$

where  $n$  is the number of directional bonds between the atoms in the chain and  $k_a$  is the stiffness of one atomic bond. We can write a set of two equations for the case of two atom chain, where we will have just one bond between the atoms on the tips, and for three atom chain, with two bonds. The effective stiffness is the measured stiffness and we will choose it as the equilibrium value on the last conductance plateau, in between two sudden jump. An average value from 200 traces will be  $k_{eff}=1.7$  N/m for two atom long chains, and  $k_{eff}=1.3$  N/m for 3 atoms. Solving the two equations we will obtain  $k_b=2.5$  N/m and  $k_a=5.5$  N/m. The lower value of the banks stiffness agrees with the assumption that when a chain breaks the broken bond is the one connecting the atoms in the chain to the banks. Note that the lower stiffness dominates the effective value for a series of springs, that means that for short chains the dominant term is the stiffness of the banks, but as the chain length increases, and the stiffness decreases, this contribution decreases. In the case of platinum chains the effective stiffness value ranges from 3 to 0.5 N/m, and for gold chains the values are even lower, around 1 N/m. Our values are about a factor of ten smaller then the values reported by force measurements and calculations [2, 88]. Estimating from this measurements the stiffness of a gold atomic bond we would obtain it of the order of 100 N/m and our value  $k_a$  is about 20 times lower.

A possible explanation could be a lowering of the stiffness due to the contribution of the electrodes. For example two tips touching side-ways would give a soft series spring, that would reduce the effective spring constant. In an experiment that uses STM-break junction technique, one can image the two tips with respect to each other. This experiment was performed on a platinum wire, first broken by the break junction technique and then the tips will scan each other with the help of two shear piezo elements placed below each of them [92]. Atomic resolution could not be easily achieved just by approaching the tips, but also lateral movement was needed. If the tips would be misaligned, they will not face each other but instead two flat surfaces will scan each-other. Another implication of the two tips misaligned is that one cannot go close enough in tunnelling and this decreases the resolution. The results of this experiment may be an indication that the Pt tips are misaligned.

## Experimental results

Although the absolute value of the stiffness is not very reliable, we can still see that qualitatively the stiffness is correlated to the reconfigurations in the contact.

### 7.3.6 Stiffness in the tunnelling regime

In Fig. 7.13 we present a measurement during the reverse process of recovering the contact. As the distance between the electrodes is reduced a jump to contact occurs. However the distance at which the jump to contact will appear depends on the ratio between the attractive force and the stiffness of the electrodes that is a measure of the binding energy of the atoms in the electrodes. A larger elastic constant of the electrodes will give an later jump to contact. Just before the jump one observes a exponential dependence of the conductance with the distance, as expected for the tunnelling regime. Into this regime three forces should be considered: van der Waals and electrostatic forces, that give long range interaction and a short range force due to metallic cohesion. The electrostatic force can be neglected in our case since the bias voltage applied between the electrodes is typically 10 mV. If we consider two identical paraboloidal tips the van der Waals force acting between them is given by:

$$F_{vdW} = -\frac{A_H R}{12(x - x_0)^2} \quad (7.19)$$

with  $R$  the curvature of the two tips and  $A_H = 3.3 \times 10^{-19} \text{J}$  is the Hamaker constant for platinum [93].  $x_0$  is the correct origin for van der Waals force and should be close to minus twice an atomic radius.

In the short range the metallic cohesion energy has the form:

$$E = -E_b \left(1 + \frac{x - x_m}{\lambda}\right) \exp\left(-\frac{x - x_m}{\lambda}\right) \quad (7.20)$$

where  $E_b$  is the binding energy,  $x_m$  is the separation at  $E = -E_b$  and  $\lambda$  is a parameter that gives the range of the metallic interaction. Considering both van der Waals and metallic cohesion contributions, one obtains the expression for the stiffness as:

$$k = \frac{E_b}{\lambda^2} \left(1 - \frac{x - x_m}{\lambda}\right) \exp\left(-\frac{x - x_m}{\lambda}\right) - \frac{A_H R}{6(x - x_0)^3} \quad (7.21)$$

No clear contribution was seen in the experimental data from the van der Waals force, therefore in the fit we will consider only the first term in the Eq. 7.21, representing the metallic cohesion. An example of the fit is shown in Fig. 7.13, where we choose as fitting parameters  $E_b$ ,  $\lambda$  and  $x_m$ . The obtained fitting parameters for several data sets are shown in Table 7.1. From our fit we cannot obtain with precision all three parameters because of the relatively low signal to noise ratio. Therefore we fix one parameter, in this case  $E_b$ , at values similar to what was reported by Rubio-Bollinger *et al.* [88] and varying it manually while the other two parameters are varied in the fitting procedure. As

it regards the order of magnitude, the parameters are in good agreement with the ones obtained by Rubio-Bollinger *et al*, although they have some variations.

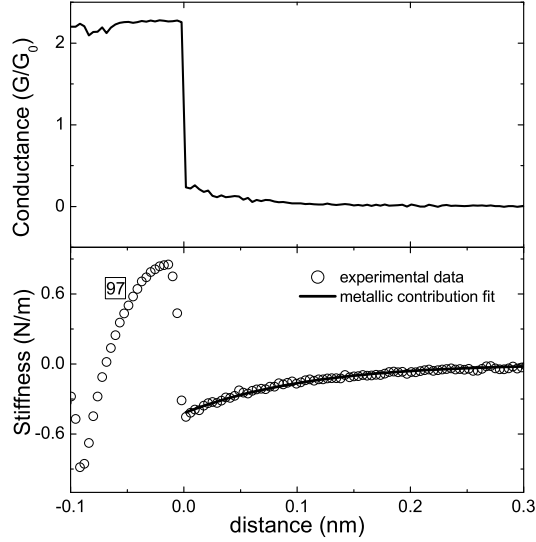


Figure 7.13: Measurement of the conductance and stiffness in the tunnelling regime as a function of the distance between the platinum electrodes. The stiffness is fitted with the metallic cohesion contribution, given by the first term in eq.7.21.

set	$E_b/\lambda(nN)$	$E_b(eV)$	$\lambda(pm)$	$-x_m(pm)$
97	0.96	0.49	81.1	376
91	3.7	0.83	35	269
103	2.5	0.61	37.9	243
42	5	0.68	21.7	236
60	2.9	0.7	37.7	290
100	1.03	1.13	65.4	388
70	2.5	0.5	31.7	259
44	7	1	22.6	184
60	9	2	34.3	311
106	2.7	0.5	29.3	193

Table 7.1: Parameters obtained from the fits of the experimental data

In order to verify the obtained parameters we calculate the value of  $E_b/\lambda$  (first column in Table 7.1) that is expected to be of the order of the breaking force for one atom contact. This value is not obtained from the fit, but is calculated from the individual parameters obtained,  $E_b$  and  $\lambda$ . From the force

### Experimental results

measurements on gold [29], the breaking force for a one atom contact is reported to be 1.5 nN. However for platinum one would expect to have a larger breaking force if we have in mind the bulk Young modulus which is two times higher than for gold. a rough estimation would then give for  $E_b/\lambda = 3nN$ . Looking at the values of  $E_b/\lambda$  on the first column in Table 7.1, we see a large variation between 1 and 9 nN, still 6 of them are between 1 and 3 nN.

Also for the tunnelling regime if we compare the averaged stiffness value for platinum just at the moment where the jump to contact occurs to the results obtained by Rubio-Bollinger *et al* for gold, we have a value 4 times lower [88].

#### 7.3.7 Stiffness of gold atomic contacts

Similar behavior to the results presented for platinum is observed for the stiffness of gold atomic contacts (Fig. 7.15). The jumps in the stiffness and the conductance are correlated. The value of the elastic constant is in average two times smaller than for platinum, which is reasonable, given a factor of two lower Young's modulus for bulk gold. Over the elastic stage we see that differently from platinum, for gold the stiffness does not show only the regular smooth decrease with stretching, but it can also increase, as for example at the plateau at about  $3 G_0$ . The conductance plateaus are straight while for platinum they had a negative slope as a function of stretching, that is an effect of the  $d$  orbital stretching. Since we see that the stiffness follows in both metals to some extent the conductance behavior, it is tempting to attribute it to the same effect.

In Fig. 7.15 we concentrate on the last plateau before rupture, that corresponds to an one atom contact. From the exceptionally long plateau at  $1 G_0$  we can conclude that a chain of atoms has formed. The conductance of the chain is almost constant at a value of about  $1 G_0$ . We can identify sudden relaxations in the stiffness that are more or less periodical with the interatomic distance that gives an indication that the jumps in the stiffness coincide with the moment an atom is released in the chain. If we perform the same type of analysis as for platinum and average the stiffness as a function of the number of atoms in the chain, one would obtain the result shown in Fig. 7.16. The stiffness obeys again the rule that we found for platinum: for the same length range, the chains with lower  $k$  value in that range will survive pulling one more atom in the chain. One cannot identify clear oscillations as in the case of platinum, correlated with the peaks in the length histogram. In the case of gold the resolution is smaller than for platinum, since the stiffness is smaller.

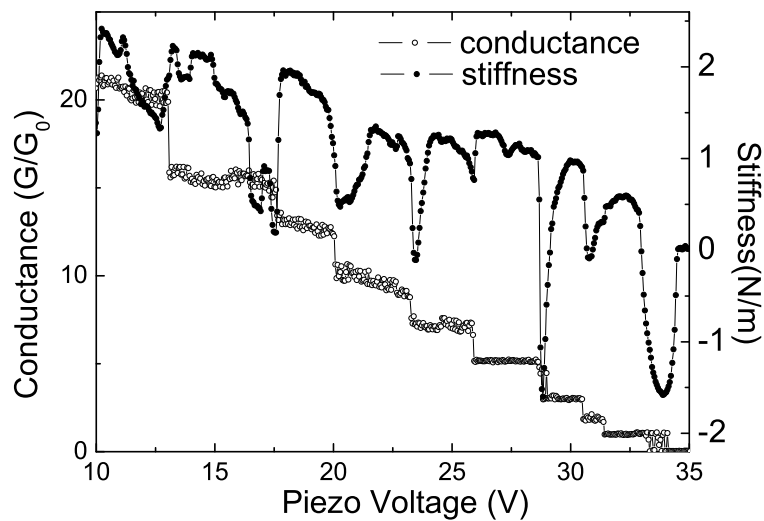


Figure 7.14: Simultaneous measurement of the stiffness and the conductance for gold atomic contacts at liquid helium temperature as a function of the piezo voltage.

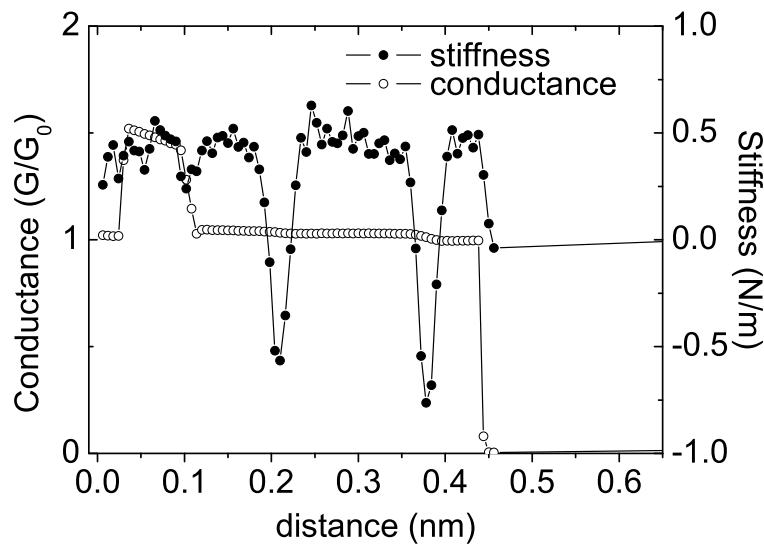


Figure 7.15: Measurement of the stiffness for the last conductance plateau for gold.

Experimental results

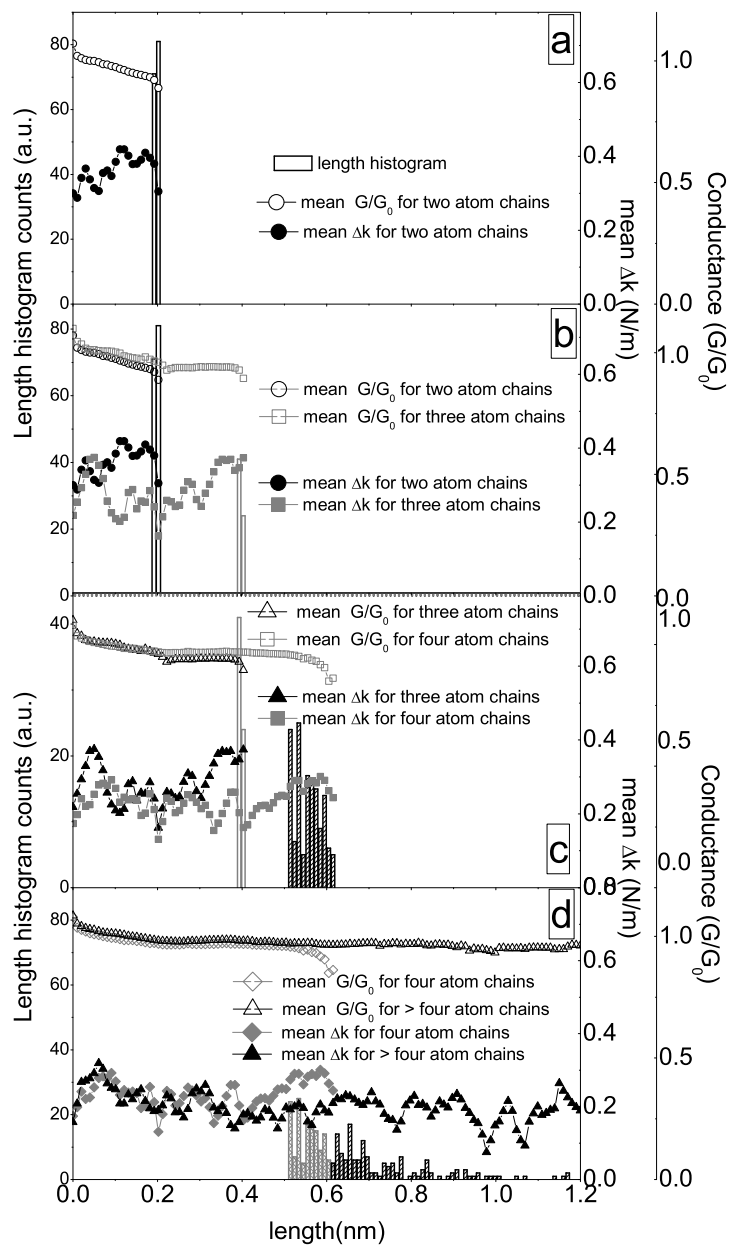


Figure 7.16: Analysis of the average conductance and stiffness for the gold chains. The bars indicate the regime in the length histogram considered in the average.

### 7.3.8 Measurements on Au at room temperature

We performed measurements of conductance and stiffness on gold contacts at room temperature (RT) under high vacuum environment with a base pressure of around  $1 \times 10^{-5} Pa$ . It has been shown that shell effects occur at RT in gold, and moreover they survive under ambient conditions. We have an indication of shell effects in our measurements, a typical histogram being shown in Fig. 7.17. We plot the peaks positions in units  $k_F R$ , as we usually analyze the period of the stable diameters. The period of the peaks is  $\Delta k_F R = 0.96$  as obtained for regular electronic shell effect in gold at RT-UHV. An unexpected peak below  $1G_0$  is observed that might be an indication of the presence of contamination.

Since the stable diameters relate to minima in the free energy of the nanowire, we would expect to observe some evidence in their mechanical properties as well [15], [25], [28]. The force should show relative minima for the peaks related to shell filling. As a result in the stiffness we expect to observe higher values, since the stability would be reflected in a resistance to elongation. In chapter 2 we have calculated the stiffness oscillation due to the electron confinement in the transversal direction. We obtained an order of magnitude of few N/m that would be a measurable effect. From the stiffness data one can get extra information about the stable diameters. While from a conductance trace we can only say if a diameter appears or not during the elongation, the stiffness would give the weight of how stable this diameter is.

Given the small frequency shift we usually obtained and the lower quality

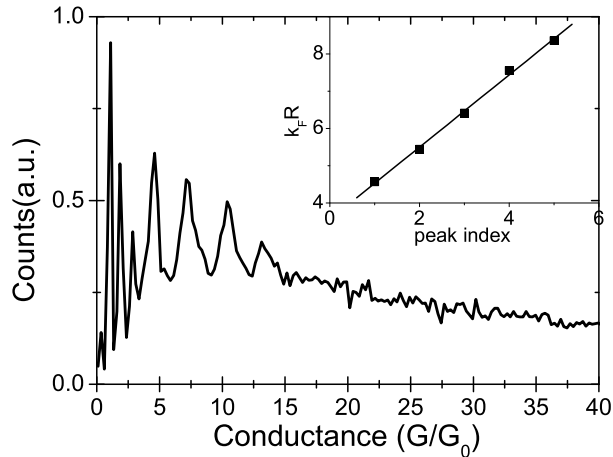
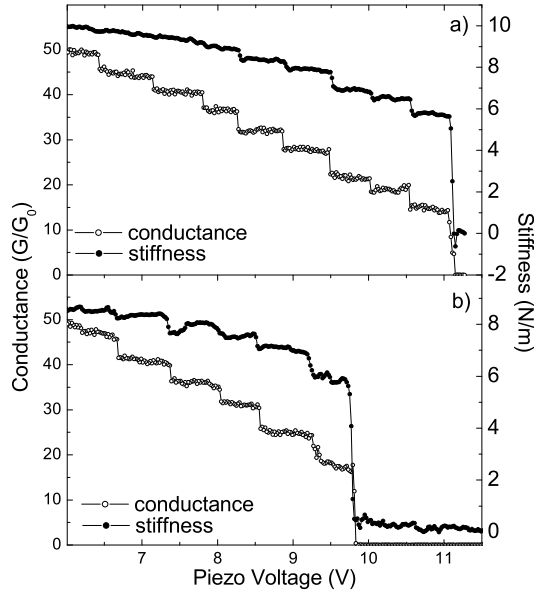


Figure 7.17: Conductance histogram for gold at room temperature under high vacuum conditions built from 1000 traces. In the inset is plotted the peaks position converted to  $k_F R$  as a function of the peak index. The slope indicates a period  $\Delta k_F R = 0.96$  similar to what is obtained for electronic shell effect in gold at RT-UHV

*Experimental results*



*Figure 7.18: Stiffness and conductance traces for gold at RT-HV as a function of the piezo voltage in the breaking process, when the contact is pulled a) and in the return process of recovering the contact b).*

factor that is at room temperature typically below 1000, this gives relatively small resolution in the measurement. The lower value of  $Q$  is caused mostly by the poor vacuum conditions that will produce dumping of the tuning fork. A second problem that we face is the limited time for measurement, since at this pressure the contamination of the wire would appear after a few hours from the breaking moment. We have an advantage in choosing gold since it is proven to be less reactive, by the fact that we can see signs of electronic shell structure at room temperature even under ambient conditions.

Simultaneous measurements of the conductance and stiffness recorded at RT-HV are shown in Fig. 7.18 a). While the conductance decreases in steps from about  $50 G_0$  to 0, the stiffness follows this behavior with approximative constant values on the conductance plateau and small jumps at the yield stage. The stiffness behavior over the plateau is different than in the low temperature measurements, where it showed a smooth variation over the plateaus. One expects a different behavior since the mobility is enhanced, the configuration being more dynamic and adjusting itself to a more stable one. At room temperature, the rearrangements take place on much smaller time scale.

In the elongation process the contact breaks at a relatively large diameter, mostly the last plateau being at about  $5 G_0$ . It was seen that small contacts are not stable at room temperature, due to thermal fluctuations. The force



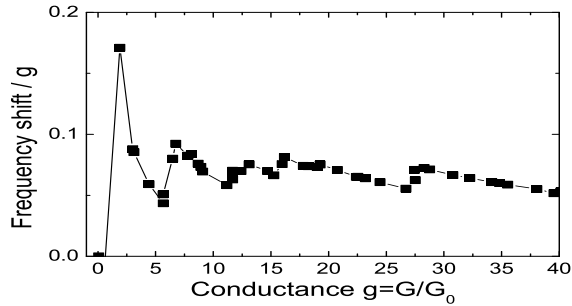


Figure 7.19: Frequency shift,  $\Delta f$ , (proportional to the stiffness) normalized to the conductance.

measurements are relatively slow taking about 1 minute per trace. We have seen that the small contacts are unstable when the breaking time is too large. The conductance histogram shows clear peaks at the low diameters, but in this case one conductance trace is recorded in about 1 second. A trace recorded during the compression stage is shown in Fig. 7.18b). Again a very abrupt jump in the conductance occurs from 0 to a contact of  $18 G_0$ . The tunnelling contribution is in most of the cases absent. The stiffness trace behaves similarly to the elongation process. In the tunnelling regime we do not observe the attractive force as seen at low temperatures, but a smooth increase in the stiffness before the jump to contact. Looking at the stiffness normalized by the surface area, we observe again an increase as the diameter decreases (Fig. 7.19), similar to the result at low temperature. In different traces the effect can be more or less pronounced depending on the contact evolution. On top of this increase, we observe some small oscillation. In this example some maxima are observed at conductance values of 2, 7, 13  $G_0$ . Although their oscillation is not very pronounced, we can consider the possibility that they might be correlated to the peaks in the histogram from Fig. 7.17.

In order to verify their reproducibility we perform an average of the stiffness over several traces (in this case 70) while also constructing a conductance histogram. An example is shown in Fig. 7.20. The period of the oscillation is found from the plot in the inset to be  $\Delta k_F R = 0.83$ . Here the positions of the relative maxima in the average stiffness from Fig. 7.20 (on the conductance axis) are plotted as a function of their index. The value of the slope is somewhat different than what expected from electronic shell effect for Au. Moreover the oscillation seen in Fig. 7.20 is less pronounced in other sets of data. Due to insufficient statistics, we cannot claim that the maxima in the stiffness are related to shell effect. There might be several reasons for the absence of the shell effect signs in the stiffness. Firstly, similarly to even odd effect, we have a competition between the atomic and electronic contributions in the stiffness. If the atomic part dominate that will give the sudden relaxations at the rearrangements, we will not be able to distinguish in the total stiffness the electronic shell effect

## Experimental results

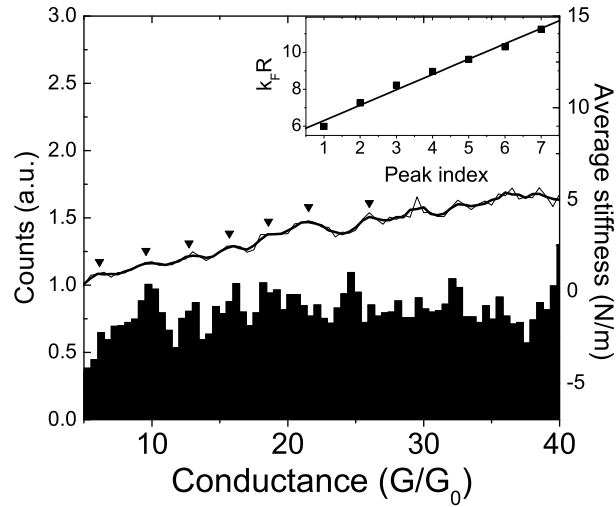


Figure 7.20: Conductance histogram and the averaged stiffness calculated from 70 individual breaking traces. Inset: the position of the maxima of stiffness from a) converted to  $k_F R$  vs. peak index. The linear fit gives the oscillation period  $\Delta k_F R = 0.83$  that is lower than what obtained for electronic shell effect for gold,  $\Delta k_F R \simeq 1$ .

contribution. The second reason might be the contamination influence, that causes lower resolution in the measurements, due to a relatively low quality factor, together with the low frequency shifts. Moreover, it is suggested from a theoretical calculation that contamination can give variations in the values of the stiffness, depending on the position of the impurity [24]. Averaging over this contribution might cause a smoothness of the oscillations due to the electronic shell effect. Given these considerations, experiments performed in UHV would prevent the contamination and at the same time would give the possibility of improving the statistics.

### 7.3.9 Conclusions

In this chapter we have addressed different aspects of nanowire stability by analyzing their electrical and mechanical properties by simultaneous measurements of conductance and stiffness with the help of a MCBJ technique combined with a tuning fork as a force sensor. Firstly we have investigated the formation of contacts formed of just a few atoms in cross-section including the case of monoatomic chains for platinum and gold at cryogenic temperatures. The stiffness presents two stages during elongation: an elastic stage, over a plateau of conductance, where both stiffness and conductance show correlated behavior that can be related to orbital stretching; in the yield stage the conductance

shows a sudden step at a reconfiguration, while the stiffness shows a jump related to relaxation. Exceptional increase in the stiffness and conductance over the last plateau for two or three atom chains can be related to a transition zig-zag to linear arrangement. The formation of monoatomic chains was observed in the stiffness measurement. Minima in the stiffness are related to the breaking of the chains, indicating that the chains break stressed. The average stiffness of the chains has the same period as the peaks in the length histograms. This supports the idea that the peaks are a measure of the number of atoms in the chains. We have found evidences that the stiffness of the starting configuration influences the length of the chain: shorter chains have a higher stiffness. In the tunnelling regime we have observed the attractive force due to the metallic cohesion. Secondly we searched for the influence of shell effects in the stiffness of gold nanowires at room temperature. We have studied the stability of nanowires up to hundreds of atoms in cross-section. We can observe evidence of electronic shell structure in the conductance measurements but they are not enough reproducible in the stiffness data. More statistics and better vacuum conditions might lead to the observation of the shell effect in the stiffness.

# VIII

## Search for shell structure by electrochemically controlled gold nanowires

### 8.1 Introduction

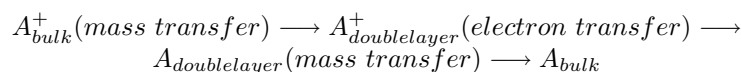
Electrochemistry is a very old field of research that dates since the beginning of the 18-th century when the first device to produce electricity was discovered by A. Volta. In the recent years, the interest in electrochemistry application to nanoscale devices increased. The first application was using a combination of electrochemistry with AFM or STM [94, 95]. Later on it was shown that electrochemistry can be used as a self standing technique in fabricating nanoscale contacts [96, 97]. Several experiments were performed on controlling contacts formed of a few atoms for materials like Au, Ag, Cu, Pb, Zn [98, 99, 100, 101]. Here we will extend the studies to the formation and stability of thicker gold nanowires, in order to study the "magical" diameters that we obtained by the MCBJ technique. It is desirable to be able to keep a nanowire stable for long time and to increase its length by finely adjusting the electrochemical potential. An advantage of working in the solution is that the sample can be kept clean, without using sophisticated instrumentation, such as a UHV set-up. Moreover, one can reversibly form and break the nanowire by controlling the electrochemical voltage. Electrochemical fabrication of atomic scale contacts opens a new area of possibilities, such as controlled atomic scale deposition, fabrication of molecular junctions, gated atomic contacts. The operation at room temperature under ambient conditions, brings the atomic contacts closer to possible technological applications. It has been shown that these systems can act as a switch, being the first step in controlling an one atom transistor [102].

---

This work was done in collaboration with M. R. Calvo, C. Untiedt and V. Climent, Universidad de Alicante, Spain

## 8.2 Working principle

The electrochemical process is based on charge transfer at the interface between an electronic conductor, and active species in the electrolyte. By tuning the potential of the electrode with respect to the solution, electrons from the electrode will occupy available states in the solution. By raising the energy of the electrons from the electrode they will flow into the solution. At the interface metal-solution, the reactant  $A$  present in solution will be reduced, as depicted in Fig. 8.1(a). Inverting the potential, the reactant will be oxidized (Fig. 8.1(b)). The potential at which the reaction occurs depends on the specific reactants present in the system. One has to take into consideration that the electrochemical system is not homogeneous. The reaction takes place at the metal-solution interface, and therefore close to the electrode the concentration is dynamically modified, while in the bulk solution, the concentration is in general constant. Two length scales are significant in the electrochemical processes: the double layer and the diffusion layer, as shown in a simplified picture in Fig. 8.2. Due to the electron transfer metal-solution, the surface of the metal holds an excess charge. In order for the interface to remain neutral, the charge is balanced by the ions attracted from the solution. This will form the double layer, that will have a width given by the ion radius, being in the range of a few Å. Electrically, the double layer can be seen as a capacitor. The distance over which the concentration of the reactants is significantly affected by the reaction taking place at the electrode is called the diffusion layer. The diffusion layer is significantly larger than the double layer, being in between  $10^4 - 10^7$  Å. The speed of the reaction is controlled by this diffusion layer. Thus the electrochemical processes consists of charge and mass transfer, as shown in the scheme below:



From the bulk solution to the diffusion layer the ions are mass transferred by diffusion, due to a concentration gradient, migration and convection (stirring). The dominant mechanism is in our case the diffusion. The migration is less significant in macroscopic cells, where the electrodes are situated at large distances, because the screening length of the electric field in the solution is in the order of 1-100 nm. Since we work with steady solutions, also the convection mass transport is mostly absent.

When applying a potential to the electrode, the potential gradient in the solution will decrease with the distance from the electrode, being mostly concentrated in the double layer, as seen in Fig. 8.2. In the bulk solution the potential is constant.

## 8.3 Electrochemical cell

A typical electrochemical cell contains three electrodes. The electrical process is controlled by a potentiostat. A current is applied in between the counter (CE)

Electrochemical cell

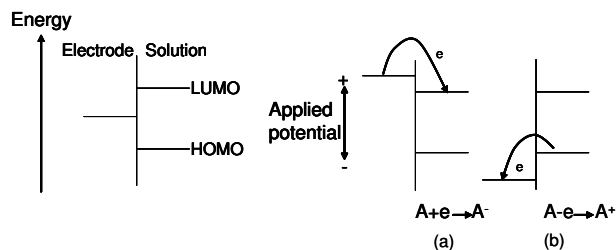


Figure 8.1: Energy levels of the solution with highest occupied molecular orbital (HOMO) and lowest unoccupied molecular orbital (LUMO) and the Fermi energy of the metal electrode. By adjusting the potential of the electrode, the electrochemical reduction (a) and oxidation (b) of a species A in solution occur.

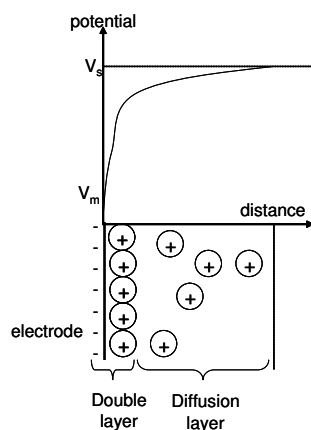


Figure 8.2: Simplified model showing the significant regions close to the metal solution interface.

and the working electrode (WE), and the potential of the WE is monitored with respect to the reference electrode (RE). The RE should have a fixed potential, independent on the reactions taking place in the solution. This is ensured by the potentiostat that doesn't allow any current to flow between the RE and the other two electrodes. A simplified electronic scheme of the potentiostat is shown in Fig. 8.3. From the DAC card of the computer we apply a voltage to the input of the operational amplifier (OPA). The OPA will measure the voltage on the RE and send a current into the CE until the two input voltages will be equal. One of the reasons for using a RE is to exclude the voltage drop that takes place at the interface CE-solution, as described in Fig. 8.2. This voltage drop will vary depending on the reactions taking place at the CE, and the potential difference measured between CE and WE will not be well defined.

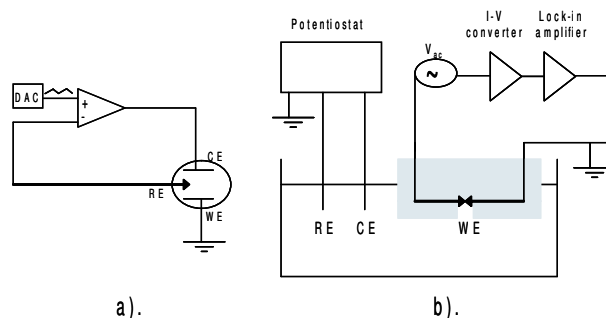


Figure 8.3: Simplified scheme of the potentiostat (a). (b): scheme of the electrochemical cell and the measurement configuration. The WE is covered by a insulating material (gray area), exposing only a small part of it to the solution, typically about 100  $\mu\text{m}$ .

The RE measures the difference in potential between the WE and the solution. If one would measure only with two electrodes one can find the difference in potential between the two. For relatively low currents, below  $\mu\text{A}$  the potential reading will not be influenced by the reaction [103]. In these conditions the use of a potentiostat can be avoided. Indeed we have seen that for low concentrated solutions when the current is in the order of  $\mu\text{A}$  there is no significant difference between the voltammograms recorded using only two electrodes (as WE and CE) and the ones using in addition the RE and the potentiostat.

## 8.4 Electrolysis of gold

In order to characterize the reactions occurring in the solution, one needs to record current-potential curves, called voltammograms. The voltage of the RE is swept and the resulting current between the CE and WE is measured. A typical voltammogram is shown in Fig. 8.4. We use a quasi-RE that is a 1 mm diameter gold wire, the same as the CE. The WE is a gold wire of 0.1 mm diameter. We want to reversibly dissolve and deposit gold on the WE. Gold is chemically one of the most stable metals, having a relatively high oxidation-reduction potential. In normal aqueous solutions, the dissociation of water will occur at lower potentials, the oxidation/reduction of gold being hindered. For the electrolysis of gold one needs to use a solution where gold forms a stable complex, that will have a lower redox potential. In this respect, NaCl and the cyanide electrolytes in aqueous solutions are good candidates. The voltammogram shown in Fig. 8.4 is recorded in a solution made of NaCl and AuCl<sub>3</sub> and a supporting electrolyte consisting of H<sub>2</sub>SO<sub>4</sub>, that is chemically inactive for the reaction. The role of the supporting electrolyte is to ensure a good electrical conductivity of the solution, in order to avoid large voltage drops in the solution, and at the same time it helps keeping the pH of the solution constant. Gold

### Electrolysis of gold

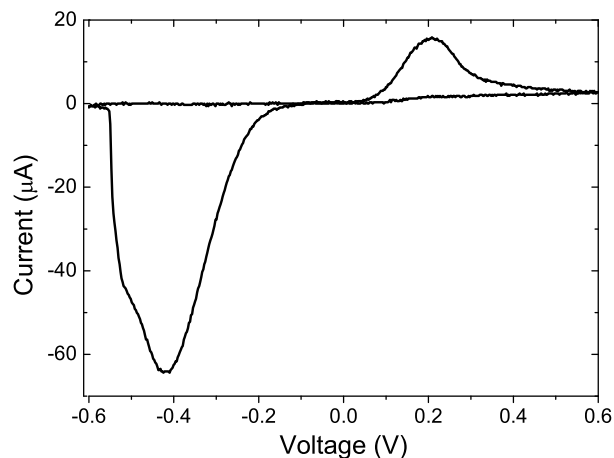
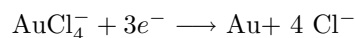


Figure 8.4: Voltammogram showing the current flowing between the CE and the WE as a function of the voltage of the RE. The solution is 1M NaCl + 0.02M AuCl<sub>3</sub> and a supporting electrolyte consisting of 1mM H<sub>2</sub>SO<sub>4</sub>. All three electrodes are gold wires. The peak representing the dissolution of gold is centered at about -0.4V, while the deposition peak is around 0.2V.

forms a chlorite complex, that can be reduced in the reaction:



The solution contains added AuCl<sub>3</sub> in order to increase the deposition rate on the WE. The peaks in the voltammogram from Fig. 8.4 show the cyclic deposition/dissolving of the gold WE. Around  $V = -0.4V$  we have a peak representing the dissolution of gold, and the deposition peak is at about  $V = 0.2V$ . The deposition peak is about three times smaller than the dissolution peak, and one of reasons can be that AuCl<sub>3</sub> has a lower concentration than NaCl. The asymmetric values of the deposition/ dissolution peaks are somewhat unexpected, since the electrochemical system is symmetrical, both CE and WE are gold. A possible explanation can come from the difference in the geometry of the two electrodes, that will affect differently the voltage drop at every of the electrodes.

A voltammogram proves that the reactions have a specific potential. In ideal conditions, there should be a step at the reaction potential, followed then by a plateau. The smooth increase in the absolute value of the current is due to the broadening of the energetic levels of the solution. The decrease in current after the maximum can have several reasons. In the case of deposition the decrease is due to current limitation by diffusion. As explained in the previous section, the reaction takes place with species inside the diffusion layer, therefore this layer should be renewed in order to continue the reaction. The position and the width of the peak depends on the speed of sweeping the voltage. In the dissolution case, one can see a more abrupt decrease. This has been commonly



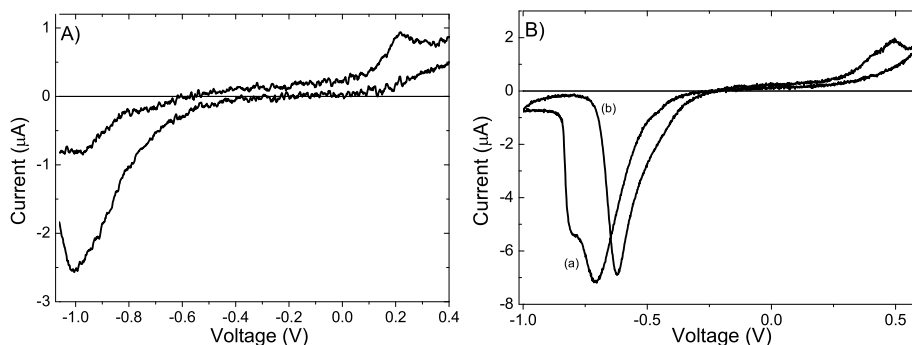
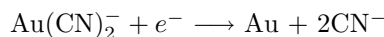


Figure 8.5: A) Voltamogram of the gold sample in a solution of 30mM KCN and 6mM  $\text{KAu}(\text{CN})_2$  with a buffer composed of 1M  $\text{KHCO}_3$  and 0.2M KOH. The RE and the CE are gold wires. The deposition/ dissolution peaks for gold are centered at 0.2V / -1V. B) Voltamogram of the gold sample in a solution of 0.1M KCN and a buffer of 1 M  $\text{KHCO}_3$  and 0.2 M KOH. The RE and the CE are gold wires. The gold deposition/ dissolution peak is at about 0.5/ -0.7.V.

attributed to the metal passivation due to the formation of a thin gold-oxide film [104]. This is an instructive example that in electrochemistry it is not implicit that increasing the voltage, the process will go faster, but depending on the reactions that occur, it can also be hindered. Understanding the features present in the voltammograms is the first step in controlling the electrochemical process. In addition the voltamogram gives information about the cleanliness of the system.

Alternatively we have used a cyanide based solution. Cyanide is industrially used for Au electroplating, providing a homogeneous gold deposition. It is reported that in this way one can deposit single crystal films [105]. Fig. 8.5 A) shows a voltamogram for gold electrodes with a solution composed of potassium cyanide (KCN) and potassium cyanaurate ( $\text{KAu}(\text{CN})_2$ ) with a buffer of potassium bicarbonate ( $\text{KHCO}_3$ ) and potassium hydroxide (KOH). The buffer has the role of keeping the solution pH constant. For safety the cyanide based solutions should be used in basic media, in order to avoid the evaporation of HCN that is very toxic. The deposition reaction is:



In the voltamogram from Fig. 8.5 one can see that the dissolution/deposition peaks are different than in the case of chlorite based solution. The electrochemical current is more than ten times lower, in the cyanide based solution. This is expected since the concentration is about ten times lower. Moreover the voltage difference between dissolution/deposition peaks is much larger. In this case we have access to a broader voltage range, that can make the process of deposition/dissolution more controllable. Similar to the chlorite solution, at voltages

### *Device design*

below  $-1V$ , a decrease in the electrochemical current occurs, that can have the same origin of gold oxide formation. One can see an additional indication of that in the voltamogram from Fig. 8.5B). The solution is more concentrated in this case  $0.1 M$  KCN, and the current is larger. Moreover the dissolution peak appears at lower voltages. The diffusion layer depends on the ion concentration in the solution influencing the position of the peaks for dissolution/deposition. Here in the negative regime in the return process (b), a dip appears at a voltage of about  $-0.7V$ . Normally one would expect a zero current in the return process. This is an indication that an oxide layer forms on the electrode that is removed when decreasing the voltage.

## 8.5 Device design

The working electrode that we will reversibly etch and deposit is a macroscopic poly-crystalline gold wire of  $100\mu m$  diameter. The wire is covered in a insulating material and only a small part of it is exposed to the solution. The insulating material is polyethylene, a chemically inert material for the type of solutions we use. The sample preparation procedure is as follows: the polyethylene granules are melted and the wire is mounted inside and completely covered. The polyethylene is then pressed making sure that it seals the wire properly. When the sample is solid again, a notch is cut in the insulation until the wire is exposed. In this way one can expose to the solution only about  $100\mu m$  of the gold wire. The first breaking time can be derived from Faraday's law as :

$$t = \frac{\pi R^2 l \rho n F}{MI} \quad (8.1)$$

with  $R, l$  being the radius and the length of the wire,  $\rho$  is the gold mass density,  $n$  is the number of electrons per ion that participates in the reaction,  $F = 96,485$  is the Faraday constant,  $M$  is the molar mass for gold, and  $I$  is the electrochemical current intensity. We obtain typically breaking times of the order of 1 to 10 hours depending on the type of solution, the solution concentration and the voltage applied. The experimental breaking times agree with the estimation from eq.8.1.

## 8.6 Experimental results

### 8.6.1 Conductance traces

The electrical measurement scheme is shown in Fig. 8.3. During the dissolution process we apply a constant electrochemical voltage, and measure the conductance of the wire. The conductance is measured by applying an ac voltage with an amplitude typically lower than  $10 mV$ , the resulting ac current is converted to a voltage by a commercial current to voltage converter. The output voltage is read by a lock-in amplifier. The data are recorded using an digital to analog (DAC) data acquisition card.

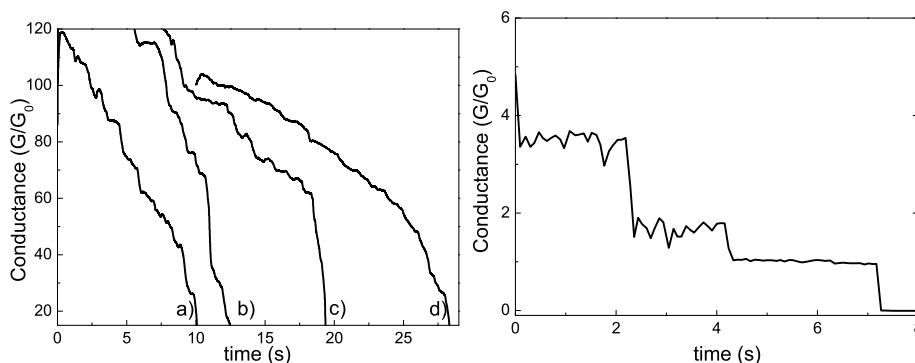


Figure 8.6: Left: Conductance traces recorded during the breaking of the contact at an electrochemical voltage of  $-0.2V$ . The solution used was  $30mM KCN$  with  $6mM KAu(CN)_2$  for traces a), c), d) and  $10mM KAu(CN)_2$  for trace b) Right: Breaking conductance trace showing a plateau at  $1G_0$ .

Once the sample is initially broken, by choosing a proper deposition voltage, one can recover the contact. The wire can be reversibly dissolved and deposited. In Fig. 8.6 left we present a few conductance traces for a Au sample. The wire is broken by an electrochemical voltage of  $-0.5V$  above  $G=100 G_0$ , while below this value the voltage is reduced to  $-0.2V$ , in order to ensure a slower breaking. The wire can be reversibly grown by applying a deposition voltage, in this case  $0.4V$ . No clear sequence of steps can be seen in the traces. This is different from what we have observed in the measurements of gold with the MCBJ in UHV-RT, where the thinning down occurs in steps.

We have observed that the contacts are typically very unstable in the range below  $100 G_0$ . One way of improving the stability is by performing repeated cycles of deposition/dissolution. We start breaking typically from values of  $2000 G_0$ . We break the contact step-wise, with a step of  $100 G_0$  stopping at every step and by adjusting the electrochemical voltage we stabilize the contact at that particular conductance. This preparation has as purpose of helping the contact to find more stable configuration in order to be able to observe the formation of contacts smaller than  $100 G_0$ , that otherwise will break too fast.

The speed with which the contact is dissolved increases with decreasing its diameter and contacts formed of just a few atoms are very unstable. Exceptionally, sometimes in the breaking process a plateau close to  $1G_0$  occurs, as for example in Fig. 8.6 right. We have observed that more often a contact of  $2 G_0$  will occur, as one can see in Fig. 8.7. Here there are also plateaus near 3 and 4  $G_0$ . We have seen the enhanced stability of a contact having a conductance of  $2 G_0$  in the MCBJ measurements for gold.

In Fig. 8.8 we present a histogram constructed from 145 selected traces. We have selected only the traces that have a step structure. In order to find the period of the peaks in the histogram of Fig. 8.8 we plot the peak position in

### Experimental results

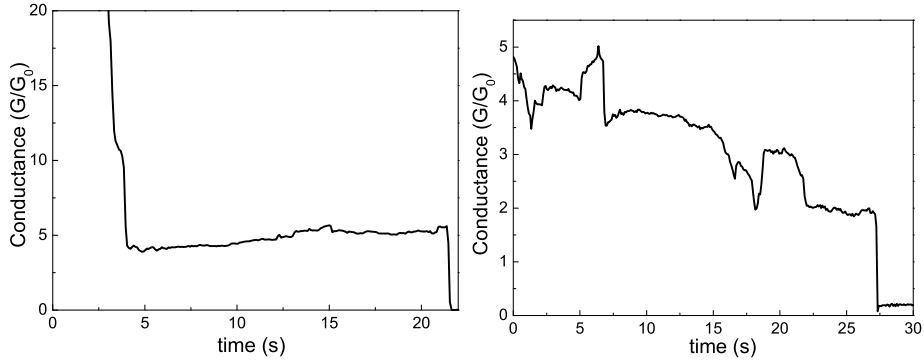


Figure 8.7: Two breaking conductance traces. In the left figure one can see a long plateau around  $5 G_0$ . The right trace shows plateaus near  $4, 3.5, 3, 2 G_0$ .

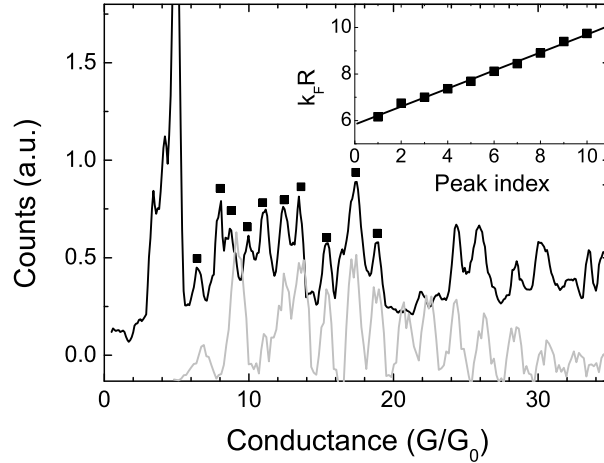


Figure 8.8: Conductance histogram constructed from 145 selected traces of repeated dissolution/ deposition of the wire (black curve). A histogram recorded for a poly-crystalline gold wire with the UHV-MCBI is shown for comparison, gray curve. Inset: the period of the peaks (for the histogram obtained in the electrochemical process) is found from the linear fit of the peak position as  $\Delta k_F R = 0.4$ .

$k_F R$  as a function of the peak index. From the linear fit we obtain a period of  $\Delta k_F R = 0.4$ . The value is similar to the atomic shell effect period obtained for gold in the MCBJ at RT-UHV. Moreover we get a very good agreement in the peak positions with a histogram recorded in UHV for a poly-crystalline gold wire.

### 8.6.2 Stabilizing certain diameters

In order to compare the stability of different diameters one can use the advantages of the electrochemistry of being able to adjust the electrochemical voltage in order to keep a certain contact stable. For the low conductance regime (below  $3 G_0$ ) Li *et al.* [96] show that it is possible to stabilize the nanowire at integer values of conductance quanta for hours. Contrary, contacts that have fractional value of conductance cannot be easily stabilized, drifting towards integer values after several minutes. With the help of a simple software controlled feedback we can adjust the electrochemical voltage such to keep a certain conductance constant. The feedback loop compares the conductance value to a preset value and adjusts linearly the electrochemical voltage. With this simple feed-back it is very easy to keep the conductance at a given value, and for most of the cases the variation in the electrochemical voltage are relatively small of the order of tens of mV, as it will be seen below. In our search for preferred diameters due to shell structure, we expect to see a lower variation of the conductance and electrochemical voltage for the stable nanowires. We succeeded in stabilizing any desired value of conductance down to values around  $10 G_0$ . The conduc-

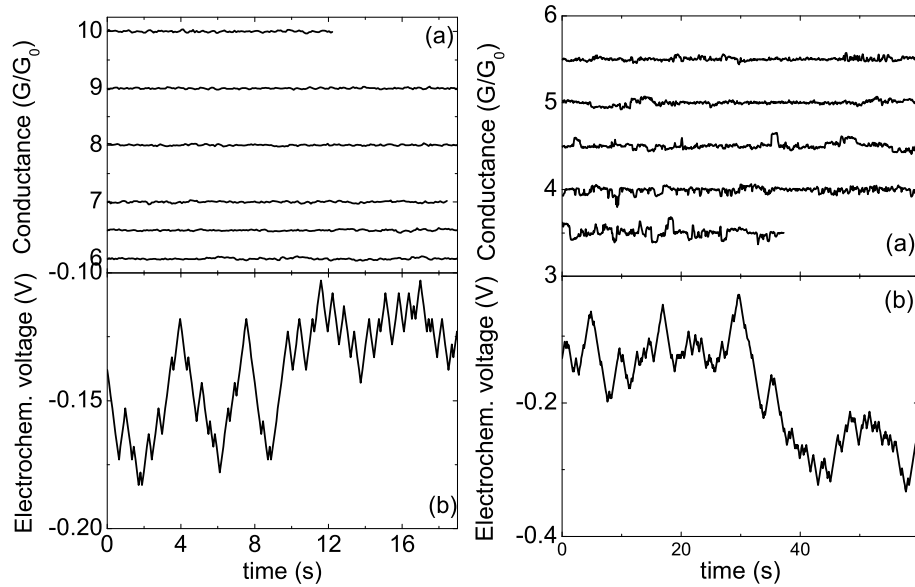


Figure 8.9: Stabilizing contacts in the region where the shell effects have been observed to influence the formation of the nanowires in the MCBJ experiment. In (a) the conductance is plotted and in (b) the electrochemical voltage that is provided with the help of the feed-back in order to stabilize a given conductance value. We show the voltage used to stabilize  $8 G_0$  and in the right figure  $4 G_0$ . For the other values of conductance very similar values are obtained.

Experimental results

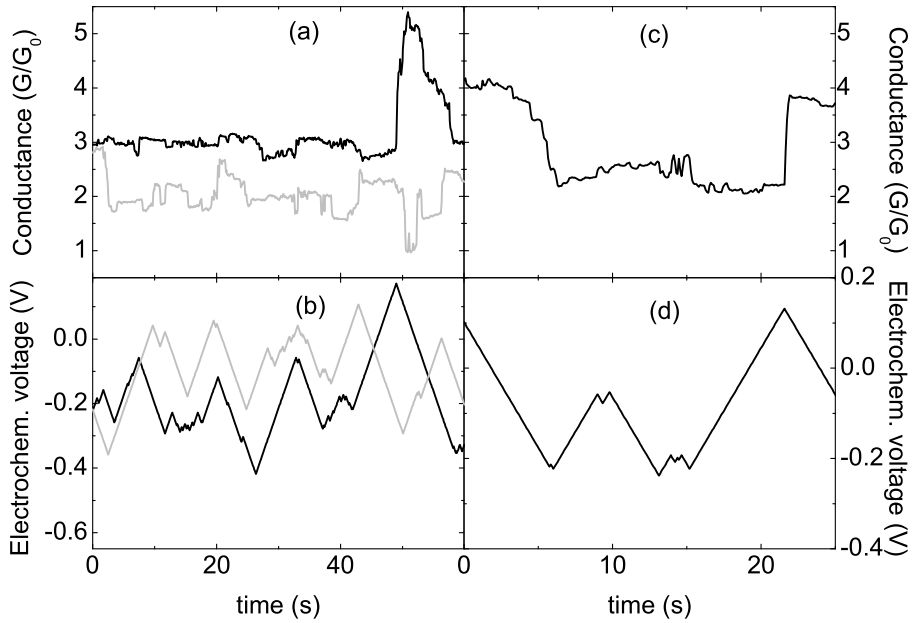


Figure 8.10: Stabilizing contacts in the low conductance regime, where the conductance is expected to be integer multiples of  $G_0$ . In (a) conductance values of 2 (grey line) and  $3 G_0$  (black line) are stabilized. The electrochemical voltage is shown in b using the same colors as in (a). In (c) the conductance is stabilized at  $2.5 G_0$  and the voltage is shown in (d).

tance can be very precisely kept constant at the desired value, having very little variations, of the order of  $\pm 0.1 G_0$ . The electrochemical voltage fluctuations are also small, less than 100 mV. We compare different values of conductance in the range where the shell effect are expected to appear. We observe that the fluctuations are very similar, as one can see in Fig. 8.9 not showing any preference for given diameters.

In the low conductance regime it is more difficult to stabilize a contact, as one can see in Fig. 8.10. The stability decreases as the diameter of the contact goes down starting from about  $6.5 G_0$ . The variations in the conductance are of the order of  $1.5 G_0$  and the voltage oscillations increase to about 400 mV. The oscillations of the conductance for 2 and  $3 G_0$  are slightly lower compared to  $2.5 G_0$ .

## 8.7 Discussion

### 8.7.1 Conductance traces

When comparing the conductance behavior of the nanowires fabricated with the electrochemical methods with the ones obtained from the room temperature UHV-MCBB we have observed several differences. The conductance traces in the majority of the cases does not show plateaus separated by abrupt steps. The electrochemical fabrication differs from the MCBB technique, since the thinning down does not occur due to the external stress applied. It was seen in the force measurements presented in chapter 7 and also reported by other groups [87] that the steps have as origin the atomic rearrangements in the contact. At a step the contact relaxes from the applied mechanical stress. It is not completely unexpected that by removing the atoms from the nanowire electrochemically no steps appear in the conductance. This explanation is valid for large enough contacts formed by hundreds of atoms. In the case of few-atom contact, the conductance is given by the number of atoms in the cross-section. One atom has a conductance of  $1G_0$ . For this regime the conductance is expected to decrease in steps of integer multiples of  $G_0$ . Also for this regime we have seen both types of traces, with steps or continuous decrease of the conductance. The latter can be due to enhanced tunnelling due to adsorbates on the surface.

### 8.7.2 Enhancement of stability by shell effect

In Fig. 8.8 we show a histogram with peaks that coincide with the ones obtained with a MCBB technique. The period of the peaks is what expected from the atomic shell packing for fcc gold nanowires. The preferential breaking of the wires with a plateau at  $2 G_0$  agrees with this, since nanowires along  $[110]$  axis are suggested to break at this value of conductance rather than at  $1 G_0$  [37], [68].  $[110]$  is the axis favorable for atomic shell effect. This issues are discussed in detail in chapter 5. Despite this agreement, the observation of shell structure is not very reproducible and was not observed in the stabilization of the contacts, discussed in section 8.6.2. A possibility is that instead forming a long nanowire, a short disordered neck will grow. This can happen when during the deposition the tendency is to grow large facets. The growing will occur not on the thinnest part of the contact, but very likely on the outer facets.

We could not obtain more statistics due to the fact that the process of deposition/dissolution is not completely controlled. When the wire is completely broken, it is sometimes very difficult to grow it again. The process can take long time and the wire grows suddenly to a very large contact. A possible reason for the uncontrolled growing of the wire can be that the electrochemical deposition is not homogeneous but it has preferred nucleation sites. Therefore, on the sharp tips that are formed after breaking it is energetically unfavorable to grow and instead the deposition takes place more on the flat part of the contact. In this way when the contact is made, it is very large. Another possible reason for the sudden growing can be the fact that we control the reaction by applying

## Discussion

a constant voltage. The current for the same voltage will increase when the size of the smallest electrode increases during the growing process, therefore the deposition rate will be accelerated. Controlling the electrochemical current, that is actually a direct measure of the reaction speed eventually more resolution can be obtained.

### 8.7.3 Low stability of small contacts

Another problem that we encountered is that the breaking speed increases while the size of the contact decreases, therefore the small contacts survive very short and in most of the cases it is difficult to record conductances below  $10 G_0$ . The control of the reaction is in most of the cases very difficult. One factor that might influence this is the RC time of the system. As described above, the interface metal solution is a capacitor due to the double layer charges. Since we use macroscopic wires, the distance between the RE and the WE is of the order of centimeters, giving then also a high resistance of the solution. The resistance of the solution can be estimated from the current versus voltage being around  $500 k\Omega$ . The capacitance due to the double layer is estimated to be of the order of  $0.1 \mu F$ . This would give a RC time of the order of 50 ms, that is still relatively small. Another cause that can slow down the system response is the diffusion. When applying a voltage step we observe that the current needs few seconds to stabilize. Although we use a supporting electrolyte that is suppose to increase the diffusion speed, still the response time might be too large. One would expect that the fast breaking of the small contacts might be due to a too high ionic concentration in the solution. We have seen that this is not the case, the concentration not being a critical parameter in the range 0.01 to 0.1 M. Yet another influencing factor might be the undefined geometry of the wire, as a result the etching can appear simultaneously at several sites. Also since we are working with poly-crystalline wires one needs to take into account that the redox potentials depend on the crystalline orientation.

A recent theoretical paper studies the change in the electrochemical properties when decreasing the size of the electrodes to nanoscale [106]. It is shown that the electrochemical potentials will be different than for the bulk electrodes. It is found that the capacity of the double layer is significantly enhanced and the diffusion speed increases. It is expected that the high electric fields in between the sharp tips will cause preferential etching on the sharp protrusions rather than on the flat electrodes.

The low stability of few atoms contacts is also observed by Li *et al.* [96]. Several measures were taken in order to stabilize them. The contact in this size range is very sensitive even to a small leakage current. In order to minimize it, an electronic relay and a mechanical relay are used in series to avoid this. The nanowires are supported on a solid glass substrate, avoiding in this way eventual breaking due to external mechanical vibrations. In our case the wire is freely suspended between the two sides of the insulating material. As we have also observed, the authors report that by repeated cycles of making and breaking the wire a more stable configuration is achieved. This was also observed in other



techniques of nano-contacts fabrication, as we have seen in the MCBJ and it was previously reported in STM fabrication [29]. The stable configuration achieved is due to annealing of the defects by mechanical indentation. Similarly in the electrochemical etching process initially the process will not be uniform and at the defect position the etching rate will be higher. When the wire is formed of relatively big grains, the whole grain will be etched at once and then a abrupt breaking of the contact appears. Due to the difficult deposition process we couldn't sufficiently repeat the process of contact "annealing".

Some of the difficulties can be avoided using lithographically fabricated samples. In this geometry the RE can be situated close to the sample and it can detect faster the changes due to the electrochemical reactions. Moreover the exposed area can be reduced to dimensions of tens of nm. Possibly by reducing the electrochemical current the electrochemical process becomes more localized and controlled. Another advantage of the lithographically fabricated samples is the possibility of imaging the sample after the measurement that will give information about how the growing and dissolution occurs.

## 8.8 Conclusions

In this chapter we present fabrication of gold nanoscale contacts by electrochemical methods. A conductance histogram obtained by repeated dissolution/deposition shows a series of peaks that agree with the peaks obtained by RT-MCBJ measurements on gold and have the period of atomic shell effect. More statistics and reproducibility are required to confirm the result. It is possible to obtain atomic scale contacts by reversible electrochemical dissolution/deposition. The stability decreases with decreasing the contact size, making the statistical analysis difficult. By adjusting the electrochemical potential we can stabilize any desired conductance value. No preference for given diameters has been observed for the regime where the shell effects has been seen to influence the stability of nanowires fabricated in a MCBJ. Our results do not contradict the results obtained by Li *et al.*, since they refer to a different conductance range. More control is required in order to systematically fabricate and characterize nanowires by electrochemical methods.

# Bibliography

- [1] A. I. Yanson, G. Rubio Bollinger, H. E. van den Brom, N. Agraït, and J. M. van Ruitenbeek, *Nature* **395**, 783 (1998).
- [2] G. Rubio-Bollinger, S. R. Bahn, N. Agraït, K. W. Jacobsen, and S. Vieira, *Phys. Rev. Lett.* **87**, 026101 (2001).
- [3] W. A. de Heer, *Rev. Mod. Phys.* **65**, 611 (1993).
- [4] M. Brack, *Rev. Mod. Phys.* **65**, 677 (1993).
- [5] T. P. Martin, *Phys. Rep.* **273**, 199 (1996).
- [6] A. I. Yanson, I. K. Yanson, and J. M. van Ruitenbeek, *Nature* **400**, 144 (1999).
- [7] A. I. Yanson, I. K. Yanson, and J. M. van Ruitenbeek, *Phys. Rev. Lett.* **87**, 216805 (2001).
- [8] D. F. Urban, J. Bürki, A. I. Yanson, I. K. Yanson, C. A. Stafford, J. M. van Ruitenbeek, and H. Grabert, *Solid State Com.* **131**, 609 (2004).
- [9] A. Bid, A. Bora, and A. K. Raychaudhuri, *Phys. Rev. B* **72**, 113415 (2005).
- [10] J. Bürki and C. A. Stafford, *Appl. Phys. A* **81**, 1519 (2005).
- [11] J. Bürki, C. A. Stafford, and D. L. Stein, *Phys. Rev. Lett.* **95**, 090601 (2005).
- [12] R. Balian and C. Bloch, *Ann. Phys. (N.Y.)* **69**, 76 (1972).
- [13] A. I. Yanson, Ph.D. thesis, Universiteit Leiden, The Netherlands (2001).
- [14] F. Kassubek, C. A. Stafford, H. Grabert, and R. E. Goldstein, *Nonlinearity* **14**, 167 (2001).
- [15] C. A. Stafford, *Phys. Stat. Sol. B* **230**, 481 (2001).
- [16] J. Bürki, R. E. Goldstein, and C. A. Stafford, *Phys. Rev. Lett.* **91**, 254501 (2003).

- [17] C.-H. Zhang, F. Kassubek, and C. A. Stafford, *Phys. Rev. B* **68**, 165414 (2003).
- [18] J. M. van Ruitenbeek, M. H. Devoret, D. Esteve, and C. Urbina, *Phys. Rev. B* **56**, 12566 (1997).
- [19] C. Yannouleas and U. Landman, *J. Phys. Chem. B* **101**, 5780 (1997).
- [20] E. Ogando, N. Zabala, and M. J. Puska, *Nanotechnology* **13**, 363 (2002).
- [21] E. Ogando, T. Torsti, N. Zabala, and M. J. Puska, *Phys. Rev. B* **13**, 075417 (2003).
- [22] D. F. Urban, J. Bürki, C.-H. Zhang, C. A. Stafford, and H. Grabert, *Phys. Rev. Lett.* **93**, 186403 (2004).
- [23] C. A. Stafford, D. Baeriswyl, and J. Bürki, *Phys. Rev. Lett.* **79**, 2863 (1997).
- [24] F. Kassubek, C. A. Stafford, and H. Grabert, *Phys. Rev. B* **59**, 7560 (1999).
- [25] C. A. Stafford, F. Kassubek, J. Bürki, and H. Grabert, *Phys. Rev. Lett.* **83**, 4836 (1999).
- [26] C. Yannouleas, E. N. Bogachek, and U. Landman, *Phys. Rev. B* **57**, 4872 (1998).
- [27] C.-H. Zhang, J. Bürki, and C. A. Stafford, *Phys. Rev. B* **71**, 235404 (2005).
- [28] C. A. Stafford, F. Kassubek, and H. Grabert, *Adv. in Solid State Phys.* **41**, 497 (2001).
- [29] G. Rubio, N. Agraït, and S. Vieira, *Phys. Rev. Lett.* **76**, 2302 (1996).
- [30] C. Höppler and W. Zwerger, *Phys. Rev. Lett.* **80**, 1792 (1998).
- [31] S. Blom, H. Olin, J. L. Costa-Krämer, N. García, M. Jonson, P. A. Serena, and R. I. Shekhter, *Phys. Rev. B* **57**, 8830 (1998).
- [32] N. Zabala, M. J. Puska, and R. M. Nieminen, *Phys. Rev. B* **59**, 12652 (1999).
- [33] F. Kassubek, C. A. Stafford, and H. Grabert, *Physica B* **280**, 438 (2000).
- [34] J. García-Rodeja, C. Rey, L. J. Gallego, and J. A. Alonso, *Phys. Rev. B* **49**, 8495 (1994).
- [35] M. Kabir, A. Mookerjee, and A. K. Bhattacharya, *Phys. Rev. A* **69**, 043203 (2004).
- [36] T. P. Martin, T. Bergmann, H. Ghlich, and T. Lange, *Chem. Phys. Lett.* **176**, 343 (1991).

- [37] V. Rodrigues, T. Fuhrer, and D. Ugarte, Phys. Rev. Lett. **85**, 4124 (2000).
- [38] J. C. Gonzalez, V. Rodrigues, J. Bettini, L. G. C. Rego, A. R. Rocha, P. Z. Coura, S. O. Dantas, F. Sato, D. S. Galvao, and D. Ugarte, Phys. Rev. Lett. **93**, 126103 (2004).
- [39] V. Rodrigues, J. Bettini, A. R. Rocha, L. G. C. Rego, and D. Ugarte, Phys. Rev. B **65**, 153402 (2002).
- [40] Y. Kondo and K. Takayanagi, Phys. Rev. Lett. **79**, 3455 (1997).
- [41] E. A. Jagla and E. Tosatti, Phys. Rev. B **64**, 205412 (2001).
- [42] D. Cheng, W. Y. Kim, S. K. Min, T. Nautiyal, and K. S. Kim, Phys. Rev. Lett. **96**, 096104 (2006).
- [43] E. Medina, M. Díaz, N. León, C. Guerrero, A. Hasmy, P. A. Serena, and J. L. Costa-Krämer, Phys. Rev. Lett. **91**, 026802 (2003).
- [44] O. Gülseren, F. Ercolessi, and E. Tosatti, Phys. Rev. Lett. **80**, 3775 (1998).
- [45] Y. Kondo and K. Takayanagi, Science **289**, 606 (2000).
- [46] Y. Oshima, A. Onga, and K. Takayanagi, Phys. Rev. Lett. **91**, 205503 (2003).
- [47] A. I. Yanson, I. K. Yanson, and J. M. van Ruitenbeek, Fiz. Nizk. Temp. **27**, 1092 (2001).
- [48] A. I. Yanson, I. K. Yanson, and J. M. van Ruitenbeek, Phys. Rev. Lett. **84**, 5832 (2000).
- [49] A. I. Yanson, I. K. Yanson, and J. M. van Ruitenbeek, *Molecular Nanowires and Other Quantum Objects* (Kluwer Academic Publishers, Dordrecht, 2004).
- [50] C. J. Muller, Ph.D. thesis, Universiteit Leiden, The Netherlands (1992).
- [51] C. J. Muller, J. M. van Ruitenbeek, and L. J. de Jongh, Physica C **191**, 485 (1993).
- [52] Torr Seal (Varian Vacuum Products).
- [53] LabView, National Instruments (Austin, TX).
- [54] H. J. Hwang and J. W. Kang, Surf. Sci. **532-535**, 536 (2003).
- [55] A. I. Mares, A. F. Otte, L. G. Soukiassian, R. H. M. Smit, and J. M. van Ruitenbeek, Phys. Rev. B **70**, 073401 (2004).
- [56] A. I. Mares and J. M. van Ruitenbeek, Phys. Rev. B **72**, 205402 (2005).

- [57] M. Díaz, J. L. Costa-Krämer, E. Medina, A. Hasmy, and P. A. Serena, *Nanotechnology* **14**, 113 (2003).
- [58] J. L. Costa-Krämer, *Phys. Rev. B* **55**, R4875 (1997).
- [59] T. Ono and K. Hirose, *Phys. Rev. Lett.* **94**, 206806 (2005).
- [60] I. Katakuse, T. Ichihara, Y. Fujita, T. Sakurai, and H. Matsuda, *Int. J. Mass Spectrom. Ion Processes* **67**, 229 (1985).
- [61] J. A. Torres, J. I. Pascual, and J. J. Sáenz, *Phys. Rev. B* **49**, 16581 (1994).
- [62] E. Scheer, N. Agraït, J. C. Cuevas, A. Levy Yeyati, B. Ludoph, A. Martín-Rodero, G. Rubio Bollinger, J. M. van Ruitenbeek, and C. Urbina, *Nature* **394**, 154 (1998).
- [63] K. Hansen, S. K. Nielsen, M. Brandbyge, E. Lægsgaard, I. Stensgaard, and F. Besenbacher, *Appl. Phys. Lett.* **77**, 708 (2000).
- [64] K. Hansen, E. Laegsgaard, I. Stensgaard, and F. Besenbacher, *Phys. Rev. B* **56**, 2208 (1997).
- [65] J. M. Krans, C. J. Muller, I. K. Yanson, T. C. M. Govaert, R. Hesper, and J. M. van Ruitenbeek, *Phys. Rev. B* **48**, 14721 (1993).
- [66] D. F. Urban, J. Bürki, C. A. Stafford, and H. Grabert, *cond-mat/0608373*.
- [67] J. Opitz, P. Zahn, and I. Mertig, *Phys. Rev. B* **66**, 245417 (2002).
- [68] L. G. C. Rego, A. R. Rocha, V. Rodrigues, and D. Ugarte, *Phys. Rev. B* **67**, 045412 (2003).
- [69] V. Rodrigues and D. Ugarte, *Eur. Phys. J. D* **16**, 395 (2001).
- [70] L. D. Marks, *Rep. Prog. Phys.* **57**, 603 (1994).
- [71] C. Untiedt, G. Rubio, S. Vieira, and N. Agraït, *Phys. Rev. B* **56**, 2154 (1997).
- [72] M. Yoshida, Y. Oshima, and K. Takayanagi, *Appl. Phys. Lett.* **87**, 103104 (2005).
- [73] M. I. Haftel and K. Gall, *Phys. Rev. B* **74**, 035420 (2006).
- [74] X. Li, H. Wu, X. B. Wang, and L. S. Wang, *Phys. Rev. B* **58**, 6775 (1998).
- [75] O. C. Thomas, W. Zheng, S. Xu, and K. H. Bowen, *Phys. Rev. Lett.* **89**, 213403 (2002).
- [76] V. Kumar and R. Car, *Z. Phys. D* **19**, 177 (1991).
- [77] T. Diederich, T. Döppner, J. Braune, J. Tiggesbümker, and K. H. Meiwes-Broer, *Phys. Rev. Lett.* **86**, 4807 (2001).

- [78] A. Lyalin, I. A. Solov'yov, A. V. Solov'yov, and W. Greiner, Phys. Rev. A **67**, 063203 (2003).
- [79] A. I. Yanson and J. M. van Ruitenbeek, Phys. Rev. Lett. **79**, 2157 (1997).
- [80] E. Scheer, P. Joyez, D. Esteve, C. Urbina, and M. H. Devoret, Phys. Rev. Lett. **78**, 3535 (1997).
- [81] D. F. Urban, J. Bürki, C. A. Stafford, and H. Grabert, to be published.
- [82] A. P. Cracknell and K. C. Wong, *The Fermi surface its concepts, determination and use in the physics of metals* (Oxford University Press, Oxford, 1973).
- [83] L. Hui, F. Pederiva, W. Guanhou, and W. Baolin, J. Appl. Phys. **96**, 2214 (2004).
- [84] N. Agraït, A. Levy Yeyati, and J. M. van Ruitenbeek, Phys. Rep. **377**, 81 (2003).
- [85] C. A. Stafford, Physica E **1**, 310 (1998).
- [86] N. Agraït, G. Rubio, and S. Vieira, Phys. Rev. Lett. **74**, 3995 (1995).
- [87] G. Rubio, N. Agraït, and S. Vieira, prl **76**, 2302 (1996).
- [88] G. Rubio-Bollinger, P. Joyez, and N. Agraït, Phys. Rev. Lett. **93**, 116803 (2004).
- [89] J. C. Cuevas, A. Levy Yeyati, A. Martín-Rodero, G. Rubio Bollinger, C. Untiedt, and N. Agraït, Phys. Rev. Lett. **81**, 2990 (1998).
- [90] V. M. García-Suárez, A. R. Rocha, S. W. Bailey, C. J. Lambert, S. Sanvito, and J. Ferrer, Phys. Rev. Lett. **95**, 256804 (2005).
- [91] R. H. M. Smit, C. Untiedt, G. Rubio-Bollinger, R. C. Segers, and J. M. van Ruitenbeek, Phys. Rev. Lett. **91**, 076805 (2003).
- [92] N. van der Post and J. M. van Ruitenbeek, Czech. J. Phys. **46**, **Suppl.S5**, 2853 (1996).
- [93] J. Lyklema, Adv. Colloid Interface Science **2**, 67 (1968).
- [94] E. S. Snow, D. Park, and P. M. Campbell, Appl. Phys. Lett. **69**, 269 (1996).
- [95] C. Z. Li and N. J. Tao, Appl. Phys. Lett. **72**, 894 (1997).
- [96] C. Z. Li, A. Bogozzi, W. Huang, and N. J. Tao, Nanotechnology **10**, 221 (1999).
- [97] A. F. Morpurgo, C. M. Marcus, and D. B. Robinson, Appl. Phys. Lett. **74**, 2084 (1999).

- [98] J. Li, T. Kanzaki, K. Murakoshi, and Y. Nakato, *Appl. Phys. Lett.* **81**, 123 (2002).
- [99] S. Boussaad and N. J. Tao, *Appl. Phys. Lett.* **80**, 2398 (2002).
- [100] S. Nakabayashi, H. Sakaguchi, R. Baba, and E. Fukushima, *Nano Lett.* **1**, 507 (2001).
- [101] J. Xiang, B. Liua, B. Liub, B. Renb, and Z. Q. Tian, *Electrochem. Comm.* **8**, 577 (2006).
- [102] F.-Q. Xie, L. Nittler, C. Obermair, and T. Schimmel, *Phys. Rev. Lett.* **93**, 128303 (2004).
- [103] A. J. Bard and L. R. Faulkner, *Electrochemical methods* (New-York, 1980).
- [104] A. J. C. J. Herrera-Gallego, C. E. Castellano and A. J. Arvia, *J. Electroanal. Chem.* **66**, 207 (1975).
- [105] J. Liu, J. L. Duan, M. E. Toimil-Molares, S. Karim, T. W. Cornelius, D. Dobrev, H. J. Yao, Y. M. Sun, M. D. Hou, D. Mo, et al., *Nanotechnology* **17** (2006).
- [106] E. P. M. Leiva, C. G. Sánchez, and P. Vélez, *Phys. Rev. B* **74**, 035422 (2006).

# Samenvatting

Het is bekend van de hydrodynamica dat een vloeistofkolom, die langer dan zijn omtrek is, niet stabiel is door een te hoge oppervlakte spanning. Deze Rayleigh instabiliteit is al lange tijd bekend, omdat vloeistoffen de neiging hebben een bolvorm aan te nemen om de oppervlakte energie te minimaliseren. Op nanometerschaal gedragen metalen bij hogere temperatuur zich enigszins vergelijkbaar met een vloeistof. Hoe kunnen dunne draden dan stabiel zijn? Dit is de vraag die we in dit proefschrift willen beantwoorden. Onlangs is ontdekt dat dunne nanodraden van een enkel atoom dik en tot zeven atomen lang, kunnen groeien tussen twee grotere elektroden. Als de nanodraad dikker wordt, maar nog in het nanometer bereik, verschijnen andere stabiele draad structuren die niet willekeurig zijn, maar welbepaalde en reproduceerbare diameters hebben. We noemen ze magische nanodraden, zoals in metallische clusters waar heel stabiele diameters zijn ontdekt die aan dezelfde schillenstructuur zijn toegeschreven. Wij willen weten hoe de elektronische en de atomaire eigenschappen van verschillende metalen de magisch nanodraden beïnvloeden. Een significant deel van dit proefschrift gaat over de studie van schillenstructuur in verschillende metalen: edelmetalen en meerwaardige metalen zoals Al en Mg. De andere twee delen gaan over de stabiliteit, vanuit verschillende aspecten gezien. In hoofdstuk 7 wordt de stabiliteit vanuit een mechanisch standpunt onderzocht. Het laatste hoofdstuk gaat over een elektrochemische methode van fabriceren van nanodraden, waar we mogelijkheden onderzoeken om de nanodraden meer stabiel te maken.

Aangezien wij bijzonder geïnteresseerd zijn in de studie van metallische nanodraden, willen wij weten hoe hun elektronische en mechanische eigenschappen met elkaar zijn verbonden. Hun elektronische structuur bepaalt hun stabiliteit alsook hun geleiding. Nanodraden worden met de mechanisch instelbare breekjunctie techniek (MCBJ) verkregen, die in hoofdstuk 3 wordt beschreven. Met deze techniek kan men willekeurige metalen onderzoeken. Het maakt een statistische analyse mogelijk, aangezien nanodraden herhaaldelijk kunnen worden gebroken en teruggekregen. Met deze techniek meten we de geleiding van de nanodraden, die directe informatie over de diameter geeft. The MCBJ techniek is gebruikt bij kamer temperatuur in ultrahoog vacuüm voor alle metalen die wij hebben onderzocht.

De stabilisatie van bepaalde diameters als gevolg van de opsluiting van de golf functies van de elektronen binnen de draad wordt het elektronisch schil effect genoemd. De energieniveaus zijn gegroepeerd in schillen en een nanodraad wordt stabiel wanneer een dergelijk schil wordt gevuld. De stabiele diameters komen overeen met de bekende magische getallen van metaalclusters. Het elektronische schil effect is opmerkelijk robuust zodat de Rayleigh instabiliteit onderdrukt wordt. De stabiliteit van nanodraden kan in een "jellium" model



van vrije elektronen worden beschreven dat door een harde wand potentiaal wordt begrensd. De theoretische modellen worden beschreven in hoofdstuk 2. Dikkere nanodraden zijn stabiel wanneer de oppervlakteenergie minimaal is. Nanodraden kunnen geen cilindervorm aannemen zoals een vloeistof, maar een stabiele configuratie wordt gevonden voor de dichtst gepakte geometrie. Wij modelleren de draad als hebben ze een hexagonale pakking, die in hoofdstuk 2 wordt voorgesteld. De verhoogde stabiliteit treedt op wanneer een facet van de zeshoek volledig bedekt is. Dit stabiliserende effect wordt ook gevonden voor metaalclusters en het is bekend als de atoomschilstructuur. Het schileffect in nanodraden werd eerst gevonden voor alkalimetalen die in zeer goede benadering vrije elektronenmetalen zijn. Omdat ze een perfect bolvorming Fermioppervlak hebben, zijn het ideale systemen voor experimentele studie. Nochtans, voor mogelijke toepassingen zijn zij niet geschikt omdat zij zeer reactief zijn. Een ander nadeel is hun lage smelttemperatuur, die het gebruik bij kamertemperatuur onmogelijk maakt. Wij hebben de studie uitgebreid tot een van het meest gebruikte materialen in nanotechnologie toepassingen: goud. Wij hebben gezien dat het mogelijk is om verscheidene dagen met goud bij kamertemperatuur in ultrahog vacuüm te werken. In lucht kan men verscheidene uren zonder enige tekenen van verontreiniging werken. Dit is toe te schrijven aan de opmerkelijke chemische stabiliteit van goud. In hoofdstuk 4 laten wij zien dat het schileffect de stabiliteit van gouden nanodraden beïnvloedt. De stabiliteit wordt bepaald door het vullen van elektronische schillen voor kleine diameters, tot draden van ongeveer tien atomen dik. Voor grotere diameters hebben de pieken een andere periode die het vullen van hexagonale facetten weergeeft. De andere twee edelmetalen, zilver en koper, vertonen gelijkaardige resultaten. De kristalrichting is een belangrijke parameter voor atomaire schilstructuur. Daarom hebben wij de invloed van de initiële kristaloriëntatie op de schilstructuur onderzocht, hetgeen in hoofdstuk 5 wordt beschreven. Wij gebruiken kristallen van goud die langs de [110], [100] en [111] richting zijn georiënteerd. Wij hebben aanwijzingen dat de [110] richting voor de dichtste atoompakking zorgt. De andere twee zijn minder stabiel en waarschijnlijk vertonen ze een overgang naar de [110] as wanneer de draad herhaaldelijk wordt gebroken en samengedrukt. De resultaten van dit experiment bevestigen onze vermoedens dat de [110] as de voorkeursrichting voor atoompakking in fcc nanodraden is. Verder hebben wij een opmerkelijk effect ontdekt: een hoge elektrische spanning over het contact (bias) stabiliseert contacten met een geleiding rond de kwantumeenheid. Deze contacten blijven uren stabiel zodra ze zijn gevormd en de mechanische spanning in de elektrodes verwijderd wordt. Dit effect verschijnt bij een biasspanning van rond de 400 mV. Onder deze waarde zullen dergelijke contacten in enkele milliseconden breken. Wij hebben aanwijzingen dat het effect aan een laag van adsorbaten tussen de twee metaalelektroden toe te schrijven is. Het effect is omkeerbaar: wanneer we teruggaan naar een lage bias wordt het schone gedrag van goud teruggevonden.

Aangezien de *s*-orbitalen verantwoordelijk zijn voor de geleiding in edelmetalen, kunnen zij in een goede benadering als vrije elektronmetalen worden beschouwd. In de volgende stap richten wij ons op complexere metalen zoals Al en Mg. Hun Fermioppervlak is niet meer bolvorming. De vraag is of dit

de nanodraden zal beïnvloeden. Voor aluminium hebben wij sterke aanwijzingen dat wij twee reeksen magische diameters waarnemen, vergelijkbaar met de alkali en edelmetalen. Bovendien zijn er bijzondere pieken aanwezig in het stabiliteitsspectrum die niet binnen een eenvoudig vrij elektronenmodel worden verwacht. Het stabiliteitsspectrum voor magnesium is complexer. Hoewel in sommige histogrammen de pieken in twee categorieën kunnen worden verdeeld die betrekking hebben op de elektronische en atomaire schilstructuur, hebben de meeste histogrammen pieken die aan een gemengde structuur moeten worden toegeschreven. Dergelijke configuraties kunnen een compromis tussen een gunstige geometrische pakking en elektronische energiminima zijn. Verder hebben wij aanwijzingen dat dunne magnesium nanodraden een metaal-isolator overgang hebben.

Directe informatie over de stabiliteit van de nanodraden komt uit krachtmeting. Wij meten de stijfheid, hetgeen een directe maat is van de sterkte van de atomaire bindingen. De magische diameters zouden een verhoogde stijfheid moeten hebben, die zich tegen externe vervorming verzet. Wij gebruiken de MCBJ techniek in combinatie met een stemvork. De stemvork is een kwartsoscillator die een scherpe en nauwkeurige resonantiefrequentie bij 32768 Hertz heeft, die in digitale horloges wordt gebruikt om de tijd bij te houden. De piezoelektrische armen van de stemvork zetten de schommeling in een evenredige stroom om die gemakkelijk kan worden gemeten. Dit vervangt de anders ingewikkelde optische detectie van afbuiging. Een commerciële stemvork wordt aan de metaalverbinding vastgemaakt en meet de krachten in de nanodraad terwijl deze wordt opgerekt. De verschuiving in de resonantiefrequentie is evenredig aan de stijfheid van het metaalcontact. Gelijktijdig meten wij de geleiding, als maat voor de contactgrootte. Wij hebben de stabiliteit van nanodraden bij kamertemperatuur onderzocht, waar wij naar schillenstructuur zochten. Hoewel een schillenstructuurpatroon wordt waargenomen, is meer statistiek nodig om het definitief met het schil-effect in verband te brengen. Tevens hebben wij de stabiliteit van een atomaire kettingen van Au en Pt bij vloeibare heliumtemperatuur gemeten. Men kan het proces van ketenvorming in de stijfheidsmeting waarnemen, als plotselinge ontspanningen op het ogenblik dat een nieuw atoom in de ketting springt. Wij hebben gevonden dat de kettingen die zachter zijn, en dus een lagere stijfheid hebben, langer kunnen groeien.

De elektrochemische vervaardiging van goud nanodraden wordt beschreven in hoofdstuk 8. De elektrochemie is een veelbelovende techniek die verfijndere nano-fabricatie procedures kan vervangen. Door een macroscopische draad elektrochemisch op te lossen konden wij nanocontacten verkrijgen. Door de elektrochemische spanning aan te passen kan men contacten stabiliseren die slechts door enkele atomen worden gevormd. Een geleiding histogram gevormd op basis van herhaalde cycli van het oplossen en het deponeren van nanodraden toont pieken die met die voor atoomschilstructuur bij UHV in overeenstemming zijn.

Samenvattend beschrijft dit proefschrift verschillende aspecten van de vorming en stabiliteit van nanodraden, onder invloed van hun elektronische en atomeigenschappen door middel van gemeten de elektrische en mechanische eigenschappen.



# List of publications

- **A. I. Mares**, A. F. Otte, L. G. Soukiassian, R. H. M. Smit and J. M. van Ruitenbeek  
*Observation of electronic and atomic shell effects in gold nanowires*  
Phys. Rev. B **70**, 073401 (2004).
- A. M. C. Valkering, **A. I. Mares**, C. Untiedt, K. Babaei Gavan, T. H. Oosterkamp, and J. M. van Ruitenbeek  
*A force sensor for atomic point contacts*  
Rev. Sci. Instr. **76**, 103903, (2005).
- **A. I. Mares** and J. M. van Ruitenbeek  
*Observation of shell effects in nanowires for the noble metals Cu, Ag, and Au*  
Phys. Rev. B **72**, 205402 (2005).
- M. R. Calvo, **A. I. Mares**, V. Climent, J. M. van Ruitenbeek and C. Untiedt  
*Formation of atomic-sized contacts controlled by electrochemical methods*  
submitted to Phys. Stat. Sol. (cond-mat/06101890) (2006).
- **A. I. Mares**, G. van Dorp and J. M. van Ruitenbeek  
*Observation of shell structure in aluminum nanowires*  
Manuscript in preparation.
- **A. I. Mares**, G. van Dorp and J. M. van Ruitenbeek  
*Observation of shell effects in magnesium nanowires*  
Manuscript in preparation.
- M. R. Calvo, **A. I. Mares**, C. Untiedt and J. M. van Ruitenbeek  
*Highly stable atomic contacts formed at high bias voltage*  
Manuscript in preparation.
- **A. I. Mares** and J. M. van Ruitenbeek  
*On the influence of crystal orientation in the atomic wire formation*  
Manuscript in preparation.
- T. Shiota, **A. I. Mares** and J. M. van Ruitenbeek  
*Mechanical properties of monoatomic platinum chains*  
Manuscript in preparation.



# Curriculum Vitae

of Ancuta Ioana Mares, born in Hunedoara, Romania on January 12, 1979.

In the summer of 1997 I obtained the diploma from the High School "Aurel Vlaicu" in Orastie. The following autumn I joined the Physics department of the University of Bucharest. Here I spent the first three years of my studies, while the two last ones including my research projects were done at Leiden University. My first research project was done in the group of Prof. L. J. de Jongh in the Kamerlingh Onnes Laboratory with the title "Magnetic Measurements in Superconducting Nanowires". My master project was performed in the group of Prof. J. M. van Ruitenbeek, at the same laboratory with the title: "Force Measurements in Atomic-Size Contacts". In the summer of 2002 I received my graduation diploma from the University of Bucharest with the title engineer physicist. In the same autumn I graduated *cum laude* at Leiden University.

I continued with a PhD in the same university under the supervision of Prof. J. M. van Ruitenbeek. The project was funded by Stichting voor Fundamenteel Onderzoek der Materie (FOM) and it concerns stability analysis of metallic nanowires. The research carried out within this project is presented in this thesis. For the work on the electrochemically fabrication of metallic nanowires I enjoyed the hospitality of Dr. C. Untiedt of the University of Alicante, Spain. During my PhD period I was assistant at the Laboratory Training for the second-year students of the Leiden Institute of Physics.



# Acknowledgements

I would like to thank all the people who were involved in the realization of this thesis. As can be seen at the beginning of the chapters, most of the work was done in collaboration.

First I would like to thank to my colleagues from the AMC group: Darko Djukic, Christian Martin, Sander Otte, Oren Tal, Robert Thijssen and Alex Yanson. I would also like to thank to the people that initiated me in the MCBJ technique and ultra high vacuum practice: Annemarie Valkering, Roel Smit, Carlos Untiedt and Marcel Rost. Carlos Untiedt and Sander Otte helped me a lot with LabView programming. My student Gijs van Dorp performed part of the measurements for Al and Mg nanowires.

The theoreticians Daniel Urban, from the Albert-Ludwigs-Universität, Germany, Jerome Bürki and Charles Stafford from the University of Arizona, Tucson provided many results and useful discussions.

I enjoyed very much working with T. Shiota from Tokio Institute of Technology, Japan, during his stay in our group, on the force measurements presented in this thesis. For this project Annemarie Valkering and Tjerk Oosterkamp provided useful advice and discussions. We had a fruitful collaboration with the group of Carlos Untiedt in Alicante. There I performed some of the electrochemical measurements together with Reyes Calvo. I learned a lot from Reyes, Carlos and the electrochemist Victor Climent.

Marcel Pohlkamp, Raymond Koehler and Bert Crama (Electronische Dienst) were eager to help whenever some problems with the electronics were arising and they also built some very useful pieces of equipment for us. Ruud van Egmond and Christiaan Pen (Fijn Mechanische Dienst) made fine pieces for my set-up. Concerning computer management support, I am grateful to Fred Kranenburg who would in no time come to solve my problems.